OULU 2015
C 547

ACTA

UNIVERSITATIS OULUENSIS

Tiina Pääkkönen

IMPROVING THE ENERGY EFFICIENCY OF PROCESSES

REDUCTION OF THE CRYSTALLIZATION FOULING OF HEAT EXCHANGERS

UNIVERSITY OF OULU GRADUATE SCHOOL;
UNIVERSITY OF OULU,
FACULTY OF TECHNOLOGY

ACTA UNIVERSITATIS OULUENSIS
C Technica 547

TIINA PÄÄKKÖNEN

IMPROVING THE ENERGY EFFICIENCY OF PROCESSES

Reduction of the crystallization fouling of heat exchangers

Academic dissertation to be presented with the assent of the Doctoral Training Committee of Technology and Natural Sciences of the University of Oulu for public defence in the Kuusamonsali (YB210), Linnanmaa, on 13 November 2015, at 12 noon

UNIVERSITY OF OULU, OULU 2015

Acta Univ. Oul. C 547, 2015

Supervised by
Professor Riitta Keiski
Docent Esa Muurinen
Professor Carey Simonson

Reviewed by
Professor Sylvain Lalot
Doctor Kamel Hooman

Opponent
Doctor Wolfgang Augustin

ISBN 978-952-62-0934-0 (Paperback)
ISBN 978-952-62-0935-7 (PDF)

ISSN 0355-3213 (Printed)
ISSN 1796-2226 (Online)

Cover Design
Raimo Ahonen

JUVENES PRINT
TAMPERE 2015

Pääkkönen, Tiina, Improving the energy efficiency of processes. Reduction of the crystallization fouling of heat exchangers
University of Oulu Graduate School; University of Oulu, Faculty of Technology
Acta Univ. Oul. C 547, 2015
University of Oulu, P.O. Box 8000, FI-90014 University of Oulu, Finland

Abstract

Heat exchangers are used in industrial processes to transfer energy from one source to another. Heat exchangers improve the energy efficiency of processes and therefore increase the profitability and decrease the environmental impact of production. Effectiveness of heat exchangers may be diminished by fouling, in which unwanted material deposits on the heat transfer surface reducing the heat transfer and increasing the pressure drop of the system. Due to fouling, the energy demand, and the operation and maintenance costs of industrial processes increase significantly. In addition, fouling causes considerable environmental effects due to the increased energy demand and the use of additives and cleaning chemicals.

In this thesis, the crystallization fouling of calcium carbonate on heat transfer surfaces was studied using experimental and modeling methods with the aim to reduce fouling by increasing the understanding of the crystallization fouling phenomenon and providing a validated model for studying crystallization fouling on heat transfer surfaces. The fouling experiments were conducted in a laboratory scale set-up to study the crystallization fouling mechanism under controlled conditions. Based on the knowledge and data gained from the experiments, a crystallization fouling model was developed, and validated in various conditions. As a result, the most important parameters affecting crystallization fouling were identified, and the governing sub-processes were determined. The developed model was used to optimize the surface temperature of a heat exchanger to provide the maximum heat transfer rate when the heat exchanger is subject to fouling at various cleaning intervals. In addition, the used methods were applied in the study of the abatement of fouling by surface modifications.

Based on the results, the studied crystallization process is governed by the surface integration sub-process. In addition, the residence time of the fluid at the wall affects the mass deposition. The results showed that the surface temperature and the shear stress are the most important parameters affecting fouling in the studied conditions, and therefore, they should be defined accurately. For this purpose, CFD was found to provide a useful tool. The developed models were found to predict reliably the experimental conditions. Therefore, the thesis shows that the developed model facilitates the design of heat exchangers, but also assists in minimizing the fouling of heat exchangers.

Keywords: calcium carbonate, CFD, crystallization, fouling, heat exchanger, heat transfer

Pääkkönen, Tiina, Prosessien energiatehokkuuden parantaminen. Lämmönvaihtimien kiteytyvän likaantumisen hallinta
Oulun yliopiston tutkijakoulu; Oulun yliopisto, Teknillinen tiedekunta
Acta Univ. Oul. C 547, 2015
Oulun yliopisto, PL 8000, 90014 Oulun yliopisto

Tiivistelmä

Lämmönvaihtimia käytetään teollisissa prosesseissa siirtämään energiaa kohteesta toiseen. Lämmönvaihtimet parantavat prosessien energiatehokuutta ja siten lisäävät tuotannon kannattavuutta ja vähentävät ympäristövaikutuksia. Lämmönvaihdinten energiatehokkuutta heikentää kuitenkin likaantuminen, jossa lämmönsiirtopinnalle muodostuu kerrostuma, joka heikentää lämmönsiirtoa ja aiheuttaa virtausvastusta. Likaantuminen lisää lämmönvaihdinten energiankulutusta ja käyttökustannuksia sekä aiheuttaa merkittäviä ympäristöpäästöjä kasvaneen energiantarpeen sekä lisä- ja puhdistusaineiden käytön vuoksi.

Tässä työssä tutkittiin kalsium karbonaatin aiheuttamaa lämmönsiirtopintojen kiteytyvää likaantumista käyttäen sekä kokeellisia että mallinnusmenetelmiä. Työn tavoitteena oli lisätä tietoa kiteytyvästä likaantumisesta sekä kehittää validoitu laskentamalli, jolla voidaan tutkia lämmönsiirtopintojen kiteytyvää likaantumista. Likaantumiskokeet tehtiin laboratoriomittakaavan koelaitteessa, jolla voidaan tutkia likaantumismekanismia hallituissa olosuhteissa. Kokeista saadun tiedon ja aineiston perusteella kehitettiin kiteytyvää likaantumista kuvaava malli, joka validoitiin eri olosuhteissa. Tulosten perusteella identifioitiin tärkeimmät kiteytyvään likaantumiseen vaikuttavat parametrit sekä määritettiin rajoittavat osa-prosessit. Kehitettyä mallia käytettiin lämmönsiirtoprosessin optimoinnissa. Lisäksi käytettyjä metodeja sovellettiin tutkimukseen, jossa likaantumista pyrittiin vähentämään pintamodifikaatioiden avulla.

Tulosten perusteella tutkittu kiteytymisprosessi on pinta-integraation rajoittama. Lisäksi havaittiin, että fluidin viipymäaika lämmönsiirtopinnalla vaikuttaa likaantumisnopeuteen. Tulokset osoittivat, että pintalämpötila ja leikkausjännitys ovat tärkeimmät kiteytyvään likaantumiseen vaikuttavat tekijät tutkituissa olosuhteissa. Näin ollen niiden tarkka määrittely on erittäin tärkeää likaantumisnopeuden mallintamiseksi luotettavasti. Virtauslaskenta (CFD) osoittautui hyödylliseksi työkaluksi näiden parametrien määrittämisessä. Tulosten perusteella kehitetty malli ennustaa luotettavasti kokeellisia olosuhteita. Näin ollen tämä työ osoittaa, että kehitettyä mallia voidaan käyttää apuna paitsi lämmönvaihtimien suunnittelussa myös lämmönsiirtopintojen kiteytyvän likaantumisen vähentämisessä.

Asiasanat: CFD, kalsiumkarbonaatti, kiteytyminen, likaantuminen, lämmönsiirto, lämmönvaihdin

To my beloveds

Acknowledgements

This doctoral study was conducted in the Environmental and Chemical Engineering research group (former Mass and Heat Transfer Process Laboratory) of the Faculty of Technology at the University of Oulu. I am very thankful for all the people who have contributed to my work or supported me somehow or other during my doctoral studies. I would like to give special recognition for the people who made this work possible.

First of all, I wish to express my gratitude to my principal supervisor, Prof. Riitta Keiski for the opportunity to work in her research group, and for the encouragement and solid support she has given me in every moment of this journey. The possibility to work in many interesting projects and with numerous talented people has been very rewarding and chastening. I would also like to thank my supervisor, Doc. Esa Muurinen for his support and guidance especially in CFD related issues. I am also grateful for the time and advise he has given me regardless of the subject. I truly appreciate the guidance and advice of my second supervisor, Prof. Carey Simonson from the University of Saskatchewan, Canada. Our discussions and his thorough and insightful comments on my work have been very valuable for me. In addition, his positive and encouraging way of giving feedback gives lots of motivation to keep on working. I am also deeply grateful for him for the opportunity to spend a research phase at the University of Saskatchewan. That time not only greatly advanced my work, but was also really memorable for me and my family.

This work has been financed by several sources, to all of which I'm very grateful. That support made it possible to conduct the research work needed for this thesis, but also enabled the participation in many conferences, courses and meetings, as well as realized the research period in Canada. Therefore, I highly appreciate the former Graduate School for Energy Science and Technology (EST) for providing me a three year grant to my doctoral work. I would also like to acknowledge the Finnish Funding Agency for Innovations (Tekes) and Academy of Finland, as well as many industrial partners for financing the research projects related to this study. Especially, I am grateful for Outokumpu Stainless AB for providing me the material for the fouling tests. In addition, Jenny and Antti Wihuri Foundation, Tauno Tönning foundation, Emil Aaltonen Foundation and Tekniikan Edistämissäätiö, as well as the Doctoral Program in Energy Efficiency and Systems (EES), the University of Oulu Graduate School (UniOGS), and the

Faculty of Technology at the University of Oulu are appreciated for the financial support.

Further, I would like to sincerely thank Prof. Sylvain Lalot from the Université de Valenciennes et du Hainaut-Cambrésis and Dr. Kamel Hooman from the University of Queensland for reviewing the manuscript of this thesis and giving the valuable comments on it.

I have worked in many interesting projects and done co-operation with several people during my doctoral studies, from which many have influenced on the content of my work somehow. I am especially grateful to my co-authors Dr. Ulla Ojaniemi, Dr. Timo Pättikangas and Dr. Mikko Manninen from VTT for advising and helping me in modeling issues, and for sharing their expertise and ideas concerning my work. The warmest compliments I would like to express to Dr. Eini Puhakka for being such a great co-operator and an excellent example of a skillful project coordinator. My co-worker M.Sc.(Tech) Markus Riihimäki also earns special honor. His extensive skills on experimental work and great analytical touch on everything have certainly advanced my work and helped me a lot. I would also like to thank him for his enjoyable company on many trips.

I would like to thank the whole Environmental and Chemical Engineering research group for the collaboration and for the enjoyable moments during the lunch and coffee breaks. It has been pleasure to working with you all. Especially, I would like to express my gratitude to Dr. Satu Pitkäaho for her friendship and support, and for providing me a great example of vigorous and efficient researcher woman. I am also thankful for Dr. Timo Kulju for the discussions and advices concerning CFD modeling. I also appreciate the comments and recommendations he provided me during the writing process of my thesis. Furthermore, I would like to address warm thanks to Lic.Sc.(Tech) Liisa Myllykoski, Lic.Sc.(Tech) Kaisu Ainassaari, Lic.Sc.(Tech) Ritva Isomäki, B.Sc.(Nutr.) Auli Turkki, M.Sc.(Tech) Sanna Antikainen, M.Sc.(Tech) Anna Valtanen, M.Sc.(Tech) Ari Vuokila, Dr. Minna Pirilä, and Doc. Mika Huuhtanen for being always so supportive, helpful, and kind.

I would like to express my heartfelt thanks to my long term colleague, office-mate and dear friend Lic.Sc.(Tech) Reeta Tolonen. We have spent many enjoyable moments in work, but also on spare time from which I am really glad. Your support and listening ear has been very important to me during these years. I also highly appreciate your comments on my work during the writing process of the thesis.

I am truly grateful for Lic.Sc.(Tech) Jenni Ylä-Mella for her friendship and support. Especially the last year has included some moments when presence of a good, understanding friend, as you are, has been indispensable. Thank you, Jenni, for listening, helping, and supporting me always when I need it.

I'm for evermore thankful to my parents, mother Leena and farther Kauko, for supporting me always in my decisions and for being there whenever needed. They have also encouraged me to take up the challenges as well as done their best to help me to reach my ambitions. I would also like to thank my little brother, Sampo, and his partner, Jenni, for showing me another way of life, and by that, reminding me about the most important things in the life. Sampo, I also appreciate our debates; perhaps they have prepared me for the defense. I am also grateful to my mother-in-law, Raija, for taking such a good care of our children always when we have needed help.

I express my deepest gratitude to my loving husband, Sami. Without your involvement and contribution to our everyday life, combining domesticity and working life would have been much more complicated and harder. Without your contribution, especially during the last year, I wouldn't have been able to finalize my thesis yet. In addition, your support and encouragement has given me motivation during my thesis work. Even completing this thesis is a great achievement in my life, the most remarkable accomplishments in my life are my dear sons. Samuli and Matias, you bring the sun shine and joy into my life. You also help me to keep my thoughts out of work when needed which provides the invaluable balance in my life. Thank you my loved ones!

August 2015 Tiina M. Pääkkönen

List of symbols and abbreviations

Latin symbols

A	area [m^2]
a	coefficient
B	bias uncertainty
b	coefficient
C	capacity rate [W/K], concentration [mol/l], in the models [kg/m^3]
$C_{1\varepsilon, 2\varepsilon, 3\varepsilon, \mu}$	constants
c	molar density of the solution [$g\text{-}mol/cm^3$]
c_p	specific heat [$J/(kg\cdot K)$]
D	diffusion coefficient [m^2/s]
Da	Damköhler number
D_h	hydraulic diameter [m]
d_p	mean crystal diameter [m]
E	specific energy [m^2/s^2]
E_a	activation energy [J/mol]
F	External body force [N]
f	Fanning friction factor
G_k	generation of turbulence kinetic energy due to mean velocity gradients
G_b	generation of turbulence kinetic energy due to buoyancy
g	gravitational acceleration [m/s^2]
h	convective heat transfer coefficient [$W/(m^2\cdot K)$]
I	unit tensor
J	diffusion flux [m^2/s]
J^*	molar diffusion flux [$kmol/s\cdot m^2$]
k	turbulent kinetic energy [m^2/s^2]
k_r	rate constant for the surface integration [$m^4/(kg\cdot s)$]
k_r'	coefficient [$m^4/(kg\cdot s^2)$]
k_{rem}	removal coefficient
k_0	pre-exponential factor [$m^4/(kg\cdot s)$]
k_0'	coefficient [$m^4/(kg\cdot s^2)$]
L	characteristic length [m]
m	mass [kg]

$\dot{m}$	mass flow rate [kg/s^2]
m_d	mass deposition rate [kg/m^{2}s]
m_r	mass removal rate [kg/m^{2}s]
n	order of reaction, normal component
Nu	Nusselt number
P	precision uncertainty
p	pressure [Pa]
Pr	Prandtl number
Q	heat flow rate [W]
q	heat flux [W/m^2]
R	gas constant [J/(mol·K)], net rate of production of species
r	parameter
Re	Reynolds number
R_f	fouling resistance [m^{2}K/W]
R_w	thermal resistance of the wall [K/W]
Sc	Schmidt number
Sh	Sherwood number
S_h	source term for heat
S_i	source term for species i
S_m	source term for mass
T	temperature [K, °C]
t	time [s]
t_{sf}	time scaling factor [s]
U	overall heat transfer coefficient [W/(m^{2}K)]
U_i	uncertainty in parameter i
U_{tot}	total uncertainty
u	velocity on x direction [m/s]
V	friction velocity [m/s]
v	flow velocity [m/s]
w	mean flow velocity above the fouling layer [m/s]
X	distance from the duct inlet [m]
x	thickness [m], mole fraction
Y_i	mass fraction of species i
Y_m	contribution of the fluctuating dilatation to overall dissipation rate

Greek letters

α	thermal diffusivity [m^2/s]
β	mass transfer coefficient [m/s]
δ	linear expansion coefficient [1/K]
ε	porosity [-], dissipation rate [m^2/s^3]
ϵ	effectiveness
η	shear viscosity [kg/(m·s)]
η_c	effectiveness factor
λ	thermal conductivity [W/(m·K)]
μ	dynamic viscosity [kg/(m·s)]
μ_t	turbulent viscosity [kg/(m·s)]
ν	momentum diffusivity [m^2/s]
θ	temperature difference [K], sensitivity coefficient
ρ	density [kg/m^3]
σ	turbulent Prandtl number, Stefan-Bolzmann constant [$W/(m^2K^4)$]
τ	shear stress [Pa]
ω	mass fraction of solute in solution

Subscripts and superscript

A	species A
B	species B
b	bulk
c	cold
exp	experiment
f	fluid
fl	fouling layer
h	hot
i	interfacial
in	inlet
j	species j
m	mean
max	maximum
min	minimum
out	outlet
rad	radiation

ref	reference
s	surface
sat	saturation
sur	surrounding
t	at a certain time t
w	wall
0	initial

Acronyms

CFD	Computational Fluid Dynamics
FVM	Finite Volume Method
LES	Large Eddy Simulation
PHE	Plate Heat Exchanger
RANS	Reynolds-averaged Navier-Stokes
SEE	Standard Error of Estimate

Abbreviations

etc.	et cetera, and so on
i.e.	id est, that is
e.g.	exempli gratia, for example

List of original publications

This thesis is based on the following publications, which are referred throughout the text by their Roman numerals:

I Pääkkönen TM, Riihimäki M, Simonson CJ, Muurinen E, and Keiski RL (2012) Crystallization fouling of $CaCO_3$ – Analysis of experimental thermal resistance and its uncertainty. International Journal of Heat and Mass Transfer 55: 6927–6937.

II Pääkkönen TM, Riihimäki M, Simonson CJ, Muurinen E, and Keiski RL (2015) Modeling $CaCO_3$ crystallization fouling on a heat exchanger surface – definition of fouling layer properties and model parameters. International Journal of Heat and Mass Transfer 83: 84–98.

III Pääkkönen TM, Ojaniemi U., Pättikangas T, Manninen M, Muurinen E, Keiski RL and Simonson CJ, (2015) CFD modeling of $CaCO_3$ crystallization fouling on heat transfer surfaces. Manuscript.

IV Pääkkönen TM, Ojaniemi U, Riihimäki M, Muurinen E, Simonson CJ, Keiski RL (2013) Surface patterning of stainless steel in prevention of fouling in heat transfer equipment. Materials Science Forum 762: 493–500.

Pääkkönen was the main and corresponding author of all Papers I-IV.

Table of contents

1 Introduction

This chapter provides the motivation and background for the research in this doctoral thesis. In addition, the scope and aims of the research, as well as an overview of the research are given.

1.1 The research problem

Greenhouse gases are a significant cause for global climate change (Stocker *et al.* 2014). Carbon footprint can be used to measure the amount of produced greenhouse gases. The carbon footprint of industrial production or equipment consists of material acquisition, manufacturing of equipment, use of energy and chemicals during the operation, maintenance and demolition or recycling of the equipment. The carbon footprint of process equipment can be decreased by improving the energy efficiency of the process.

The energy efficiency of processes is lowered by fouling, which is the deposition of unwanted material on the surfaces of the process equipment (especially heat exchangers). The fouling layer increases the resistance to heat transfer between process streams in heat exchangers, and as the thickness of the fouling layer increases, the flow channel narrows, which increases the pressure drop in the system. In addition, fouling may cause flow maldistribution or corrosion. Cleaning of the fouled surfaces leads to the use of cleaning chemicals, interruptions of the production, and additional energy and personnel costs. In addition, process equipment is often oversized to take into account the expected fouling. As a whole, fouling decreases the economic profitability of processes and increases the environmental impact of production, which makes fouling a major challenge in the design and operation of process equipment. (Bott 1995, Müller-Steinhagen *et al.* 2002, Müller-Steinhagen *et al.* 2009, Müller-Steinhagen 2011)

Fouling problems have been investigated for nearly 5 decades, since the 1970's, when the oil crisis stimulated research on fouling. Research has provided different solutions and advantages in the mitigation of fouling, but in many cases fouling, as a complicated and diverse phenomenon, still remains an unresolved problem. It is estimated that the annual costs of fouling in heat transfer equipment is about 0.25% of the Gross National Product of industrialized countries (Bansal *et al*. 2008). Further, it is estimated that fouling is responsible for 2.5% of the carbon dioxide emissions that are produced by human beings. In addition to the considerable greenhouse gas emissions, fouling increases NO_x and SO_x

emissions, which cause acidification of water resources and soil, and the use of chemicals to avoid fouling or to clean fouled heat exchangers may cause toxic effluents. (Müller-Steinhagen *et al.* 2009)

Because of the substantial environmental and economic impacts of fouling, even a rather small decrease in fouling could lead to significant savings if applied broadly. Many methods have been tried to reduce fouling, but quite often they are expensive, bring out harmful environmental effects or the desired result is not achieved (Kazi 2012). Therefore, the most effective method against fouling is its prevention, which requires that the phenomena and the interactions affecting fouling are known.

Fouling of heat transfer surfaces is a complex phenomenon, in which different fouling mechanisms may have interrelated effects. Detailed interactions between depositing substances and surfaces or between fouling mechanisms are still not completely known. To clarify these interactions and sub-processes involved, experimental research, surface characterization, and modeling methods, like Computational Fluid Dynamics (CFD), can be used. A proper fouling model would provide a tool to find preferable operating conditions and to design geometries for process equipment (especially heat exchangers) that are less prone to fouling. This would reduce energy, material and maintenance costs, as well as the environmental impacts of processes.

1.2 The objectives and scope

In this doctoral thesis project, the main goal is to improve the energy efficiency of heat exchangers by providing a better understanding and models for crystallization fouling. The knowledge and tools can then be applied to reduce crystallization fouling on heat transfer surfaces. In order to reach that target, crystallization fouling phenomenon in question needs to be understood. The objectives of the thesis can be summarized as follows:

- To determine the effects of operating conditions on crystallization fouling and to identify the most important parameters affecting crystallization fouling through experiments and modeling.
- To define the sub-processes that control crystallization fouling.
- To develop and validate a crystallization fouling model.
- To quantify the uncertainty of fouling experiments in order to evaluate the reliability of the experiments, but also the accuracy of fouling models.

- To incorporate the crystallization fouling model into CFD to determine accurately the most important parameters affecting crystallization fouling in complicated geometries.
- To study the abatement of crystallization fouling on a patterned surface using the developed methods.

The scope of the thesis is on the crystallization fouling of $CaCO_3$ from aqueous solution on flat and patterned heat exchanger surfaces using experimental and modeling methods to decrease fouling phenomenon and to improve the energy efficiency of processes. The content of the thesis under this scope is presented in Fig. 1.

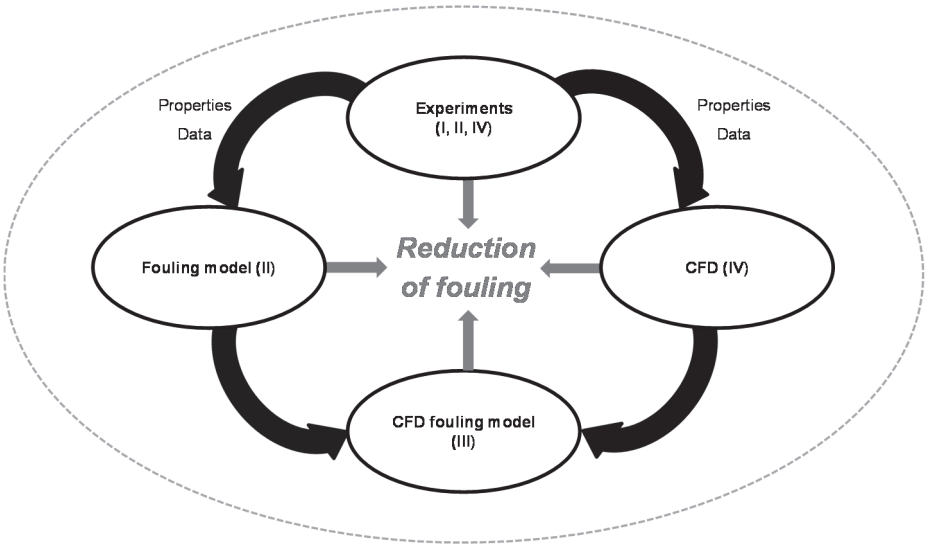

Fig. 1. Content of the thesis.

This thesis consists of four refereed articles, the contributions of which are shown in Fig. 2. Paper I contributes to the experimental part of this thesis in which the effects of the operating conditions are defined. In addition, the experimental uncertainty in the fouling resistance is quantified in Paper I to define the largest sources of uncertainty and to evaluate the reliability of the results. In Paper II, the ex-situ measurements of the fouling layer are used to determine the properties of the fouling layer, which are used to calculate the mass deposition rate from the experimentally obtained fouling thermal resistances. In Paper II, the uncertainty analysis is used to evaluate the accuracy of the properties of the fouling layer and

the mass deposition rate, and suitability of the used method for the definition of the fouling layer properties. In Paper II, also the model parameters for different fouling models are defined using non-linear regression. The sub-process that controls the crystallization fouling is discussed in Papers I and II in the context of experiments and modeling, respectively. In Paper III, the most suitable fouling model defined in Paper II is implemented in CFD. The obtained crystallization fouling CFD model is validated against experimental data, and the model is used to identify the most significant parameters affecting crystallization fouling. Paper IV combines the methods presented in Papers I-III for studying the prevention of crystallization by surface modifications. In Paper IV, the fouling experiments are used to compare fouling behavior of different surface patterns. The most promising surface pattern is then studied by CFD, which gives the values needed to accurately estimate crystallization fouling on that pattern.

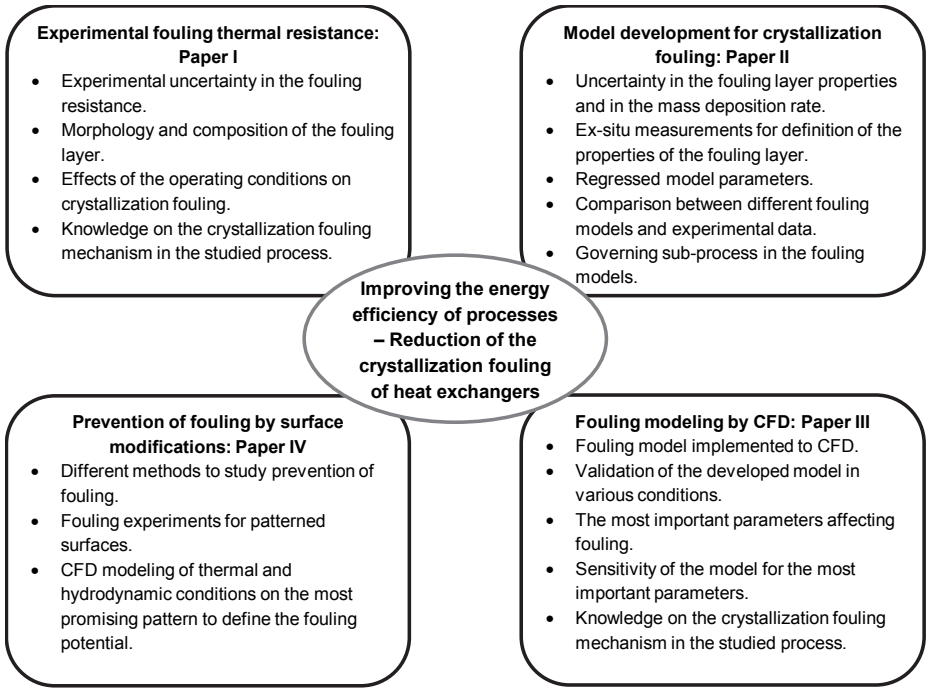

Fig. 2. The contributions of the original papers to the thesis.

2 Background

2.1 Heat exchangers

Temperature differences cause an energy flow, which is called heat transfer. In industrial processes, heat transfer within and between systems is essential for energy-efficient processes. Heat transfer between two or more fluids or between a solid or solid particles and a fluid, having different temperatures, can be performed by heat exchangers. (Shah & Sekulic 1985)

2.1.1 Classification of heat exchangers

In heat exchangers, heat transfer between the fluids occurs usually through a wall that separates the fluids and prevents mixing of the fluids. These heat exchangers are called recuperators. In regenerators, the fluids flow through the same channel in an intermittent manner, without mixing with the other fluid, and the heat transfers via thermal energy storage and is released by the heat transfer surfaces. In addition, there are heat exchangers in which the fluids exchange heat through a direct contact. Other types of heat exchangers are e.g., boilers, steam generators, condensers, radiators, evaporators, cooling towers, heaters and coolers, just to mention a few. (Kraus 2003, Shah & Sekulic 1985)

Heat exchangers may be classified according to the transfer process, construction, flow arrangement, surface compactness, number of fluids, or heat transfer mechanism (Kraus 2003, Shah & Sekulic 1985). One classification is based on the configuration of the fluid flow paths through the heat exchanger to the parallel flow, counter flow, and cross flow heat exchangers. In the parallel flow configuration, the two fluid streams enter and exit the heat exchanger at the same end, and flow in the same direction through the heat exchanger. In the counter flow system, the fluid streams flow in the opposite directions through the heat exchanger. In cross flow heat exchangers, the flow direction is perpendicular. The cross flow heat exchangers may be single pass or multi pass. In the single pass cross flow unit, one fluid flows through the heat exchanger at a certain angle to the flow path of the other fluid. In the multi pass cross flow unit, one fluid stream flows back and forth across the flow path of the other fluid. Quite often, heat exchangers are a combination of the above mentioned types. The choice of the type and the size of a heat exchanger for certain processes is usually

performed based on e.g., the inlet temperature of the fluid streams, pressure, flow velocities, and fluid properties. (Welty 1974: 381–383)

2.1.2 Plate heat exchangers

One of the most common heat exchangers used in industry is the plate heat exchanger (PHE). Plate heat exchangers are closed heat exchangers in which the fluids are flowing in adjacent channels, separated by plates, without mixing with each other. (Welty 1974: 379–380) The plate heat exchanger consists of several, thin, corrugated plates that are compressed together and brazed, welded or sealed with gaskets. The corrugation of the plate is often made in a herringbone pattern, as shown in Fig. 3, which enhances the heat transfer (Wang & Sunden 2003). The plate alternates between an upward and downward herringbone pattern forming complicated flow passages between the plates. The corrugated flow channel generates vortices even at low Reynolds numbers. Therefore, in the corrugated plate heat exchanger, the Reynolds number for turbulent flow is between 100 and 400 depending on the plate type. (Cooper 1980)

Fig. 3. Corrugated heat transfer surface of a plate heat exchanger.

The turbulence caused by the vortices increases convective mass and heat transfer. Corrugations also increase the heat transfer area. Due to these effects, the heat transfer rates of the corrugated plate heat exchangers may be 3–4 times higher than those of a flat plate heat exchanger with the same external dimensions. Because the plates of the corrugated plate heat exchanger are very tightly packed, the specific surface area, i.e. the ratio of the heat transfer area to the volume of the heat exchanger, is also large, which makes plate heat

exchangers small, light, and cost effective compared to other heat exchanger types. The small size also reduces the need of construction and backing materials and space for assembly and maintenance. (Reay 1999: 17–20, 58–59)

Plate heat exchangers may be easily modified based on their needs, they are durable, and have a large number of model options. Plate heat exchangers can be used with heat-sensitive materials since the temperatures in the plate heat exchangers can be controlled accurately. Plate heat exchangers are also very effective; heat transfer effectiveness may be even 95%. Therefore, the temperature difference between the fluids can be low, which reduces the energy costs. (Reay 1999: 17–20, 58–59)

Plate heat exchangers can be used in a wide range of industrial applications, often for liquid-to-liquid heat transfer, like the heating, cooling or heat recovery of process fluids, but also for two phase heat transfer, like condensation and vaporization. (Reay 1999: 17–20, 58–59) Plate heat exchangers are generally not suitable for erosive conditions or for fluids containing fibrous material. Also, plates and gaskets cause some limitations (e.g., high pressure or temperature, highly corrosive application) in the use of plate heat exchangers. These, however, may be overcome in some applications by welding or brazing the plates together instead of sealing them by gaskets, but these methods are not suitable for conditions where fouling might occur because cleaning of such plate heat exchangers is difficult (Cooper 1980). (Shah & Sekulic 1985)

2.1.3 Performance of heat exchangers

The performance of heat exchangers may be estimated using e.g., effectiveness, ϵ,. The effectiveness in heat transfer can be defined as a ratio between the actual heat transfer rate, Q and the maximum heat transfer rate, Q_{max}

$$\epsilon = \frac{Q}{Q_{max}}. \tag{1}$$

For a heat exchanger with two process streams, the heat flow can be defined based on the conservation of energy as

$$Q = C_h\left(T_{h,in} - T_{h,out}\right) = C_c\left(T_{c,out} - T_{c,in}\right), \tag{2}$$

where T is the temperature, and subscripts h and c denote the hotter and colder fluids, and *in* and *out* the inlet and outlet of the heat exchanger, respectively. C is the heat capacity rate defined as

$$C = \dot{m}c_p, \tag{3}$$

where $\dot{m}$ is the mass flow rate, and c_p is the specific heat capacity, both to be defined for hot and cold fluids. The effectiveness can be then written as

$$\epsilon = \frac{C_h(T_{h,out}-T_{h,in})}{C_{min}(T_{h,in}-T_{c,in})} = \frac{C_c(T_{c,out}-T_{c,in})}{C_{min}(T_{h,in}-T_{c,in})}, \tag{4}$$

where $C_{min} = \min\{C_h, C_c\}$. (Kraus 2003)

The effectiveness describes the duty of the heat exchanger for certain flow and temperature conditions, but it does not indicate the size of the heat exchanger needed for the duty. The required size of the heat exchanger can be defined by the following rate equation

$$Q = UA\theta = U_hA_h\theta = U_cA_c\theta, \tag{5}$$

where A is the surface area of the heat exchanger, U is the overall heat transfer coefficient, and θ is the driving temperature difference. The total heat exchange process can be presented for a heat exchanger with flat surface by combining Eqs. 2 and 5 as (Kraus 2003)

$$Q = UA\theta = U_hA_h\theta = U_cA_c\theta = C_h\left(T_{h,in} - T_{h,out}\right) = C_c\left(T_{c,out} - T_{c,in}\right). \tag{6}$$

The overall heat transfer coefficient accounts for all heat transfer resistances that occur during the heat transfer process. The inverse of the overall heat transfer coefficient is a sum of individual resistances to heat flow, and can be written for fouling conditions as

$$\frac{1}{UA} = \frac{1}{h_hA_h} + \frac{x_{fl,h}}{\lambda_{fl,h}A_h} + R_w + \frac{x_{fl,c}}{\lambda_{fl,c}A_c} + \frac{1}{h_cA_c}, \tag{7}$$

where h is the heat transfer coefficient, x is the thickness, λ is the thermal conductivity, R_w is the thermal resistance of the wall material, and *fl* and *w* denote the fouling layer and the heat transfer wall, respectively. The terms on the right hand side of Eq. 7 represent the hot side convective layer resistance, the hot side fouling resistance, the resistance of the heat exchanger wall, the cold side fouling resistance, and the cold side convective layer resistance, respectively. The fouling resistance will be discussed more in subsequent sections. (Kraus 2003)

In order to force streams through the heat exchanger, pumping power is needed. The performance of the heat exchanger compete with the performance of the pumping power since e.g., the increase in the surface area by a structured surface enhances the heat transfer but, on the other hand increases the pressure drop, which increases the required pumping power. In addition, many factors that

depend on the heat exchanger type, such as entrance, exit, contraction, expansion, acceleration and friction effects, influence the required pumping power.

2.1.4 Fouling of heat exchangers

A major problem with heat exchangers is fouling. Fouling reduces the overall heat transfer coefficient since it forms additional resistance to heat transfer, as can be seen from Eq. 7. Fouling also reduces the effectiveness of heat exchangers since the reduced heat transfer lowers the temperature difference between inlet and outlet for the given flow rates. In addition, fouling increases the pressure drop in heat exchangers, which reduces the energy efficiency of the heat transfer process. (Collier 1981)

Fouling mechanisms

Fouling is classified into different mechanisms based on the cause of fouling. These are crystallization fouling (also called scaling or precipitation), particulate fouling (including sedimentation), chemical reaction fouling, and biofouling. (Bott 1995, Collier 1981)

Crystallization fouling is usually caused by the deposition of inversely soluble salts (such as $CaCO_3$, $CaSO_4$, or Na_2SO_4 in water) on a heated surface, since the solubility of inversely soluble salts decreases with temperature. Freezing may also be classified as a form of crystallization fouling. Freezing occurs when pure liquid or one component in the liquid crystallizes to a subcooled heat transfer surface. (Collier 1981) Crystallization fouling is studied in this thesis, and therefore, described in more detail in Section 2.2.

Particulate fouling is the accumulation of, often colloidal, particles on a heat transfer surface in liquid or gas systems. One common example in liquid based systems is cooling with natural water, which often contains particulate matter, such as silt, that accumulates on a heat exchanger surface. Also, some process slurries may cause depositions on the surface. In gas systems, e.g., dust particles in air blown coolers or incombustible mineral residues of the fuel within the combustion gases may cause deposition on the walls. (Bott 1995) Sedimentation is one form of particulate fouling, and it is referred to as settling (e.g., sand, rust or clay on process equipment) (Collier 1981).

Chemical reaction fouling occurs when chemical reactions take place in the bulk fluid or at the surface to form products that deposit on the surfaces.

Polymerization, cracking or coking of hydrocarbons at high temperatures are examples of chemical reactions taking place within the fluid stream that causes the fouling of surfaces. On the other hand, corrosion causes fouling, which involves a reaction between the surface and the fluid (e.g., corrosion in waste heat boilers). (Collier 1981)

In biofouling bio-organisms, like plants, animals, algae, or bacteria accumulate and grow on the surface. Biofouling is common e.g., in heat exchangers using sea water. (Cooper 1980)

Fouling may also be a combination of different mechanisms. Composed fouling includes more than one foulant or fouling mechanism, which interact with each other.

Fouling prevention and cleaning of heat exchangers

The best strategy for fouling would be to prevent it. However, total prevention of fouling is rarely possible. The formation of fouling layers might be reduced by operational means, i.e. by optimization of the process and by steady operation of the process in favorable conditions. These could be possible to achieve by suitable plate design and materials, proper temperatures, pressures, and flow velocities. (Cooper 1980)

In addition to operational methods, chemicals can be used as additives to prevent fouling, or as cleaning agents to remove fouling layers. The additives may be used as sequestering agents, threshold agents, crystal modifiers, dispersants or corrosion inhibitors to prevent fouling. Also, seeding may be used to reduce crystallization fouling. Unfortunately, the use of chemical additives or detergents may lead to contamination of the product or may have harmful environmental impacts or safety hazards for employees. (Kazi 2012)

Generally, fouling cannot be totally prevented. Therefore, cleaning or other methods to reduce fouling are needed. Traditional mechanical methods, such as scraping or brushing, can be used to remove fouling layers from heat exchangers surfaces. However, these methods are expensive (due to the required labor and process shut downs), and can be used only for limited applications. Some other methods to remove or reduce fouling are: increasing the flow velocity for a short period of time to increase the shear stress, reversing the flow direction, pulsating the flow, using turbulence promoters, passing cleaning devices through the flow channels, overheating for short time to cause breakage due to differential thermal expansion of the heat transfer surface and deposits, vibrating (mechanical or

acoustic) the heat transfer surface, and modifying (physical or chemical) the surface roughness and surface materials. In addition to the above mentioned methods, magnetic, electric, ultrasound or radiation treatment have been proposed to mitigate fouling. (Kazi 2012)

2.2 Crystallization fouling

2.2.1 Mechanism of crystallization

Crystallization fouling occurs in many industrial applications. Crystallization fouling is caused by dissolved salts that precipitate out of the solution. Three sequential stages can be distinguished in the crystallization process: 1) appearance of supersaturation, 2) nucleation of crystals, and 3) growth of crystals. The supersaturation is therefore a prerequisite for crystallization. Supersaturated conditions may result due to a change in temperature, evaporation of water, addition of solute, mixing of two streams, presence of impurities in the solution, or change in pH or pressure. (Bott 1995, Hasson 1981, Stumm & Morgan 2012)

The salts causing crystallization fouling may have normal (e.g. $NaNO_3$, NaCl) or inverse ($CaCO_3$, $CaSO_4$) solubility. The solubility of the normal solubility salts increases as the temperature increases, whereas the solubility of the inversely soluble salts decreases with the increasing temperature. The concentration of the inversely soluble salts, as used in this thesis, may be illustrated using Fig. 4, which presents the concentration behavior of inversely soluble salts during heating. (Bott 1995)

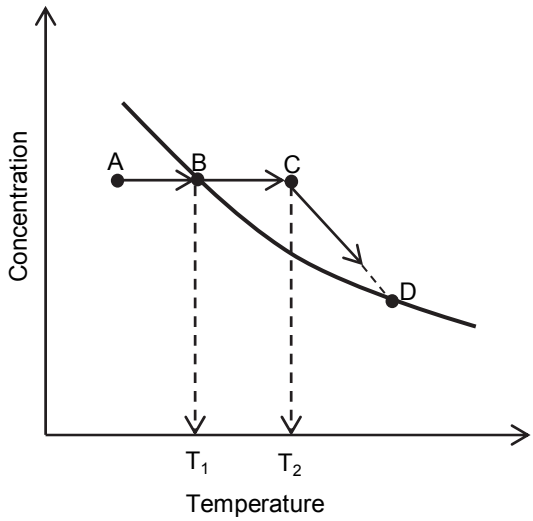

Fig. 4. Concentration behavior of inversely soluble salt during heating (modified from (Bott 1995)).

In Fig. 4, at point A, the solution is under-saturated. When the solution is heated up to temperature T_1, the solubility limit (point B) is reached and the solution becomes saturated. If the heating is continued, the solution will be supersaturated. At point C, the temperature reaches the limit when crystallization begins. After that, further heating will decrease the concentration as the ions crystallize out of the solution, and the equilibrium moves towards point D. (Bott 1995)

Crystallization may take place on a surface or in the bulk fluid (Schreier & Fryer 1995), however, bulk crystallization requires the presence of impurities or higher supersaturation than surface crystallization. Homogeneous nucleation and the growth of crystals in the bulk fluid may occur in a reasonable time if a critical supersaturation degree is obtained (Mullin 2001: 185). Bulk crystallization may occur spontaneously in the primary nucleation zone, which has been defined based on the pH value and Ca^{2+} concentration for the $CaCO_3$-CO_2-H_2O system by Elfil and Roques (2004). In the metastable zone, the bulk fluid is supersaturated but the homogeneous nucleation to the bulk fluid is unlikely, and impurities or seeds are required for the crystallization in the bulk fluid (Elfil & Roques 2004).

Bulk crystallized particles and other solid material in the bulk fluid, such as non-crystallized, inert particles, affect the crystallization fouling rate on surfaces

(Bansal *et al.* 2003, Pääkkönen *et al.* 2009, Sheikholeslami 2000) (Paper I). The solid material in the solution may either increase or mitigate crystallization fouling on the surface. According to Andritsos and Karabelas (2003) fine aragonite particles increase the fouling rate of calcium carbonate. In contrast, TiO_2 particles had no significant effect on the fouling rate, but changed the morphology and reduced the strength of the fouling layer, which may increase the removal of the deposition from the surface. Corresponding results were obtained by Bansal *et al.* (Bansal *et al.* 1997, Bansal *et al.* 2001) for calcium sulfate fouling. Hasson and Karman (1983) found that crystallized calcium carbonate particles did not have any significant effect on the surface crystallization rate. Therefore, in order to study only the surface crystallization, the presence of impurities in the system should be avoided.

2.2.2 Crystallization fouling of $CaCO_3$

Calcium carbonate ($CaCO_3$) is a salt, which commonly causes crystallization fouling e.g., in cooling and drinking water systems and in desalination processes. (Andritsos & Karabelas 2003, Bott 1997) Calcium carbonate is inversely soluble, which means that its solubility decreases as the temperature increases (Hasson *et al.* 1968, Helalizadeh *et al.* 2000). Therefore, the heated surfaces of heat exchangers are prone to $CaCO_3$ crystallization fouling.

The overall surface crystallization process of calcium carbonate can be presented as

$$Ca^{2+} + 2HCO_3^- \rightarrow CaCO_{3(s)} + CO_2 + H_2O. \quad (8)$$

The overall crystallization process composes of the crystallization reaction (Eq. 9) and the carbonate reactions (Eqs. 10 and 11). Also, some other minor species are involved but their influence is negligible in many practical applications. (Segev *et al.* 2012)

$$Ca^{2+} + CO_3^{2-} \leftrightarrow CaCO_{3(s)} \quad (9)$$

$$H^+ + HCO_3^- \leftrightarrow CO_2 + H_2O \quad (10)$$

$$HCO_3^- \leftrightarrow H^+ + CO_3^{2-}. \quad (11)$$

The presence of hydrogen ions shows that the solubility of calcium carbonate is sensitive to the pH value of the solution. Therefore, changes in the pH value may lead to supersaturated conditions even when the temperature remains constant. In addition to pH, the presence of other chemical species in the solution may affect the solubility. (Bott 1995)

Calcium carbonate has three polymorphs: calcite, aragonite and vaterite. The temperature dependency of the solubility of different polymorphs has been presented by Plummer and Busenberg (1982). According to those authors, calcite is thermodynamically the most stable polymorph of calcium carbonate, followed by aragonite. Aragonite may also transform to calcite (Sawada 1997, Sheikholeslami & Ng 2001). Vaterite is the least stable, and therefore has the highest solubility of the polymorphs.

2.2.3 Sub-processes governing surface crystallization fouling

In the crystallization fouling of heat exchanger surfaces, several processes take place simultaneously: (a) bulk diffusion of ions through the boundary layer of the fluid, and the porous fouling layer, (b) diffusion of solute ions at the surface, (c) partial or total dissolution of ions, (d) integration of ions into the crystal lattice, and (e) counter diffusion of water through the adsorption and boundary layers. Instead of studying the detailed fouling process, these steps may be combined together into more general sub-processes, which also take into account the hydrodynamic and thermal conditions that control the detailed processes. (Bott 1995)

In the case of surface crystallization, the net mass deposition rate during the linear growth of the fouling layer is a result of 4 main sub-processes or steps. These processes are depicted in Fig. 5 (a) as follows: (A) transport of the ions from the bulk fluid to the adjacent area of the surface, (B) attachment of the material to the surface, i.e. surface integration, (C) probability of the attachment of the ions to the surface influenced by the residence time of the fluid at the wall (Epstein 1994), and (D) removal of the fouling layer from the surface. (Hasson *et al.* 1968, Helalizadeh *et al.* 2000, Mullin 1961: 115–128) Aging of the deposition layer may also take place especially if a longer time period is observed (Kazi 2012). The sub-processes are introduced in more detail in the following sections.

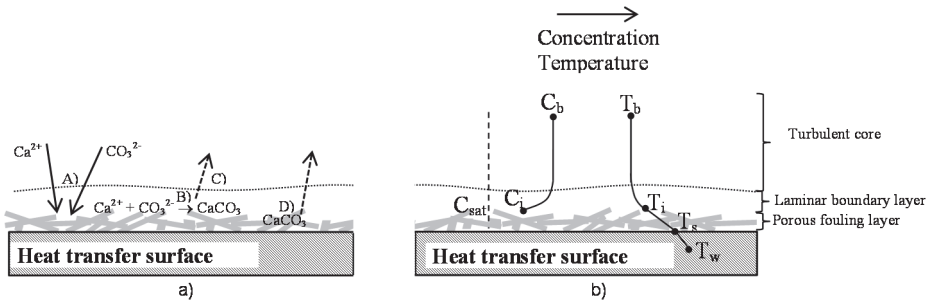

Fig. 5. Schematic of the sub-processes in crystallization fouling mechanism (a), and the concentration and temperature profiles in the system (b). Sub-process (A) represents mass transfer of ions to the surface, (B) represents surface integration, (C) represent probability of ions to adhere to the surface depending on the residence time of the fluid at the wall, and (D) represents removal of crystals from the porous fouling layer (modified from Paper I, published by permission of Elsevier).

Mass transfer

The transport of ions to the surface, step (A) in Fig. 5 (a), is due to convective mass transfer and associated with the transport of the ions through the boundary layer to the surface. The mass transport is driven by the concentration difference between the bulk fluid (C_b) and the interface (C_i), and can be described by

$$m_d = \beta(C_b - C_i), \tag{12}$$

where m_d is the mass deposition rate, β is the mass transfer coefficient, C_b and C_i are the bulk and interfacial concentrations, respectively. (Hasson *et al.* 1968, Krause 1993)

As can be seen from the concentration profile in Fig. 5 (b), the concentration decreases when the fouling layer is approached. Supersaturation is a prerequisite for crystallization fouling, and therefore, the interfacial concentration (C_i) at the interface between the fluid and the fouling layer is higher than the saturation concentration (C_{sat}).

Surface integration

The attachment step (B) in Fig. 5 (a), includes the chemistry of the solid-liquid interface, physics of the heterogeneous nucleation, local thermodynamics, and hydrodynamics (Helalizadeh *et al.* 2005). Since modeling of these phenomena in detail would be complicated, the integration of the ions to the crystal lattice is usually described by a temperature dependent chemical reaction (Bott 1995), which is driven by the n^{th} order of the concentration difference between the interfacial (C_i) and the saturation (C_{sat}) concentrations as follows

$$m_d = k_r(C_i - C_{sat})^n, \tag{13}$$

where k_r is the rate coefficient for the surface integration, which is often described by the Arrhenius type rate equation (Bott 1997, Hasson *et al.* 1968, Helalizadeh *et al.* 2005, Krause 1993, Mwaba *et al.* 2006b)

$$k_r = k_0 e^{-E_a/RT_i}, \tag{14}$$

where k_0 is the pre-exponential factor, E_a is the activation energy, R is the universal gas constant, and T_i is the interfacial temperature.

As can be seen from the temperature profile in Fig. 5 (b), temperature increases towards the surface. The interfacial temperature (T_i) corresponds to the surface temperature (T_s) when the surface is clean. The difference between the surface and interfacial temperature increases as the fouling layer grows on the surface. If the heat transfer rate through the surface is constant (as assumed in this thesis), the surface temperature will increase as the thickness of the fouling layer increases, but the interfacial temperature remains nearly constant (Hasson *et al.* 1968, Mwaba *et al.* 2006c). However, the evolving roughness of the fouling layer may increase the film heat transfer coefficient, which further decreases the interfacial temperature.

Probability of the attachment

According to Epstein (Epstein 1994), the residence time of the fluid at the wall affects the probability of the fouling material to adhere to the surface. The residence time (C) in Fig. 5 (a), may be taken into account through a time scaling factor (Epstein 1994)

$$t_{sf} = \frac{\mu_f}{(\rho_f V^2)}, \tag{15}$$

where μ_f and ρ_f are the viscosity and the density of the fluid, respectively, and V is the friction velocity defined for the smooth surfaces as

$$V = \sqrt{\frac{\tau_w}{\rho_f}} = v\sqrt{\frac{f}{2}}, \tag{16}$$

where τ_w is the wall shear stress, v is the flow velocity, and f is the Fanning friction factor, which is calculated at the film temperature.

The time scaling factor has been earlier applied to fouling in protein (Rose *et al.* 2000), and $CaSO_4$ (Fahiminia *et al.* 2007) solutions, in addition to chemical reaction fouling (Epstein 1994). In this thesis, the time scaling factor is applied to the crystallization fouling of $CaCO_3$.

Removal from the surface

The removal of the depositions from the surface, m_r, (D) in Fig. 5 (a) is related to the shear strength of the fouling layer and the shear stress of the fluid flow as was defined by Bohnet (1987) and applied by Brahim *et al.* (2003) for $CaSO_4$ depositions

$$m_r = 83.2w^{0.54}\rho_{fl}(1 + \delta\Delta T)d_p\left(\rho_f^2\mu_f g\right)^{1/3} x_{fl}w^2, \tag{17}$$

where w is the mean fluid velocity in the flow channel, ρ_{fl} is the density of the fouling layer, δ is the linear expansion coefficient, d_p is the mean crystal diameter, g is the gravitational acceleration, and x_{fl} is the thickness of the fouling layer.

Another way to model the removal was proposed by Bansal *et al.* (2005) who incorporated the formation of the turbulent bursts, including area, efficiency, and frequency of the turbulent burst, to the removal.

In addition, e.g., Kern and Seaton (1959) have presented the following removal model based on the removal rate coefficient, k_{rem}

$$m_r = -k_{rem} f \frac{1}{2} \cdot \rho_f \cdot v_f^2. \tag{18}$$

Removal from the surface is neglected in this thesis, because calcium carbonate forms tenacious depositions that are hard to remove from the surface (Andritsos & Karabelas 2003, Lee *et al.* 2006). In addition, the thin fouling layers occurring during the early stage of the fouling process, as in this work, do not affect the cross sectional area of the flow channel, and therefore, the removal of the deposits from the surface is minor (Bansal *et al.* 2008, Bansal & Müller-Steinhagen 1993). Also, experimental evidence supports this assumption, since

asymptotic fouling curves were not detected in the surface crystallization experiments (Paper I).

2.2.4 Overall fouling model

Many fouling models are based on the approach of Kern and Seaton (1959) who defined the net rate of the formation of deposits as a result of two competing processes, i.e. the formation and removal of deposits

$$\frac{dm}{dt} = m_d - m_r, \tag{19}$$

where *dm*/*dt* is the overall mass deposition rate. The formation of the deposits may involve the following sub-processes: processes in the bulk fluid, transport to the heat transfer surface, and attachment of the deposits to the surface. The removal may involve dissolution, re-entrainment, or spalling of the material from the surface. (Somerscales & Knudsen 1981) The general fouling models, as the one proposed by Kern and Seaton (1959) (Eq. 19), need case-specific reformulation, in which all of the relevant phenomena occurring in the studied case, and information of physical properties and kinetic data, are included.

Before combining the sub-processes described in the previous section into an overall fouling model, it is important to evaluate the relative importance of each sub-process to determine if the mass deposition rate is limited by one of the sub-processes.

If one sub-process limits the fouling process, it is said to control the fouling. Many researchers have found that crystallization fouling is controlled by surface integration (Augustin & Bohnet 1995, Bansal & Müller-Steinhagen 1993, Mwaba *et al.* 2006a, Mwaba *et al.* 2006b). In contrast, Hasson *et al.* (1968) found that mass transfer controls the crystallization fouling of tap water. Some researchers have proposed that mass transfer controls fouling at low flow velocities, and that the control shifts to surface integration as the flow velocity increases (Fahiminia *et al.* 2007, Helalizadeh *et al.* 2000, Najibi *et al.* 1997b). Overall, it is clear that both the operating conditions and the process fluid (crystallizing ions, presence of particles etc.) affect the controlling mechanism.

The controlling step in crystallization fouling can be found by plotting the mass deposition rates at the constant surface temperature as a function of flow velocity, as denoted in Fig. 6 by a solid line. When the mass transfer rate is low compared to the rate of surface integration, and the mass transfer controls the

fouling process, increasing the velocity increases the mass deposition rate. On the other hand, when the mass transfer rate is much higher than the rate of surface integration (i.e. the surface integration controls fouling), the mass deposition rate remains constant or even decreases as the flow velocity increases. The decreasing mass deposition rate with an increasing flow velocity, may be attributed to the increased removal at higher flow velocities (Bansal *et al.* 2000), or to the decreasing residence time of the fluid at the wall, which reduces the probability of the attachment to the surface (Epstein 1994, Fahiminia *et al.* 2007, Rose *et al.* 2000) (Paper I).

It is proposed in the literature (Epstein 1994, Fahiminia et al. 2007, Rose et al. 2000) that the mass transfer controls fouling at low flow velocities, and at some flow velocity, the maximum in the fouling rate is achieved. The fouling rate begins to decrease after the maximum point as the flow velocity is increased. The maximum fouling rate is higher the higher the wall temperature is, because the attachment of the foulants to the surface at a certain flow velocity is more probable at higher wall temperatures. The maximum point of the fouling rate occurs at the higher flow velocity the higher the wall temperature is, because the higher the fouling rate is, the shorter residence time is required to overcome the effect of the wall temperature on the fouling rate. (Rose et al. 2000) This behavior is illustrated in Fig. 6 for higher (solid curve) and lower (dashed curve) wall temperatures.

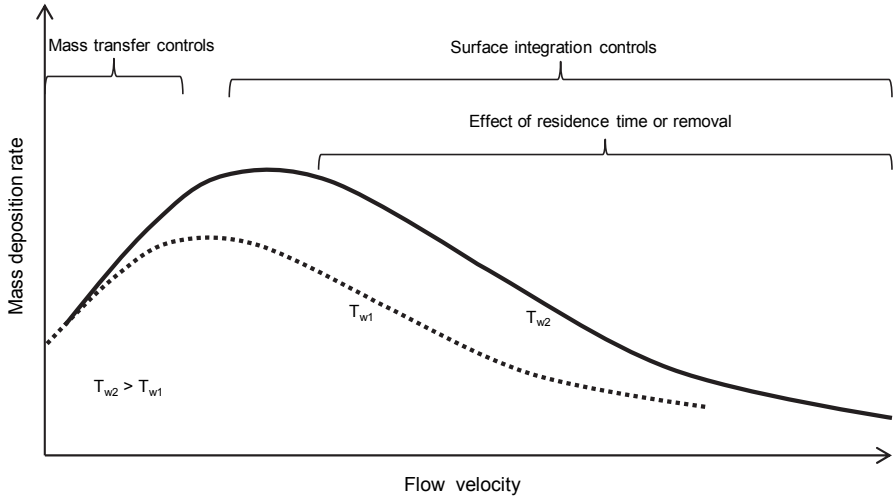

Fig. 6. Schematic of the controlling fouling mechanism. The sub processes refer to the solid curve. Dashed curve shows an example of the fouling behavior at the lower temperature.

Surface integration controlled fouling model

If surface integration controls crystallization fouling, the mass transfer term (Eq. 12) can be neglected in the model (Augustin & Bohnet 1995, Bansal & Müller-Steinhagen 1993), and Eq. 13 may be used to describe the fouling process. In the surface integration controlled fouling, the interfacial concentration (C_i) in Eq. 13 is assumed to correspond to the bulk concentration (C_b) because mass transfer from bulk fluid to the surface is assumed to be infinite (Mwaba *et al.* 2006a). According to Helalizadeh *et al.* (2005) and Augustin and Bohnet (1995), the reaction order (n) may be assumed to be two. Therefore, the following model for the surface integration controlled mass deposition rate is obtained

$$m_d = k_r(C_b - C_{sat})^2 = k_0 e^{-E_a/RT_i}(C_b - C_{sat})^2. \qquad (20)$$

Model including mass transfer and surface integration

Mass transfer from the bulk fluid to the vicinity of the surface may restrict the fouling process especially at low flow velocities. In order to take into account the

effect of mass transfer, Eq. 12 needs to be integrated in the model. By summing Eqs. 12 and 13, the following model for the mass deposition rate is attained (Brahim *et al.* 2003, Helalizadeh *et al.* 2005, Krause 1993, Mwaba *et al.* 2006c)

$$m_d = \beta\left[\frac{1}{2}\left(\frac{\beta}{k_r}\right) + (C_b - C_{sat}) - \sqrt{\frac{1}{4}\left(\frac{\beta}{k_r}\right)^2 + \frac{\beta}{k_r}(C_b - C_{sat})}\right]. \quad (21)$$

Models including the probability of the attachment

If the probability of the attachment using the residence time of the fluid at the wall is included in the models in Eqs. 20 and 21, the following model is obtained for surface crystallization fouling that considers the surface integration only

$$m_d = k_r'(C_b - C_{sat})^2 \frac{\mu_f}{\rho_f V^2}, \quad (22)$$

where k_r' is rate coefficient (Paper II).

When both the surface integration and the mass transfer are considered, the model is presented as (Paper II)

$$m_d = \beta\left[\frac{1}{2}\left(\frac{\beta\rho_f V^2}{k_r'\mu_f}\right) + (C_b - C_{sat}) - \sqrt{\frac{1}{4}\left(\frac{\beta\rho_f V^2}{k_r'\mu_f}\right)^2 + \frac{\beta\rho_f V^2}{k_r'\mu_f}(C_b - C_{sat})}\right]. \quad (23)$$

The models need several variables to be defined. These are: 1) the mass transfer coefficient for which the diffusion coefficient, density, viscosity, flow velocity and the dimensions of the modeled system are needed; 2) the friction velocity for which the shear stress or friction factor is required; 3) the rate coefficient for the surface integration for which the interfacial temperature, pre-exponential factor and activation energy are needed; 4) and the bulk and saturation concentrations. The flow velocity, bulk concentration, temperatures, and the dimensions are set by the modeled system. Non-linear regression can be used to define the rate coefficient for the surface integration (pre-exponential factor and activation energy). The temperature dependency of the fluid properties, such as density, viscosity, diffusion coefficient, and saturation concentration, can be found from the literature. In order to define the mass transfer coefficient and the friction velocity, transport processes need to be modeled.

The crystallization fouling models presented above are influenced by the hydrodynamic and thermal conditions of the system. In addition, the models are related to the thermodynamics, chemical kinetics and material properties.

(Helalizadeh *et al.* 2000) Therefore, the fouling behavior of a single foulant may vary depending on the system and the operating conditions; but in order to reduce fouling, it is important to understand the fouling behavior of the specific process and practical application.

2.3 Transport processes in heat exchangers

The following sections present the basic phenomena and related equations needed in the modeling of a flow system in which fouling occurs. The velocity, temperature and concentration fields within a heat exchanger can be described by mathematical equations, which are derived from the conservation laws of the mass, momentum, energy and chemical species.

Continuity equation for the fluid flow can be derived from the conservation of mass, for the unsteady, three dimensional, and compressible fluid flow as

$$\frac{\partial \rho}{\partial t} + \nabla \cdot (\rho \vec{v}) = \mathrm{S}_m, \tag{24}$$

where ρ is the density of the fluid, t is time, $\vec{v}$ is the velocity vector, and S_m is the source term. In this thesis, the source term is determined from the fouling model (see Section 2.2.4). The first term on the left hand side represents the density fluctuation with respect to time, and the second term the convective transport. (Bird *et al.* 1960: 74–75, Versteeg & Malalasekera 1995: 12–13)

2.3.1 Momentum transfer

The momentum equation (Eq. 25) is derived from Newton's second law according to which the rate of change in momentum is equal to the sum of forces acting on the fluid element, which can be presented in the vector form as follows

$$\frac{\partial}{\partial t}(\rho \vec{v}) + \nabla \cdot (\rho \vec{v} \vec{v}) = -\nabla p - \nabla \cdot (\bar{\bar{\tau}}) + \rho \vec{g} + \vec{F}, \tag{25}$$

where p is pressure, $\bar{\bar{\tau}}$ is the shear stress tensor, $\vec{g}$ is the gravitational acceleration vector, and $\vec{F}$ is the external body force vector, which may also include other model-dependent sources. On the left hand side, the first term describes the rate of change of momentum with time, and the second term is the rate of change of momentum gain by advection. On the right hand side, the first term is the pressure gradient, the second term represents the rate of change of momentum by viscous

transfer, the third term is the gravitational force, and the last term the external force. (Bird *et al.* 1960: 78) The stress tensor may be given by

$$\bar{\bar{\tau}} = -\mu\left[(\nabla\vec{v} + \nabla\vec{v}^T) + \frac{2}{3}\nabla\cdot\vec{v}I\right], \tag{26}$$

where μ is the molecular viscosity, I is the unit tensor. The second term on the right hand side is the effect of volume deformation. (ANSYS Inc. 2011a: 3, Versteeg & Malalasekera 1995: 22)

When the fluid flows in the x-direction between two, stagnant plates perpendicular to y-direction such that v_x is a function of y alone, the stress tensor will simplify to

$$\tau_{yx} = -\mu\frac{dv_x}{dy}, \tag{27}$$

which is called Newton's law of viscosity. Eq. 27 states that the shear stress is proportional to the negative of the local velocity gradient. According to this law, which is applicable to all gases and simple liquids, i.e. to the Newtonian fluids, moving fluid "layers" transfer x-momentum to the adjacent layers in the y-direction. (Bird *et al.* 1960: 4–6) When the distance from the surface (y) increases, the x-component of the fluid increases as a hydrodynamic boundary layer is formed at the wall. In the hydrodynamic boundary layer, the velocity gradients and the shear stress are large, whereas outside the boundary layer, they are negligible. (Incropera & DeWitt 1996: 289–290)

The surface shear stress is related to the surface frictional effects. The friction coefficient (also called the Fanning friction factor) may be determined as

$$f = \frac{\tau_w}{\rho v_m^2/2}, \tag{28}$$

where τ_w is the wall shear stress, and v_m is the mean fluid velocity. (Incropera & DeWitt 1996: 290, 424) The friction factor depends on the Reynolds number, Re, and the ratio of length and diameter of the flow channel. The Reynolds number represents the ratio of inertia and viscous forces in the velocity boundary layer, and is defined as

$$Re = \frac{\rho v L}{\mu}, \tag{29}$$

where L is the characteristic length. The friction factors may be determined based on the Reynolds number and relative roughness of the surface using empirical or analytical correlations or e.g., the Moody diagram. (Bird *et al.* 1960: 184–187)

In this thesis, CFD is used for the solution of the continuity (Eq. 24) and momentum (Eq. 25) equations to obtain a velocity field of the system. The shear stress, which is needed for the fouling model, is either modeled by CFD from the velocity gradients (Papers III and IV) or defined using the following friction factor correlation for a turbulent flow in a smooth tube (Bird *et al.* 1960: 186) (Paper II)

$$f = \frac{0.0791}{Re^{1/4}}. \quad (30)$$

2.3.2 Energy transfer

The energy conservation equation (Eq. 31) is derived from the first law of thermodynamics, which defines that the rate of change of energy of the fluid is equal to the net rate of heat transfer within the fluid and net rate of work done to fluid

$$\rho\left(\frac{\partial E}{\partial t} + \vec{v}\cdot\nabla E\right) = -\nabla\cdot\vec{q} + \rho\vec{v}\cdot\vec{g} - \nabla\cdot(p\vec{v}) - \nabla\cdot(\bar{\bar{\tau}}\cdot\vec{v}) + S_h, \quad (31)$$

where E is the specific energy, which is the sum of the internal and kinetic energies, q is the heat flux and S_h is the source term. The first term in the left hand side of Eq. 31 is the rate of gain of energy, the second term is the rate of energy transfer by advection. The first term on the right hand side represents the rate of energy input by conduction (q is heat flux), and the second, third and fourth terms are work done by gravitational forces, pressure forces, and viscous forces, respectively. (Bird *et al.* 1960: 311–314, Versteeg & Malalasekera 1995: 19–20) Quite often, the work terms on the right hand side of Eq. 31 may be neglected and only the heat transfer by conduction is included in the right hand side of the energy conservation equation.

In heat exchangers, heat may also be transferred by radiation (Incropera & DeWitt 1996: 2) but usually conduction and convection are the prevailing mechanisms, and radiation can be neglected. In addition, the nuclear and electromagnetic energies are ignored here.

Conduction

Heat transfer by conduction is an important term in the energy conservation equation (Eq. 31). Heat conduction is a process induced by molecules where heat diffuses through a stagnant medium that may be a solid or a stationary fluid.

Conduction takes place via molecular interactions whereby molecules at a higher energy level transfer energy to the molecules at the lower energy level. This kind of heat diffusion occurs in amorphous solid materials, liquids and gases. In solids that are organized to a lattice structure, heat transfer occurs via lattice vibration. Conduction may also occur via free electrons. The ability to conduct heat is directly proportional to the amount of free atoms, which makes pure metals good conductors. According to the second law of thermodynamics, the heat transfers to the direction of the negative temperature gradient, i.e. from a higher temperature to a lower temperature. (Welty 1974: 1–2)

The rate at which heat transfers in conduction is described by Fourier's law which in the vector form is

$$\vec{q} = \frac{\vec{Q}}{A} = -\lambda \nabla T, \tag{32}$$

where $\vec{q}$ is the heat flux vector, which is the heat flow rate vector $\vec{Q}$ in the direction of the temperature gradient vector ∇T, per unit heat transfer area A, and λ is the thermal conductivity of the material. The negative sign accounts for the fact that the heat transfers in the direction of the decreasing temperature gradient. (Incropera & DeWitt 1996: 4, Welty 1974: 2)

The thermal conductivity of the material determines its suitability for the given application. The thermal conductivity of gases depends significantly on temperature and pressure, whereas in liquids and solids the thermal conductivities are largely independent of the pressure and usually less dependent on temperature than gases. (Welty 1974: 3–7) Solid materials have generally higher thermal conductivity than liquids and gases because the motion of the molecules is more random and the intermolecular spacing is larger for fluids than for solids. Gases have the lowest thermal conductivity because of the large distances between molecules. (Incropera & DeWitt 1996: 46–49)

Convection

Convective heat transfer takes place between a surface or interface and a fluid in motion. Convective transport is a combination of two mechanisms: macroscopic bulk motion of the fluid and random motion of the molecules (diffusion). Diffusion dominates near the surface where the flow velocity is low. The motion of the fluid may be caused by an external force, such as a pump or a fan, which is called forced convection. If the flow motion is induced by buoyancy forces,

which are caused by the density differences occurring due to temperature variations in the fluid, the energy transport mechanism is called natural (or free) convection. (Incropera & DeWitt 1996: 5–6) In addition to the internal energy transfer, latent heat exchange may take place in the convection process. The latent heat exchange is typically associated with the phase change e.g., in boiling or condensation. (Incropera & DeWitt 1996: 7)

The rate equation for the convection is called Newton's law

$$q = h(T_s - T_f), \tag{33}$$

where T_s is the temperature of the surface, T_f is the temperature of the bulk fluid (or the average temperature in the cross section), and h is the convective heat transfer coefficient. The convective heat transfer coefficient depends on the nature of the fluid motion, thermodynamic and transport properties of the fluid, and the surface geometry, which all affect the conditions in the boundary layer forming due to interaction between the fluid in motion and the bounding surface of different temperatures. The temperature difference between the surface and the fluid induces a thermal boundary layer the size of which may differ from the size of the hydrodynamic boundary layer. (Incropera & DeWitt 1996: 5–7)

The dimensionless convective heat transfer coefficient, the Nusselt number (*Nu*), is a function of geometry, and the Reynolds (*Re*) and the Prandtl (*Pr*) numbers

$$Nu = \frac{h\,L}{\lambda_f} = f(Re, Pr, geometry), \tag{34}$$

where λ_f is the thermal conductivity of the fluid. The Prandtl number relates to the momentum diffusivity, ν, and the thermal diffusivity, α, therefore providing a measure of the relative effectiveness of momentum and energy transport by diffusion in the hydrodynamic and thermal boundary layers (Incropera & DeWitt 1996: 318–320)

$$Pr = \frac{\nu}{\alpha} = \frac{c_p \mu}{\lambda}. \tag{35}$$

A large number of Nusselt number correlations can be found from the literature for different applications. (Bird *et al.* 1960)

2.3.3 Mass transfer

Mass transfer is the movement of species due to a concentration difference or thermodiffusion. For multicomponent systems, the continuity equation for species A can be presented in the following form

$$\frac{\partial}{\partial t}(\rho Y_A) + \nabla(\rho \vec{v} Y_A) = -\nabla \cdot \vec{J}_A + \mathrm{R}_A + \mathrm{S}_A, \tag{36}$$

where Y_A is the mass fraction, $\vec{J}_A$ is the diffusion flux, R_A is the net rate of production of species, and S_A is the source term of species A. The source term in this thesis is a sink of the species A due to crystallization fouling. (ANSYS Inc. 2011a: 197–198, Bird *et al.* 1960: 555–557)

Diffusion mass transfer

The species continuity equation (Eq. 36) requires information about the diffusion flux. The rate equation for mass diffusion is known as Fick's Law. In a binary mixture of species A and B it can be presented in the vector form as follows

$$\vec{J}_A^* = -\mathrm{c} D_{AB} \nabla x_A, \tag{37}$$

where J^*_A is the molar diffusion flux of species A, c is the molar density of the solution, x_A is the mole fraction of species A, and D_{AB} is the binary diffusion coefficient, which corresponds to the thermal conductivity in the conduction heat transfer. (Bird *et al.* 1960: 502).

The diffusion of ionic solution is controlled by the slower moving ions. The solution ionic strength also affects diffusion, but the effect is negligible if the total amount of dissolved solids is less than 6 g/l. (Segev *et al.* 2012) The temperature dependency of the diffusion coefficient can be determined from the following relation, when D is known at temperature T_1

$$\frac{D(T)}{D(T_1)} = \frac{\eta(T_1)}{\eta(T)} \frac{T}{T_1}, \tag{38}$$

where η is the shear viscosity. (Zeebe 2011)

Convective mass transfer

In convective mass transfer, the bulk fluid motion combines with the diffusion of species. The convection takes place if a fluid containing species A, with bulk concentration $C_{A,b}$ flows over a surface where the concentration of species is $C_{A,s}$,

which differs from the bulk concentration (i.e., $C_{A,s} \neq C_{A,b}$). The molar flux of species A, can be expressed by

$$J_A^* = \beta\left(C_{A,s} - C_{A,b}\right), \tag{39}$$

where β is the convection mass transfer coefficient, which is needed in the fouling model (see Section 2.2.3). (Incropera & DeWitt 1996: 285–286) The dimensionless convective mass transfer coefficient, the Sherwood number (*Sh*), may be correlated as a function of geometry, and the Reynolds (*Re*) and the Schmidt numbers (*Sc*)

$$Sh = \frac{\beta \cdot L}{D_{AB}} = f(Re, Sc, geometry). \tag{40}$$

The Schmidt number relates to the momentum and mass diffusivities and is expressed as

$$Sc = \frac{\mu}{\rho \cdot D_{AB}}. \tag{41}$$

Numerous correlations have been developed for the Sherwood number in different applications. The Sherwood number for the flow between parallel plates, which is needed in this thesis, can be defined as (Brahim *et al.* 2003)

$$Sh = 0.034 Re^{0.875} Sc^{1/3}. \tag{42}$$

2.3.4 Transport in the entrance region

In the entrance region of the flow channel, the hydrodynamic, thermal, and concentration boundary layers are developing, and the transfer coefficients are considerably larger than those in the fully developed region. (Incropera & DeWitt 1996: 294–296) The enhancement in the transfer coefficient, i.e. in the Nusselt number for heat transfer and in the Sherwood number for the mass transfer, can be estimated using the following correlation developed for circular tubes (Molki & Sparrow 1986)

$$\frac{Nu_{average}}{Nu_{fully\ developed}} = 1 + \frac{a}{\left(\frac{X}{D_h}\right)^b}, \tag{43}$$

where X is the distance from the inlet of the channel, D_h is the hydraulic diameter, and a and b are defined as

$$a = 23.99 \cdot Re^{-0.230}, \text{ and} \tag{44}$$

$$b = -2.08 \cdot 10^{-6} \cdot Re + 0.815. \quad (45)$$

Due to the analogy between heat and mass transfer, the increase in the Nusselt number is the same as the increase in the Sherwood number (Incropera & DeWitt 1996).

2.4 CFD modeling

In Computational Fluid Dynamics (CFD), the systems involving fluid flow, heat transfer or other associated phenomena are analyzed by computer based simulations. CFD can be applied in a wide range of applications in environmental, chemical, aerospace, electrical, biomedical and marine engineering, just to mention a few. (Versteeg & Malalasekera 1995: 1) CFD provides the ability to determine the velocity, temperature and concentration data for a wide range of fluid and material properties, operating conditions and geometric characteristics of the heat exchanger. The obtained data can be reported at any position and time during the simulation without any disturbance to the underlying flow as exists in experimental measurements.

In order to use CFD, the computational domain, i.e. the model geometry, needs to be divided into cells that form a computation grid. The cells of the grid may have different sizes or shapes (e.g., quadrilateral or triangular in 2D, or tetrahedral, hexahedral or prism in 3D). The governing equations representing the system are solved in the computational nodal point in the middle of each cell, and therefore, the amount of cells affects directly on the computation time. On the other hand, the density of the grid needs to be fine enough to capture all of the necessary phenomena. Therefore, the optimization between computation time and accuracy of the results may be needed. (Anderson 1995: 198–171, Shaw 1992: 88–96)

2.4.1 Modeling a flow system

CFD uses the equations derived from the conservation laws, presented in Section 2.3, to describe the flow system and the associated phenomena. In addition to the conservation laws, other relations (such as the Fourier's law presented in Section 2.3.2.) are needed to define the unknown variables. The equations derived from

the conservation laws are, in practice, suitable for simple systems with laminar flow conditions. This approach is called the Direct Numerical Simulation (DNS).

Fluid flows in nature or in industrial processes are often turbulent. Turbulence is the random, chaotic movement of fluid. There is no strict limit between laminar and turbulent flows, but transition to swirly and three-dimensional turbulence begins from hydrodynamic instabilities in laminar flow, which are caused by viscous and inertia effects. For example, for a pipe flow, the transition between laminar and turbulent flows takes place at $2000 < Re < 10^4$ (Welty 1974: 183). Turbulent flow has good diffusion abilities, which improves mixing and increases momentum, heat and mass transfer, compared to laminar flow. (Versteeg & Malalasekera 1995: 41–47)

Variables in the turbulent flow (e.g., velocity, pressure, temperature, and concentration) are unsteady and random both in time and space. Therefore, turbulent flow has a wide range of length and time scales, which means that modeling of turbulent flow with DNS would require a very fine grid. Since the values of the variables are calculated at every nodal point of the computation grid, the amount of data would be enormous especially for large geometries, which restricts the applicability of DNS to small geometries and low flow velocities. (Versteeg & Malalasekera 1995: 41–47)

Despite the time-dependent and spatially three-dimensional characteristics, turbulent flows are usually statistically independent of time, and therefore, statistical methods have been developed for turbulence modeling. Turbulence models can be divided into the Reynolds-averaged Navier-Stokes (RANS) and LES (Large Eddy Simulation) models. Also, combinations of RANS and LES appear. In the LES models, the large scale movement is calculated directly, and only the small scale movement is modeled. In the RANS models, the RANS equations have the same general form as the instantaneous Navier-Stokes equations (Eqs. 24 and 25), but the solution variables represent the averaged values. In addition, the RANS equations have additional terms (Reynolds stresses) representing the effects of turbulence, which needs to be modeled in order to solve the RANS equations. For this purpose, several options, such as different forms of the k-ε and k-ω turbulence models, are available. (Versteeg & Malalasekera 1995: 49–54) In this thesis, the standard and the RNG k-ε turbulence models are used, and therefore introduced in more detail.

The standard k-ε turbulence model is a widely used model for fully turbulent flows. In the standard k-ε turbulence model, two separate transport equations, one for the turbulence kinetic energy, k (Eq. 46), and one for the dissipation rate, ε (Eq.

47) are solved allowing the determination of the turbulent length and time scales. Turbulent viscosity, μ_t, (Eq. 48) is calculated by combining the kinetic energy and the dissipation rate. (ANSYS Inc. 2011a, Launder & Spalding 1972)

$$\frac{\partial}{\partial t}(\rho k) + \nabla \cdot (\rho k \vec{v}) = \nabla \cdot \left[\left(\mu + \frac{\mu_t}{\sigma_k}\right) \nabla k\right] + G_k + G_b - \rho\varepsilon - Y_M + S_k, \quad (46)$$

$$\frac{\partial}{\partial t}(\rho \varepsilon) + \nabla \cdot (\rho \varepsilon \vec{v}) = \nabla \cdot \left[\left(\mu + \frac{\mu_t}{\sigma_\varepsilon}\right) \nabla \varepsilon\right] + C_{1\varepsilon} \frac{\varepsilon}{k}(G_k + C_{3\varepsilon} G_b) - C_{2\varepsilon} \rho \frac{\varepsilon^2}{k} + S_\varepsilon, \quad (47)$$

$$\mu_t = \rho C_\mu \frac{k^2}{\varepsilon}. \quad (48)$$

In Eqs. 46–47 G_k is the generation of the turbulence kinetic energy due to the mean velocity gradients and G_b due to buoyancy. Y_m is the contribution of the fluctuating dilatation in compressible turbulence to the overall dissipation rate, and σ_k and σ_ε are the turbulent Prandtl numbers for k and ε, respectively. $C_{1\varepsilon}$, $C_{2\varepsilon}$, $C_{3\varepsilon}$ are constants, which have the default values of 1.44, 1.92, 0.09, respectively. (ANSYS Inc. 2011a)

The RNG k-ε turbulence model is based on a renormalization theory, which is a statistical technique providing an analytically derived formula for the effective viscosity. Due to this differential viscosity model, the RNG k-ε turbulence model may be suitable also for lower Reynolds numbers. The constant of the RNG k-ε turbulence model differs from that of the standard k-ε turbulence model, and the transport equation for the dissipation rate contains an additional term that makes the RNG k-ε turbulence model more responsive to the effects of rapid strain and streamline curvature than the standard k-ε turbulence model. (ANSYS Inc. 2011a)

2.4.2 Boundary conditions

Boundary conditions define the variables of the system on the boundaries of the physical model. The choice of appropriate boundary conditions is very important since the boundary conditions dictate the solutions obtained from the governing equations. (Anderson 1995: 80)

Plenty of options are available for different boundary types and their conditions. Boundary types are e.g., flow inlet and outlet boundaries, walls, repeating and pole boundaries, and internal face boundaries. (ANSYS Inc. 2011b:

211) Some of the most common boundary conditions of these boundary types are introduced below.

At the inlet boundaries it is common to define the velocity or pressure and other scalar properties. For compressible flows, the mass flow rate may be defined at the inlet. Other possible inlet boundary conditions are e.g., the inlet vent and the intake fan in which the loss coefficient and pressure jump, respectively, are defined in addition to flow direction, total pressure and temperature. At the outlet, the static pressure (along with other scalar variables in case of back flow conditions) is often used as the boundary conditions. An option for a fully developed outlet boundary is the outflow condition where all of the stream wise gradients, except the pressure, are assumed to be zero. In addition, the outlet vent or the exhaust fan boundary conditions, in which the loss coefficient or the pressure jump, respectively, are defined with the pressure and the temperature, may be used. (ANSYS Inc. 2011b: 261–262)

At the walls, the required specifications depend largely on the selected models. For example, wall motion conditions, shear conditions, wall roughness, or thermal, species, chemical reaction, discrete phase, wall adhesion, and contact angle conditions may be defined. (ANSYS Inc. 2011a: 313)

The symmetry boundary condition is utilized when the solution is expected to have mirror symmetry. At the symmetry boundary, the convective and diffusion fluxes across the boundary are zero, i.e. velocity and gradients of all variables are zero normal to the symmetry plane. (ANSYS Inc. 2011a: 334–336)

2.4.3 Solution methods for CFD

CFD programs solve algebraic conservation equations that are obtained from the partial differential governing equations using a certain discretization method. The most common discretization methods are finite element, finite volume and finite difference methods. ANSYS FLUENT, which is used in this thesis, uses the finite volume method (FVM).

In the finite volume method, the computation domain is divided into discrete control volumes using a computational grid. The governing equations representing the system are integrated over the control volume to get discretized equations at the nodal point located at the cell's center. The discrete equations therefore express the conservation law on a control volume basis. (Versteeg & Malalasekera 1995: 85–88)

The discretized transport equations need to be linearized in order to solve them. Two different methods for linearization and the solution of the linear equation system are available in ANSYS FLUENT; pressure-based and density-based methods. In the pressure-based method, an iterative protection method is used to solve the pressure equation, which is derived from the momentum and the continuity equations in such a way that the continuity is satisfied by the velocity field, which is corrected by the pressure. The algorithms available for the pressure-velocity coupling are e.g., SIMPLE, SIMPLEC, PISO, and Coupled (ANSYS Inc. 2011a: 666–671). The pressure-based solver has traditionally been used for incompressible flows as in this thesis. (ANSYS Inc. 2011a: 641–647)

The discrete values of the scalars are stored at the cell centers. In order to solve the convection terms in the discretized equations, the values of the scalar variables are needed on the faces of the control volumes. (Versteeg & Malalasekera 1995: 87) To interpolate the face values from the nodal values, the upwind schemes, such as first-order, second-order or quadratic (QUICK) upwind, or power-law can be used. For interpolation of the pressure e.g., standard, linear, second order or PRESTO! schemes are available. Also, the gradients of the variables are needed in the discretization of the convection and diffusion terms in the flow conservation equations. Methods available for this are e.g., Green-Gauss Cell-Based, Green-Gauss Node-Based, and Least Squares Cell-Based. In addition to spatial discretization, temporal discretization is needed for transient simulations. The choice of the interpolation technique usually depends on the modeled system, but also on the computational capacity available and the required accuracy of the solution. The first order upwind interpolation technique may be acceptable for simple flow processes in which the flow is aligned with the computation grid. If the flow is not aligned with the grid, the numerical discretization error may increase with the first-order upwind scheme. The second order upwind is more suitable for complex flows and yields more accurate results. However, convergence problems may occur with the second order upwind technique, but they can be overcome by using the first order upwind at the beginning of the simulation. In this thesis, both the first and second order upwind techniques were applied for the face value interpolation, and Green-Gauss Cell-Based for the gradient interpolation. (ANSYS Inc. 2011a: 648–673)

3 Materials and methods

3.1 Experimental methods

Fouling experiments are conducted in a laboratory to study the crystallization fouling of $CaCO_3$ on a heated surface in well-controlled conditions. In the fouling experiments, an idealized heat exchanger is used as a test section. The test surfaces of the test section are heated, which increases the supersaturation of the test fluid near the surface, and therefore provides a platform to study the surface crystallization fouling of $CaCO_3$. The formation of the fouling layer on the surface can be detected from the measured wall temperature, T_w, which increases with time due to the growth of the resistive fouling layer on the surface. In the experiments, the effects of flow velocity, heat flux, concentration and surface patterning on the crystallization fouling of $CaCO_3$ are studied. The following sections provide more information about the experiments.

3.1.1 Fouling test apparatus

The fouling experiments presented in this thesis were performed in a laboratory scale set-up that has an idealized test section of a plate heat exchanger and controlled operating conditions. A schematic of the experimental set-up is presented in Fig. 7.

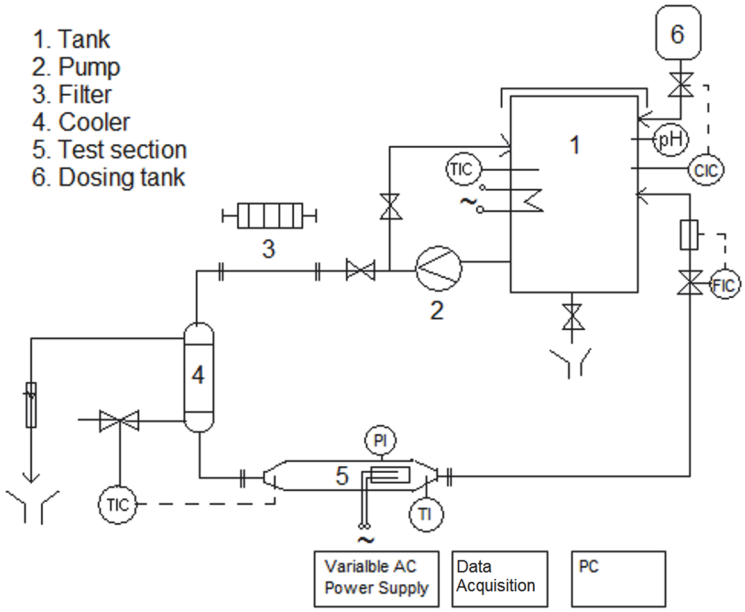

Fig. 7. Schematic of the experimental set-up (Riihimäki *et al.* 2009) (Paper I, published by permission of Elsevier).

The set-up has a closed flow loop in which the test fluid is pumped from a 100 l mixing tank (label 5 in Fig. 7), through filters (two Watman washable 60 µm nylon filters and two Watman polypropene 1 µm filters) (label 3 in Fig. 7) and a double pipe heat exchanger (label 4 in Fig. 7), to the (vertical) test section (label 5 in Fig. 7), where the flow goes downwards, and back to the mixing tank. The test fluid is heated in the tank to a desired bulk temperature. The double pipe heat exchanger is used to accurately control the inlet temperature of the fluid entering into the test section. The temperatures of the inlet and outlet fluids and the test surfaces are measured with SKS Automaatio Oy K-type thermocouples. The flow rate is measured with a Bürkert 8045 Electromagnetic Flow Transmitter and controlled with a control valve (Bürkert 2632).

The conductivity of the test solution is maintained constant by adding a conductivity control solution, made of $CaCl_2 \cdot 2H_2O$ (1.5 g/l) and $NaHCO_3$ (1.5 g/l) salts mixed with deionized water, automatically to the mixing tank during the experiment. The conductivity is measured (Bürkert 8225) and controlled with a magnetic on-off valve (Bürkert 0124). The purpose of the

conductivity control is to replace ions removed from the test solution due to crystallization fouling and therefore maintain the concentration of the solution approximately constant during the experiment.

LabView 8.0 software is used as the control and data acquisition system. The system is built on National Instruments Inc. components on a compact Field point 2100 platform.

3.1.2 The test sections

The experimental set-up has a vertical test section where the fouling takes place. The test section can be removed from the set-up for cleaning or replacement. Two different test sections have been used in this thesis. The steel block test section was used in Papers I, II, and III, and a steel plate on a copper block test section in Paper IV.

Steel block

The steel block test section (Fig. 8) is made of two stainless steel (AISI 316L) blocks (0.2 m long x 0.1 m wide x 0.02 m thick) that form a rectangular flow channel with two flat test surfaces between them. The steel blocks are heated with electrical heaters (Watlow Firerod, 230V/1000W) that are embedded in the walls of the steel blocks and connected to a power transmitter (TEKLAB ACP 100) that provides a constant but adjustable heat flux to both test surfaces. The test surfaces are therefore hotter than the test fluid, and provide sufficient supersaturation for crystallization at the surface. The same steel blocks are used in all experiments in order to ensure that the surface conditions are identical in every test. The steel blocks are washed after every test by rinsing them with de-ionized water and brushing the test surfaces gently with a soft sponge.

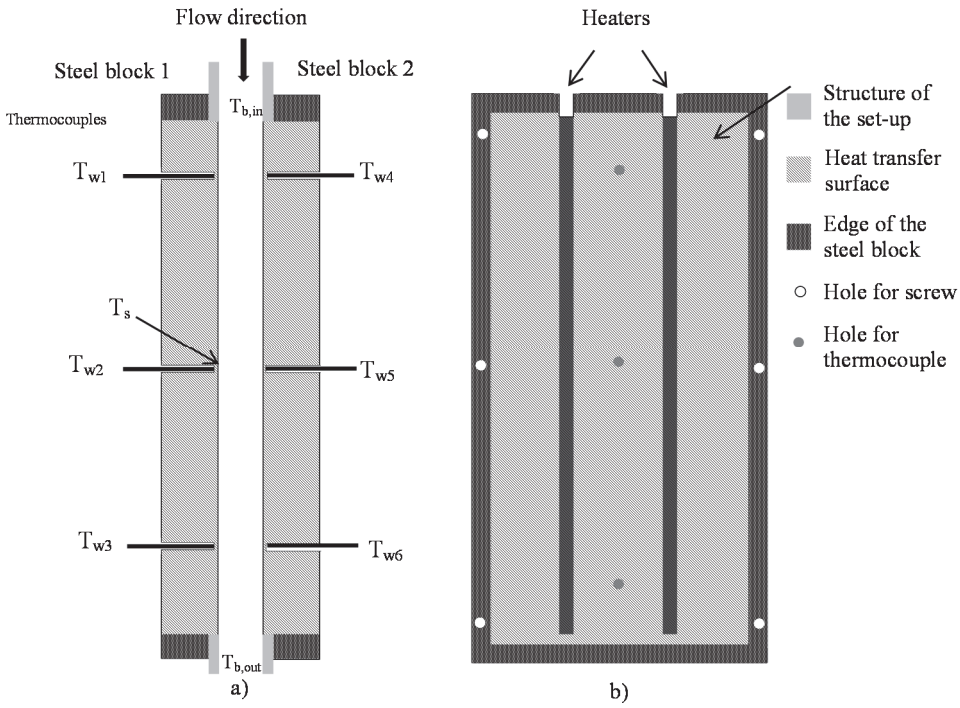

Fig. 8. Schematic of the steel block test section: a) side view of the steel blocks with the thermocouples, and b) front view of the used steel block with heaters and positions of the thermocouples (Paper II, published by permission of Elsevier).

The wall temperature (T_w) is measured by three thermocouples placed in the holes drilled through the steel block, as shown in Fig. 8. Because steel has a relatively low thermal conductivity, slight variations in the wall temperatures were detected. The measured wall temperature also deviates slightly from the surface temperature (T_s) (i.e. the temperature at the interface between the heated surface and the fluid), in which the fouling takes place, because the thermocouples do not exactly reach the surface. A 3D CFD model (Paper II), which includes both the steel block and the flow channel, was used to determine the variations in the surface temperature. The CFD model showed that the temperature measurement point in the middle of the test section corresponded quite well (within ± 2%) to the average wall temperature. Therefore, the measurement point in the middle of the test section is used to represent the average surface temperature.

The flow channel gap at the inlet of the test section is 0.015 m and hydraulic diameter (D_h) is 0.026 m. The flow at the entrance of the test section is fully developed because a 0.54 m (20 D_h) long and straight flow channel precedes the test section. However, there is about 0.002 m enlargement in both sides of the flow channel due to sealing of the steel blocks and placement of the steel block to the test section, which increases the hydraulic diameter to 0.03, and causes some instability to the flow regime and leads to a hydrodynamically developing flow. Because there is no preheated section before the test section, the mass and heat transfer boundary layers are developing throughout the test section.

Steel plate on copper block

Some experiments were conducted with a test section that contains a flat steel plate (thickness 0.0008 m) which is heated with electronic heaters embedded in a copper block (thickness 0.025 m). Good connection between the steel test plate and copper block heater is ensured by a thermal conductivity paste (λ = 0.9 W/m·K) between them.

With the steel plate on copper block test section, the surface temperature and the heat flux are more uniform than with the steel block test section. However, a consistent connection between the steel test plate and the copper heating block in every test is a challenge with this arrangement. In addition, the gap in the flow channel on the test surface increases to about 0.023 m (D_h = 0.37) with this test section.

The advantage of the steel plate on copper block test section is that the plate can be easily changed after every experiment and different surface properties (e.g., patterns, roughness, coatings) can be studied. In this thesis, the steel plate test section is used to study the effect of the surface patterning on crystallization fouling (Paper V). The studied surface patterns are presented in Fig. 9. The patterned surfaces, and the flat plate surface used in comparison with the patterned surfaces, were made of stainless steel AISI 304L 2B and had a thickness of 0.8 mm.

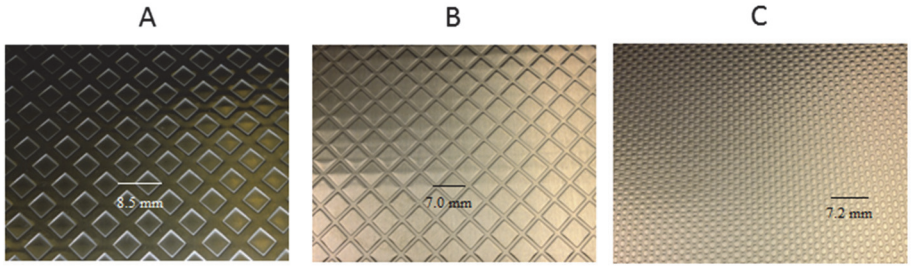

Fig. 9. Surface patterns used in the fouling experiments (Paper IV, published by permission of TTP).

3.1.3 The test solution

The fouling tests were performed using $CaCO_3$ as a fouling compound. A test solution was prepared by mixing 50 g of $CaCl_2 \cdot 2H_2O$ (BDH Prolabo) and 50 g $NaHCO_3$ (BDH Prolabo) salts into 100 dm^3 of pre-heated deionized water.

A thermodynamic equilibrium analysis, performed by the MINEQL+ 4.5 software, was performed to determine the bulk and saturation concentrations of the solution (Paper II). According to the analysis, the solution mainly consists of Ca^{2+} and HCO_3^- ions (Fig. 10), which is consistent with the literature (Bott 1995, Stumm & Morgan 2012).

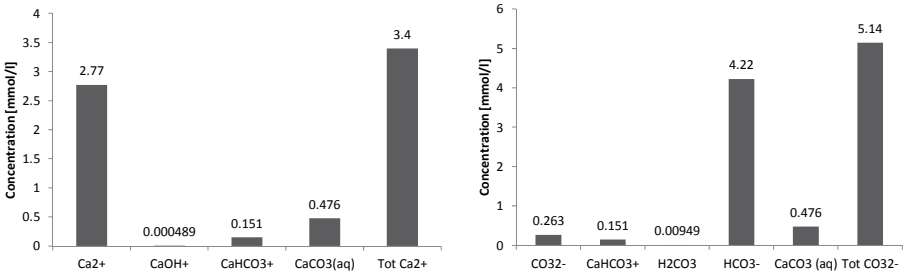

Fig. 10. a) Calcium and b) carbonate speciation in the solution used in the experiments (Paper II, published by permission of Elsevier).

According to analysis (Paper II), the bulk concentration of the solution (C_b) (corresponding to the inlet concentration), when all the aqueous species of

calcium and carbonate ions in the solution are taken into account, is 4.18 mmol/l. Because the bulk temperature, 30 °C, remains constant in all experiments, the bulk concentration can be assumed to be constant. In the concentration variation experiments, the amounts of salts were varied (30 g, 50 g, or 70 g of both $CaCl_2 \cdot 2H_2O$ and $NaHCO_3$ salts). The bulk concentrations in those tests were 2.57 mmol/l, 4.18 mmol/l, and 5.78 mmol/l, respectively.

The saturation concentration (C_{sat}) is affected by the pH, temperature, and the chemical composition of the solution. In this thesis, the saturation concentration is calculated from the ion product of the aqueous calcium and carbonate ions in the equilibrium (Paper II). The solid phase is assumed to be calcite in the thermodynamic analysis because it has the lowest solubility of the polymorphs of calcium carbonate. In addition, the X-ray diffraction studies of Pääkkönen *et al.* (2009) showed that the obtained fouling layer consists mainly of calcite. Fig. 11 shows the temperature dependency of the saturation concentration. The temperature dependent saturation concentration used in the fouling models is obtained using the curve fit to Fig. 11. The supersaturation degree corresponds to those presented e.g., by Mayer et al (2013).

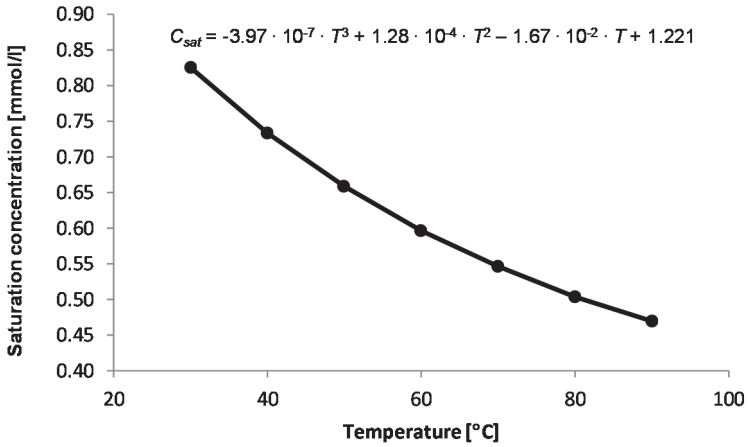

Fig. 11. Saturation concentration of $CaCO_3$ in the test system as a function of temperature according to MINEQL+ 4.5 (modified from Paper II, published by permission of Elsevier).

3.1.4 Experimental procedure for the fouling tests

The following procedure was followed in every test in order to ensure that different tests can be compared. First, the mixing tank is filled with deionized water. Deionized water is circulated in the set-up having the tank and the test section heaters on to heat the fluid to the desired temperature. As the target temperature is achieved, the test section heaters are turned off and the fluid is circulated only in the mixing tank. Two buckets with a volume of 8 dm^3 each are filled with preheated de-ionized water, and 50 g of both $CaCl_2 \cdot 2H_2O$ and $NaHCO_3$ salts are dissolved separately in these buckets. These concentrated salt solutions are added slowly, one after another to the mixing tank. After that, the test fluid is circulated within the whole set-up until the conductivity of the solution is settled denoting the full mixing of the salts in the test fluid. After the test solution is fully mixed, the test section heaters are turned on. The test begins when the inlet and test section's wall temperatures stabilize.

In the crystallization fouling experiments, the effects of flow velocity, heat flux (wall temperature), concentration and surface patterning on the fouling behavior are studied. The used operating conditions are presented in Table 1.

Table 1. The operating conditions used in the experiments in this thesis.

Parameter	Range
q	49.3–62.5 kW/m^2
T_w	69.0–91.5 °C
T_b	30 °C
v_{in}	0.2–0.4 m/s
C_b	2.57–5.76 mmol/l

3.2 Data analysis

The following sections provide information about calculating the fouling resistance and the mass deposition rate based on the wall temperature measurements. In addition, the ex-situ measurements to define the properties of the fouling layer are introduced.

3.2.1 Fouling resistance

The measured wall temperature, T_w increases due to the growth of the resistive fouling layer on the surface because the heating system produces a constant heat flux, q, to the test section. The fouling resistance, R_f, is used to quantify the thermal performance of heat exchangers during fouling. It can be calculated from the change in the measured wall temperature (Krause 1993, Mwaba *et al.* 2006b, Pääkkönen *et al.* 2012)

$$R_f = R_{f,t} - R_{\mathrm{f},0} = \left(\frac{(T_w - T_b)}{q}\right)_t - \left(\frac{(T_w - T_b)}{q}\right)_0 = \frac{T_w^t - T_b^t - T_w^0 + T_b^0}{q}, \quad (49)$$

where *t* and *0* denote time and initial, respectively.

The heat flux may be considered to remain constant during an experiment because the experimental data shows that the bulk temperature of the fluid leaving the test section remains constant during an experiment. In addition, calculation of the energy balance shows that the difference between the total energy flow into and out of the test section is less than ± 3% when normalized by the energy flow into the test section, which is less than the uncertainty in the energy imbalance. (Paper I) Therefore, heat loss to the environment is negligible. Because the heat flux and bulk fluid temperature remain constant during an experiment, the bulk temperature cancels out from Eq. 49, and the fouling resistance can be calculated from

$$R_f = \frac{T_w^t - T_w^0}{q} = \frac{\Delta T}{q}. \quad (50)$$

3.2.2 Fouling rate

The rate of change of the fouling resistance with time is known as the fouling rate and is calculated with

$$\frac{dR_f}{dt} = \frac{dT_w(t)}{q \cdot dt}. \quad (51)$$

The temperature difference in Eq. (51) is between the initial and final wall temperatures, and the time difference is the length of the experiment.

3.2.3 Mass deposition rate

The mass deposition rate is needed to validate the fouling models that predict the mass flux to the surface instead of the thermal resistance of the fouling layer. The mass deposition rate, m_d, at a certain time can be calculated using the density and the thickness of the fouling layer as follows

$$m_d = \frac{\rho_{fl} dx_{fl}(t)}{dt}, \tag{52}$$

where ρ_{fl} is the density of the fouling layer and dx_{fl} is the change in the thickness of the fouling layer. The change in the thickness and in the area based fouling resistance are related by

$$dR_f = \frac{dx_{fl}}{\lambda_{fl}}, \tag{53}$$

where λ_{fl} is the thermal conductivity of the fouling layer. Solving dx_{fl} from Eq. 53, and substituting it with Eq. 51 to Eq. 52 gives the mass deposition rate

$$m_d = \frac{dR_f \rho_{fl} \lambda_{fl}}{dt} = \frac{dT_w(t) \rho_{fl} \lambda_{fl}}{q \cdot dt}. \tag{54}$$

Therefore, the thermal conductivity and density of the fouling layer are needed in order to calculate the mass deposition rate from the experimental data. To estimate these parameters, the porosity of the fouling layer, ε, is needed.

The porosity of the fouling layer can be related to the density of the fouling layer using the parallel method (Fauchoux *et al.* 2010, Helalizadeh *et al.* 2005, Olutimayin & Simonson 2005)

$$\rho_{fl} = \varepsilon \cdot \rho_{air} + (1 - \varepsilon) \cdot \rho_{CaCO_3}. \tag{55}$$

Therefore, the porosity can be defined using the density of the air-filled fouling layer from

$$\varepsilon = \frac{\rho_{fl} - \rho_{CaCO_3}}{\rho_{air} - \rho_{CaCO_3}} = \frac{\rho_{fl}}{\rho_{air} - \rho_{CaCO_3}} - \frac{\rho_{CaCO_3}}{\rho_{air} - \rho_{CaCO_3}}. \tag{56}$$

The density of the air-filled fouling layer is measured after certain fouling experiments by removing the test sections from the facility. To determine the density of the air-filled fouling layer, ρ_{fl}, using Eq. 57, the thickness of the fouling layer, x, and the mass of the deposited material, m, on a certain area, A, are needed

$$\rho_{fl} = \frac{m}{A \cdot x}. \tag{57}$$

The thickness of the fouling layer is determined using a light microscope. The change in the focal point of the microscope between the clean steel surface and the fouling layer is determined to get the thickness of the fouling layer. The accuracy of the thickness measurement is improved by taking thickness as an average value from five different measurements over the heat transfer area. The mass of the fouling layer is determined by scraping the fouling layer from the surface of the test section, from a certain area. The mass is determined with a digital scale and the area is measured with a digital caliper.

As the porosity is obtained, the density (Eq. 58) and the thermal conductivity (Eq. 59) of the liquid filled fouling layer can be calculated using the parallel method

$$\rho_{fl} = \varepsilon \cdot \rho_f + (1 - \varepsilon) \cdot \rho_{CaCO_3}, \tag{58}$$

$$\lambda_{fl} = \varepsilon \cdot \lambda_f + (1 - \varepsilon) \cdot \lambda_{CaCO_3}. \tag{59}$$

3.3 Experimental uncertainty

An uncertainty analysis is necessary in any experiment to quantify the uncertainty in the measured and calculated data (Coleman & Steele 1999, Izadi *et al.* 2011). The uncertainty analysis is important especially if the measured fouling resistances are small. In this thesis, the uncertainties in the fouling resistance, fouling rate, properties of the fouling layer, and the mass deposition rate are defined using the following standard method (ASME 1985).

The sensor calibration and systematic errors that tend to remain constant throughout the experiments are called bias uncertainties (B). The precision uncertainties (P) come from random fluctuations during the experiments, and may be defined by statistical methods. To calculate the total uncertainty (U_{tot}), the bias and precision uncertainties are related as follows

$$U_{tot} = \sqrt{(B)^2 + (P)^2}. \tag{60}$$

In general, the bias uncertainty of the calculated parameter

$$\mathrm{r} = \mathrm{r}(x_1, x_2, \ldots x_n) \tag{61}$$

is obtained by

$$B_r = \sqrt{\sum_{i=1}^{n} (\theta_i B_{\overline{x_i}})^2}, \tag{62}$$

where the sensitivity coefficient is

$$\theta_i = \frac{\partial r}{\partial x_i}. \tag{63}$$

The bias uncertainties of parameters (Papers I and II) used in this thesis are presented in Table 2 for the calculation of the fouling resistance from the experimental data (Section 3.2.1), determination of the density of the fouling layer based on the ex-situ measurements of the fouling layer (Section 3.2.3), and the calculation of the mass deposition rate (Section 3.2.3).

The precision uncertainties may be quantified by linear regression and the standard error of estimate (SEE). The precision uncertainty is multiplied by the Student t value to get the 95% confidence level (Coleman & Steele 1999). The standard error of estimate (SEE) only applies to a linear curve because the method gives the standard deviation to the linear fit. In this thesis, the SEE was used to determine the precision uncertainty in the fouling resistance. The precision uncertainties in the density measurements and in the determination of the porosity of the fouling layer were defined from the standard deviation of the measurements, multiplied by the Student t value (Coleman & Steele 1999) to get the precision uncertainty at the 95% confidence level.

Table 2. Bias uncertainties of the measurements and properties of the fouling layer used in this thesis (Papers I and II).

Parameter	Unit	Value/range	Bias uncertainty
Fouling resistance			
q	[kW/m^2]	49.3–62.5 kW/m^2	± 2.5%
T	[°C]	69.0–91.5 °C	± 0.4%
Density			
m	[g]	Measured (Paper II)	± 10%
A	[m^2]	Measured (Paper II)	± 5%
x	[m]	Measured (Paper II)	± 20%
Mass deposition rate			
ρ_{CaCO_3}	[kg/m^3]	2870 kg/m^3	± 100 kg/m^3
ρ_{air}	[kg/m^3]	1.2183 kg/m^3	± 0.02 kg/m^3
ρ_f	[kg/m^3]	971 kg/m^3	± 0.13 kg/m^3
λ_{CaCO_3}	[W/(mK)]	5.09 W/(mK)	± 0.44 W/(mK)
λ_f	[W/(mK)]	0.66 W/(mK)	± 0.011 W/(mK)
t	[s]	Varies	± 0.1%

3.4 CFD modeling

CFD modeling is used to study hydrodynamic and thermal behavior, as well as crystallization fouling in the computational geometries corresponding to the experimental test sections. The following sections introduce the details of the model geometries and the model settings.

3.4.1 Model geometries

The model geometries and computational grids used in this thesis are created using the Gambit 2.6.4 program. The geometries represent the experimental test section with flat (Fig. 12) and patterned (Fig. 13) surfaces. 2D models are chosen to represent the flow conditions in the middle of the test section.

Flat plate geometry of the test set-up

The flat surface geometry presented in Fig. 12 is meshed with quadrilateral cells. The grid of the flow channel is generated such that the cell height gradually reduces towards the wall. The grid independency tests in Paper III show that a cell height of 5 μm next to the wall provides an appropriate compromise between the accuracy of the results and the computation time.

The width of the channel depends on whether the steel block (19 mm flow gap) or steel plate (23 mm flow gap) is used in the fouling test section. The geometry with 19 mm flow gap contains 76000 quadrilateral cells, whereas the geometry with 23 mm flow gap has 83600 quadrilateral cells.

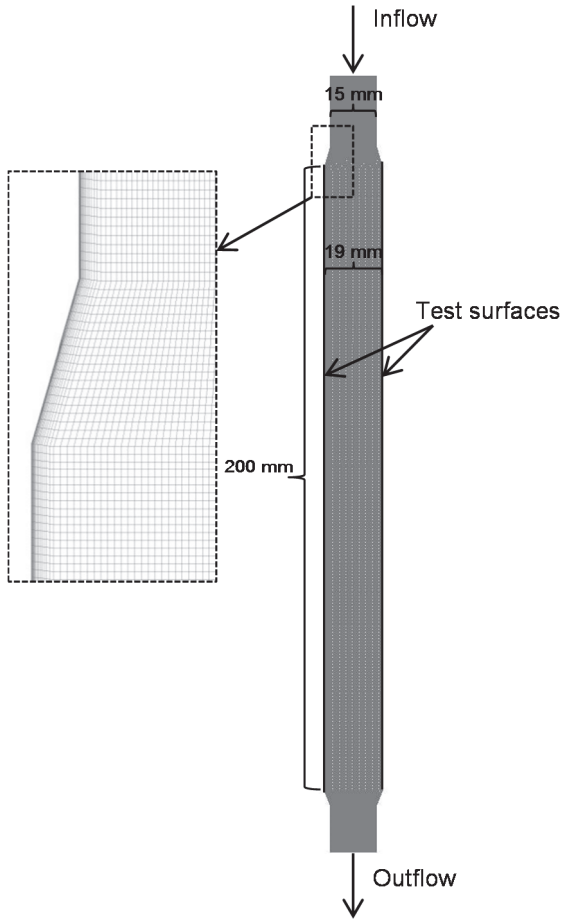

Fig. 12. Computation geometry and grid for the steel block test section (Paper III, published by permission of Elsevier).

Patterned geometry of the test set-up

The patterned surface geometry (Fig. 13) represents the pattern C presented in Section 3.1.2. The surface pattern C has curved patterns whose heights are 0.02 mm and 0.05 mm, lengths 0.5 mm and 1.4 mm, respectively, and a 0.1 mm gap between them. Because of the small dimensions of the geometry and requirement of the high grid density near the wall, an enormous number of cells would be

required for modeling the whole geometry corresponding to the experimental set-up. Therefore, only a 7 mm long and 5mm high portion of the geometry is used in the modeling of the patterned surface geometry. The patterned surface geometry has a grid with 326 300 triangular cells.

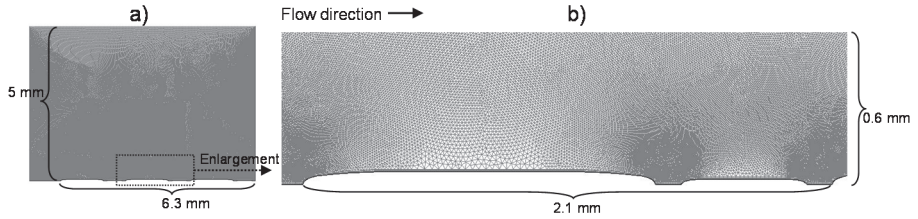

Fig. 13. The model geometry with a patterned surface (a), and enlargement of the near wall region (b) (Paper V, published by permission of TTP).

3.4.2 Model settings

CFD modeling in this thesis has been performed using the ANSYS FLUENT 13.0 and 14.0 CFD packages. The finite volume based discretization method is used with a pressure-based solver algorithm and finite-difference interpolation techniques to solve the governing equations for the conservation of mass, momentum, and energy. (ANSYS Inc. 2011b)

For turbulence modeling, both standard and RNG k-ε turbulence models with the Enhanced Wall Treatment are employed. The Enhanced Wall Treatment allows resolving the viscosity affected near wall region all the way to the viscous sublayer if the computation grid is fine enough, i.e., $y^+ \sim 1$, as is in this work. Detailed modeling of the near wall area is important because the phenomena taking place in the boundary layer affect significantly the mass deposition rate. The energy equation is enabled for heat transfer modeling and the species model for mass transfer modeling. (ANSYS Inc. 2011b) The crystallization fouling model (Section 4.2.4) is connected to the flow and species model as a sink term using the user defined functions of ANSYS FLUENT.

Steady-state simulations are used if only the fluid flow and the heat transfer are modeled in order to save computation time. When the fouling model is included, time-dependent simulations with the length corresponding to the experiments are used due to the time-dependent nature of fouling.

Boundary conditions are defined in each case to correspond to the experimental conditions, as shown in Table 3. Generally, at the inlet boundary, the flow velocity, temperature, and salt concentration are defined based on experimental conditions. At the outlet boundary, pressure is set to zero. The backflow conditions are approximated from the inlet conditions to the direction of normal to the outlet boundary. At the walls, the flow velocity and the diffusion flux of the species are set to zero. Thermal conditions are defined at the heated wall (usually the heat flux is defined, but in sensitivity studies, a constant surface temperature is employed), whereas other walls are insulated.

Table 3. The boundary conditions used in CFD (Paper III).

Boundary	Condition	Values
Inlet	$v_{in} = v_{in,exp}$	0.1 m/s–0.45 m/s
	$T_{in} = T_{in,exp}$	30 °C
	$C_b = C_{b,exp}$	0.259–0.578 kg/m^3
Outlet	$p = 0$	
Walls	$v = 0$	
	$\partial Y_i / \partial n = 0$	
	$\partial T / \partial n = 0$	
Heated wall	$q = q_{exp}$	49–62.5 kW/m^2

4 Results and discussion

4.1 Experiments for crystallization fouling

This section summarizes the results obtained from crystallization the fouling experiments on a flat steel surface. The experimental uncertainties and the effects of operating conditions on fouling resistance and fouling rate are presented. In addition, the experimental data are used to identify the governing sub-process of the crystallization fouling mechanism.

4.1.1 Fouling resistance in the crystallization fouling experiments on the flat surface (Paper I)

The surface crystallization fouling experiments presented in this section were carried out with the filters in-line of the set-up because, according to the bulk crystallization fouling experiments presented in Paper I, crystals in the bulk fluid significantly increase the fouling rate, and this effect can be avoided by filtering the test fluid.

The formation of the fouling layer on a heat transfer surface is detected from the change in the measured wall temperature, which is used to calculate the fouling resistance as described in Section 3.2.1 (Eq. 50). An example of the fouling resistance curve obtained in this thesis is presented in Fig. 14. The fouling layer resists heat transfer from the surface, which causes the wall temperature to increase. The first crystals deposited on a heat transfer surface, however, increase the surface roughness, which enhances the near wall turbulence and the convective heat and mass transfer. This is seen as a decrease in the wall temperature at the beginning of the experiment. As the wall temperature decreases, the apparent fouling resistance has negative values, as can be seen in Fig. 14 at the beginning of the experiment. This period is called the induction period. (Bansal & Müller-Steinhagen 1993, Helalizadeh *et al.* 2000, Mwaba *et al.* 2006a, Najibi *et al.* 1997a) The induction period ends when the fouling layer continues to grow on the surface and the heat transfer resistance caused by the fouling layer exceeds the effect of the enhanced heat transfer caused by the surface roughness.

The fouling resistance curve presented in Fig. 14 can be considered to increase approximately linearly after the induction period. During this linear

phase, the fouling conditions remain constant, which leads to a steady growth of the fouling layer on the surface. The experiments and modeling in this thesis mainly focus on this linear growth period. Most of the fouling tests are run around 6 hours, except in cases in which the surface temperature approaches the boiling point. In those cases, the tests are ended earlier in order to avoid boiling on the surface, which would affect the fouling rate because of the change in the fouling conditions. In addition, some experiments are run for around 24 h to ensure the continuation of the approximately linear increase in the fouling curve.

At some point, the fouling resistance may start to approach a constant value. The asymptotic, or even falling, fouling curve (the dashed lines in Fig. 14) could be due to 1) the removal of the deposits from the surface, 2) increased flow velocity caused by the narrowed flow channel, or 3) decreased temperature at the interface between the fouling layer and fluid. (Bansal *et al.* 2008, Mwaba *et al.* 2006a)

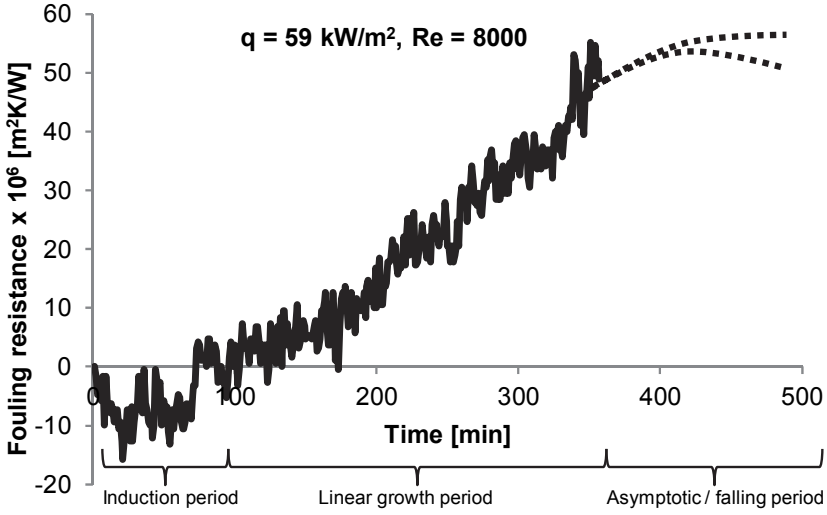

Fig. 14. Experimental fouling curve with different fouling periods.

The asymptotic fouling curve has not been detected in the experiments of this thesis. Reasons for this are: 1) Pure calcium carbonate depositions existing in this thesis form rather tenacious fouling layers that are hard to remove from the surface (Andritsos & Karabelas 2003, Lee *et al.* 2006). Therefore, the removal of crystals from the surface is unlikely. 2) The experiments presented here were rather short describing the initial stages of the fouling process when the crystals

are small and the fouling layer is thin. Therefore, the effect of the fouling layer to the cross-sectional area of the flow channel is minor. 3) The decrease in the interfacial temperature can be considered minor due to constant heat flux conditions as denoted in Hasson and Zahavi (1968). However, the formation of a rough fouling layer could increase the heat transfer coefficient and consequently decrease the interface temperature (T_i). This would lead to a decreased rate coefficient (k_r in Eq. 13) and a lowered driving force due to decreased saturation that both would reduce the surface integration of the ions. The decrease in the surface integration would be seen as an asymptotic fouling curve if the crystallization fouling process is controlled by the surface integration. However, the relative roughness of the studied fouling layers has been found to deviate from the smooth surface by less than 10% (Paper II). In addition, according to Mottahed and Molki (1996), the entrance region of the duct is significantly reduced by the surface roughness. This means that even if the heat (and mass) transfer increase due to increased roughness, the reduction in the entrance region due to roughness would decrease the heat and mass transfer. Therefore, constant heat and mass transfer coefficients, and further constant interfacial temperature may be assumed during the experiments.

Because the asymptotic behavior has not been detected in the experiments presented in this thesis, the assumption of the constant interfacial concentration is also justified in Section 4.2.

4.1.2 Experimental uncertainty in the fouling resistance (Paper I)

The bias uncertainty in the fouling resistance is calculated for each experiment by substituting Eq. (50) into Eq. (64)

$$B_{R_f} = \sqrt{\left[\left(\frac{\partial R_f}{\partial \Delta T} \cdot B_{\Delta T}\right)^2 + \left(\frac{\partial R_f}{\partial q} \cdot B_q\right)^2\right]}. \tag{64}$$

Taking the partial derivatives gives

$$B_{R_f} = \sqrt{\left[\left(\frac{1}{q} \cdot B_{\Delta T}\right)^2 + \left(-\frac{\Delta T}{q^2} \cdot B_q\right)^2\right]}. \tag{65}$$

The uncertainty analysis (Paper I) showed that the most of the bias uncertainty in the fouling resistance comes from the uncertainty in the temperature measurement. Therefore, the higher the temperature difference during the fouling experiments the lower the uncertainty. It was suggested that the

temperature difference of at least 2 °C will give reasonable (± 20%) bias uncertainty.

The precision uncertainties are defined using linear regression and the standard error of estimate (SEE) as shown in Fig. 15. The replicates are also included in the calculation of the precision uncertainty in order to include the repeatability to the analysis. The induction period is excluded from the calculation of the SEE due to its deviation from the linear fit required by the SEE.

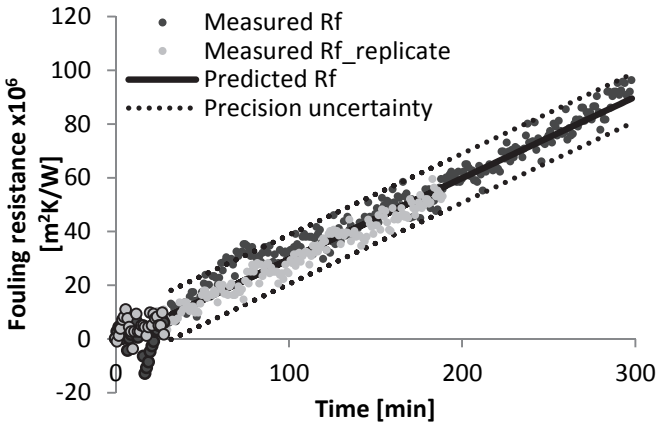

Fig. 15. Linear fit and 95% precision uncertainty bounds for the fouling resistance for the example case and its replicate. The induction is excluded from the curve fit and uncertainty analysis (Paper I, published by permission of Elsevier).

The total uncertainty in the fouling resistance at the 95% confidence level is then obtained as a square root of the sum of the squares of the precision and bias uncertainties

$$U_{R_f}^{tot} = \sqrt{[(B_{measurement})^2 + (2 \cdot SEE)^2\,]}. \quad (66)$$

The student t value of 2 is used to get the 95% confidence level for more than 30 measurements (Coleman & Steele 1999).

For the example case in Fig. 15, the uncertainty in the fouling resistance is $\pm\, 12.6 \cdot 10^{-6}$ m^{2}K/W, which is ± 13.5% at the end of the experiment. The uncertainty in the fouling resistance is $\pm\, 11.9 \cdot 10^{-6}$ m^{2}K/W (± 12.7% at the end of the experiment) if the replicate test is not included in the analysis. The small increase in the total uncertainty due to repeatability of the experiment shows that the tests are very repeatable.

4.1.3 *Effects of operating conditions on the surface crystallization fouling (Paper I)*

The surface crystallization fouling experiments were conducted for different heat fluxes and flow velocities given in Section 3.1.4 in Table 1 (Paper I). Examples of the fouling resistance curves are presented in Fig. 16 a) for varied heat fluxes, and b) for varied flow velocities.

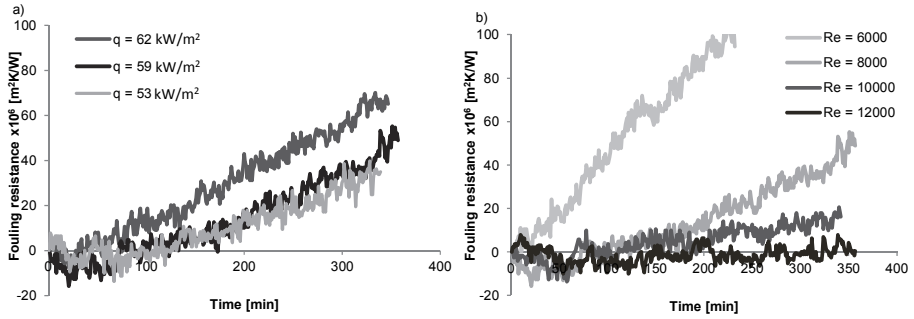

Fig. 16. Fouling resistance (a) with different heat fluxes when the Reynolds number is 8000, and (b) with different flow velocities when the heat flux is 59 kW/m^2 (modified from Paper I, published by permission of Elsevier).

The results in Fig. 16 (a) show that increasing the heat flux increases the linear growth rate of the fouling resistance. An increase in the heat flux increases the wall temperature that further increases both the supersaturation at the wall and the rate constant of the surface integration leading to higher fouling rate. Also, the mass transfer coefficient increases with temperature (Najibi *et al.* 1997a). Similar observations have been reported by many researchers (Hasson *et al.* 1968, Helalizadeh *et al.* 2000, Najibi *et al.* 1997a).

The role of the flow velocity is more complicated. When the flow velocity is increased, which is presented as an increasing Reynolds number in Fig. 16 (b), the convective heat and mass transfer increase due to increased turbulence. The enhanced mass transfer increases the diffusion of ions to the surface. On the other hand, the enhanced heat transfer lowers the surface temperature, which decreases the crystallization fouling rate via decreased supersaturation and rate constant (Eq. 14). In addition, an increasing Reynolds number results in an increased friction velocity in the solution-fouling layer interface, which reduces the probability of the attachment of the crystals to the surface due to a decreased

residence time of the fluid at the wall (Eq. 15). It is clear from Fig. 16 (b) that the temperature effect dominates fouling over the mass transfer effect in this work since an increase in the flow velocity decreases the linear growth rate of the fouling resistance. According to Najibi *et al.* (1997a), this is an indication of a surface integration controlled crystallization fouling process.

Fig. 16 also shows that the induction time depends on the operating conditions. The induction time decreases as the heat flux increases and as the Reynolds number decreases. At the low Reynolds numbers, the convective heat transfer is lower and therefore the surface temperature is higher. At the higher wall temperature, the crystallization fouling rate is higher due to the temperature effect on the rate constant for the surface integration in Eq. 14, and due to increased supersaturation at the surface. Because the crystallization fouling rate is high, the thickness of the fouling layer quickly reaches the limit where the advantage of the high heat transfer coefficient, caused by the first crystals on the surface, is overcome by the increased heat transfer resistance of the fouling layer. Therefore, the induction time is short in the conditions in which the crystallization fouling rate is high, i.e. with low Reynolds numbers and high heat fluxes. The temperature has an exponential effect on the surface integration of the crystallization fouling (Eq. 14). Therefore, at the lower wall temperature, i.e. with high Reynolds numbers and low heat fluxes, the crystallization fouling rate is much lower and the induction time is longer because it takes a longer time for the resistive fouling layer to overcome the effect of the enhanced turbulence even the laminar boundary layer is thinner with higher Reynolds numbers (Schlichting 1968). This can be observed in Fig. 16 as longer induction times with the higher Reynolds numbers are observed.

4.1.4 Governing sub-processes in crystallization fouling experiments (Paper I)

The crystallization fouling may be controlled by mass transfer, surface integration, or both (Bansal *et al.* 2008). The mass transfer mostly depends on the Reynolds number (flow velocity) and the surface integration mainly depends on the surface temperature. To define the controlling fouling mechanism in the experiments, the effect of flow velocity was differentiated from the effect of surface temperature. This was achieved by varying the flow velocity at constant initial wall and bulk temperatures (Helalizadeh *et al.* 2000). In order to keep the initial wall temperature constant, the flow velocity and heat flux were changed at

the same time. The fouling rate, calculated by Eq. 51, was used for the comparison of experiments. The fouling rates at constant initial wall temperature and various flow velocities are presented in Fig. 17.

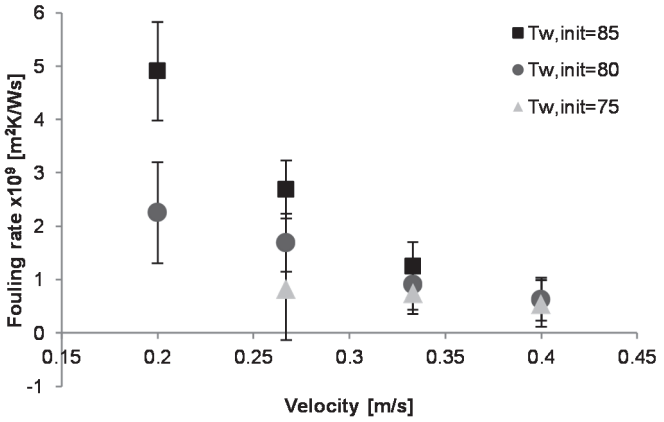

Fig. 17. Fouling rates on constant initial wall temperatures with varied flow velocity with their 95% uncertainty bounds (modified from Paper I, published by permission of Elsevier).

The results in Fig. 17 show that the flow velocity has a clear effect on the fouling rate especially at high wall temperatures. The experimental data shows that the fouling rate decreases when the flow velocity increases. This means that the mass transfer does not control the fouling process because, in mass transfer controlled conditions, the fouling rate would increase with an increasing flow velocity since the transport of ions to the surface increases with the velocity (Andritsos & Karabelas 2003, Fahiminia *et al.* 2007, Rose *et al.* 2000). Therefore, in this case the surface integration is controlling the fouling over the mass transfer. This finding corresponds with many studies on crystallization fouling in the literature (Augustin & Bohnet 1995, Bansal *et al.* 2008, Bansal & Müller-Steinhagen 1993, Mwaba *et al.* 2006a).

The decreasing fouling rate with an increasing flow velocity seen in Fig. 17 can be explained by the residence time of the fluid at the wall. As discussed in Section 2.2.4, an increase in the flow velocity decreases the residence time of the fluid at the wall, which reduces the probability of the crystals attaching to the surface (Epstein 1994, Fahiminia *et al.* 2007, Rose *et al.* 2000). According to Rose *et al.* (2000), mass transfer controls fouling at low flow velocities, which is

seen as an increasing fouling rate with an increasing flow velocity (see Fig. 6 in Section 2.2.4). At some flow velocity, a maximum in the fouling rate is achieved. After that point, the fouling rate begins to decrease as the flow velocity is increased indicating surface integration controlled conditions. In this thesis, the mass transfer controlled conditions and the maximum point in the fouling rate do not occur, but the experiments are in the surface integration controlled conditions, where the residence time of the fluid affects the results at higher flow velocities. However, the maximum fouling rates for each wall temperature and the mass transfer controlled area could most probably be seen if the flow velocity had been decreased further.

4.2 Modeling crystallization fouling

The following sections summarize work carried out for the development, validation and utilization of the crystallization fouling model in this thesis.

4.2.1 Definition of the properties of the fouling layer for the mass deposition (Paper II)

The crystallization fouling models predict the mass-based deposition rate on the surface. In order to calculate the experimental mass deposition rates from the measured fouling resistances, the properties of the fouling layer, i.e. thermal conductivity, density and porosity of the fouling layer, are needed (see Section 3.2.3).

The porosity was determined by the ex-situ measurements of the density of the fouling layer (see Section 3.2.3, Eq. 57). Using the methods described in Sections 3.2.3 and 3.3, the bias uncertainties of the density measurements presented in Section 3.3. (Table 2) and the precision uncertainty in the density measurements (determined from repeated tests), the average density of the air-filled fouling layer is calculated to be 196 ± 56 kg/m^3 ($= \pm 28\%$).

The porosity of the fouling layer is calculated from the densities of the air, $CaCO_3$, and the air filled fouling layer (see Section 3.2.3, Eq. 56). The bias uncertainty in the porosity is determined with Eq. 67 and the bias uncertainties presented in Section 3.3 (Table 2). The precision uncertainty in the porosity is determined from the repeated tests as described in Section 3.3. The average porosity of the fouling layer is 0.93 ± 0.02 ($= \pm 2.1\%$). Therefore, despite the relatively high uncertainty in the density, the uncertainty in the porosity of the

studied fouling layer is low. The obtained porosity value indicates that the surface is only partly covered by the crystals, and longer experiments would lead to an increase in the surface coverage and a decrease in the porosity, as was shown in Paper II. A corresponding finding on the surface coverage in the case of the $CaCO_3$ crystallization fouling was reported by Scholl & Augustin (2006).

$$B_\varepsilon = \sqrt{\left[\begin{array}{c}\left(\frac{1}{(\rho_{air}-\rho_{CaCO_3})}\cdot B_{\rho_f}\right)^2 + \left(\left(\frac{-\rho_{fl}}{(\rho_{air}-\rho_{CaCO_3})^2}+\frac{\rho_{CaCO_3}}{(\rho_{air}-\rho_{CaCO_3})^2}\right)\cdot B_{\rho_{air}}\right)^2 \\ + \left(\left(\frac{\rho_{fl}}{(\rho_{air}-\rho_{CaCO_3})^2}-\frac{\rho_{air}}{(\rho_{air}-\rho_{CaCO_3})^2}\right)\cdot B_{\rho_{CaCO_3}}\right)^2\end{array}\right]} \quad (67)$$

The density and the thermal conductivity of the liquid filled fouling layer were calculated from Eq. 58 and Eq. 59, respectively, using the determined porosity, and the properties of the fluid and $CaCO_3$ shown in Table 2 (Section 3.3). The density of the liquid-filled fouling layer is 1100 ± 44 kg/m^3 (= ± 4.0%) and the thermal conductivity 0.97 ± 0.10 W/(m·K) (= ± 10.6%), which corresponds to the values reported by Mayer *et al.* (2015) (0.87 W/(m·K)). The values are close to those of fluid because of the high porosity (i.e. large void fraction) of the fouling layer (Paper II).

The bias uncertainties (B) of the ex-situ measurements are generally high ($B_{\rho fl} = \pm 23\%$ in this case) because they are difficult to determine accurately. Therefore, the sensitivities of the bias uncertainties in the ex-situ measurements of the air-filled fouling layer on the calculated properties (ε, λ_{fl}, ρ_{fl}, m_d) are presented in Fig. 18. The sensitivity analysis in Fig. 18 shows that increasing the bias uncertainty of the ex-situ measurement up to 40% from the original value increases the uncertainty in the calculated properties by only 1.5%−5%. Therefore, the properties of the fouling layer (ε, λ_{fl}, ρ_{fl}, m_d) are not sensitive to the bias uncertainties of the ex-situ measurements when the porosity is high (0.93 in this case).

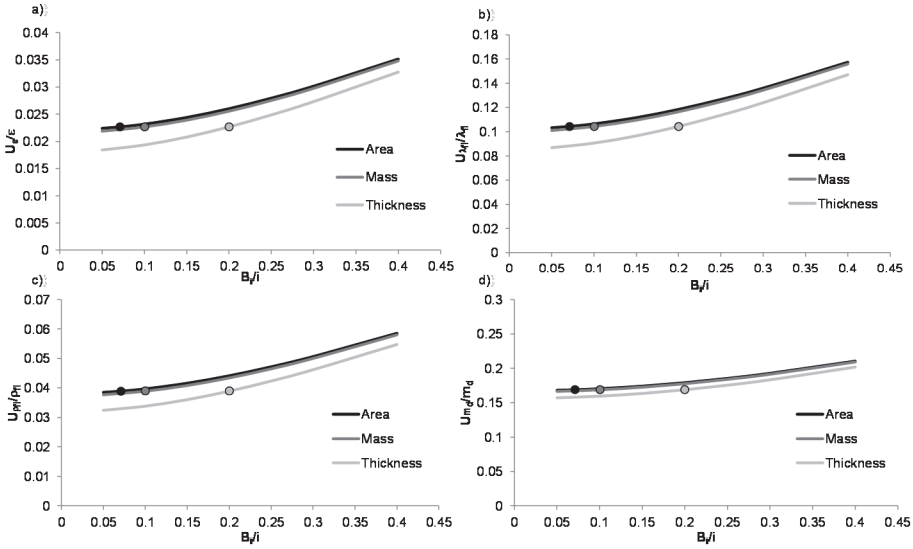

Fig. 18. Sensitivity of the bias uncertainties of the ex-situ measurements (area, mass and thickness) on the uncertainty of the (a) porosity, (b) thermal conductivity and (c) density of the fouling layer, and (d) the mass deposition rate (Paper II, published by permission of Elsevier).

Fig. 19 shows the bias uncertainty in the porosity for different porosities (the black line). The uncertainty is below 20% for the porosities over 0.55. As the porosity decreases, the bias uncertainty in the porosity increases. The uncertainty propagation equation (Eq. 67) shows that the uncertainty in the porosity comes mostly from the uncertainty in the density of the air-filled fouling layer. In Eq. 67, the uncertainty in the density is multiplied by the reciprocal of $(\rho_{air}-\rho_{CaCO3})$, which has quite a large value (negative sign disappears due to the second power in Eq. 67). This means that the uncertainty that comes from the density will have a rather low value when the density is low. Therefore, the uncertainty in the porosity is low for low densities and increases as the density decreases. Since the density of the fouling layer is low when the porosity is high, the uncertainty in the porosity will be low at high porosities.

The gray line in Fig. 19 demonstrates that the uncertainty in the mass deposition rate increases as the uncertainty in the porosity increases with decreasing porosity. However, the increase in the uncertainty in the mass deposition rate is much less than the increase in the uncertainty in the porosity,

i.e. with the porosity of 0.2, the uncertainty in the porosity is 100%, but the uncertainty in the mass deposition rate is only about 30%. Therefore, the presented method for defining the porosity of the fouling layer can be utilized especially for low density fouling layers when the porosity is rather high, preferably over 0.8, but also for the fouling layer with lower porosities.

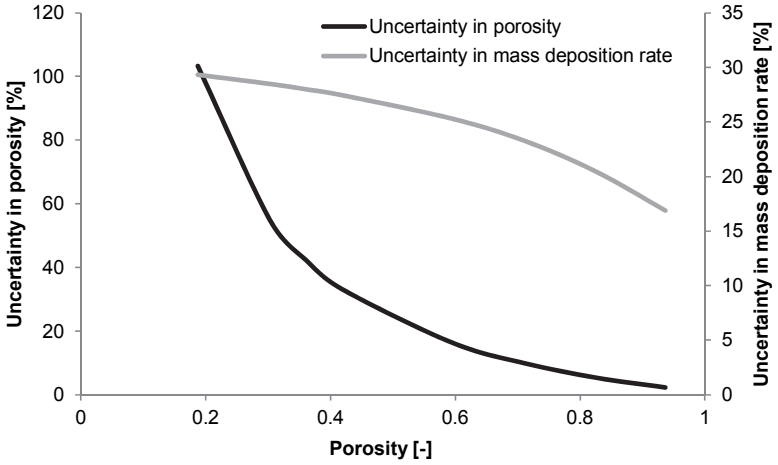

Fig. 19. Variation of the uncertainty in the porosity (black line) and in the mass deposition rate (gray line) for different porosities.

4.2.2 Regression of the model parameters (Paper II)

The kinetic parameters (the activation energy (E_a) and the pre-experimental factor (k_0)) that are needed to model crystallization fouling depend on the process conditions (T_s, v, C_b), the fluid, and the system (Fahiminia *et al.* 2007, Pääkkönen *et al.* 2009, Rose *et al.* 2000). In order to model crystallization fouling accurately, these parameters need to be determined considering all of these factors. In this work, the kinetic parameters are determined using non-linear regression. The regression is performed by Origin 8.6 using a nonlinear least square fitting with two parameters (E_a, k_0) and one (T_s) or two (T_s, v) independent variables depending on the model.

Four different fouling models (namely integration (Eq. 20), integration-diffusion (Eq. 21), integration-velocity (Eq. 22), and integration-diffusion-velocity (Eq. 23)) introduced in Section 2.2.4 are used in the regression. The mass

transfer coefficient is estimated from Eq. 42, including the enhancement correction for the entrance region presented in Section 2.3.4. The time scaling factor is modeled using Eq. 15 and Eq. 16, in which the friction coefficient is estimated from Eq. 30.

The constants used in the models are given in Table 4. The bulk concentration (C_b) is considered constant since conductivity control is used in the experiments to replace the ions deposited on the surface. The diffusion coefficient at the film temperature is defined using Eq. 38. The diffusion coefficient of the Ca^{2+} ion at 25 °C is chosen as a reference value (D_{ref}) because diffusion is controlled by the slower moving ion (Segev *et al.* 2012), and Ca^{2+} ion has the lowest diffusion coefficient of the ions in the studied system. The hydraulic diameter (D_h) and the length of the test section (X) used in the enhancement correction for the entrance region are set by the dimensions of the experimental set-up.

Table 4. Model constants (Paper II).

Constant	Unit	Value
C_b	[kg/m^3]	0.4197
D_{ref}	[m^2/s]	$0.79 \cdot 10^{-9}$
D_h	[m]	0.03
X	[m]	0.2

The temperature dependencies of the diffusion coefficient, density, and viscosity of the fluid were included into the models as described in Paper III. The properties in the mass transfer coefficient and the friction factor are estimated at the film temperature, and the time scaling factor is calculated at the initial surface temperature (Fahiminia *et al.* 2007, Rose *et al.* 2000). The experimental mass deposition rate is obtained from Eq. 54. The properties of the fouling layer needed in Eq. 54 are determined in Section 4.2.1. The parameters obtained in the regression for different models are presented in Table 5.

Table 5. Regression results of the studied models (Paper II).

Model	Eq.	E_a	k_0, k_0'	R^2
Integration	20	179 kJ/mol	$1.65 \cdot 10^{22}$ m^4/(kg·s)	0.74
Integration-diffusion	21	170 kJ/mol	$1.69 \cdot 10^{21}$ m^4/(kg·s)	0.59
Integration-velocity	22	148 kJ/mol	$1.62 \cdot 10^{20}$ m^4/(kg·s^2)	0.78
Integration-diffusion-velocity	23	113 kJ/mol	$1.65 \cdot 10^{22}$ m^4/(kg·s^2)	0.62

Figures 20 and 21 present the mass deposition rates obtained by each model at different heat fluxes and flow velocities, respectively. The squared symbols in Figs. 20-21 represent the measured mass deposition rates with their 95% uncertainty bounds.

The integration (R^2=0.74) and integration-velocity (R^2=0.78) models provide the best fit with the experimental data. These models assume that the mass transfer of the ions is so high that the mass deposition rate is not limited by the mass transfer through the boundary layer, but the surface integration controls fouling, as was discussed in Section 4.1.4. The integration-velocity model, which includes the residence time of the fluid at the wall, and thus the probability of the crystals attaching to the surface, provides a slightly better fit than the surface integration model. With the models that take into account the mass transfer, i.e. integration-diffusion and integration-diffusion-velocity models, the fitting is slightly weaker (R^2 numbers 0.59 and 0.62, respectively). The deviation is larger especially at high heat fluxes and at low flow velocities, as can be seen in Figs. 20 and 21.

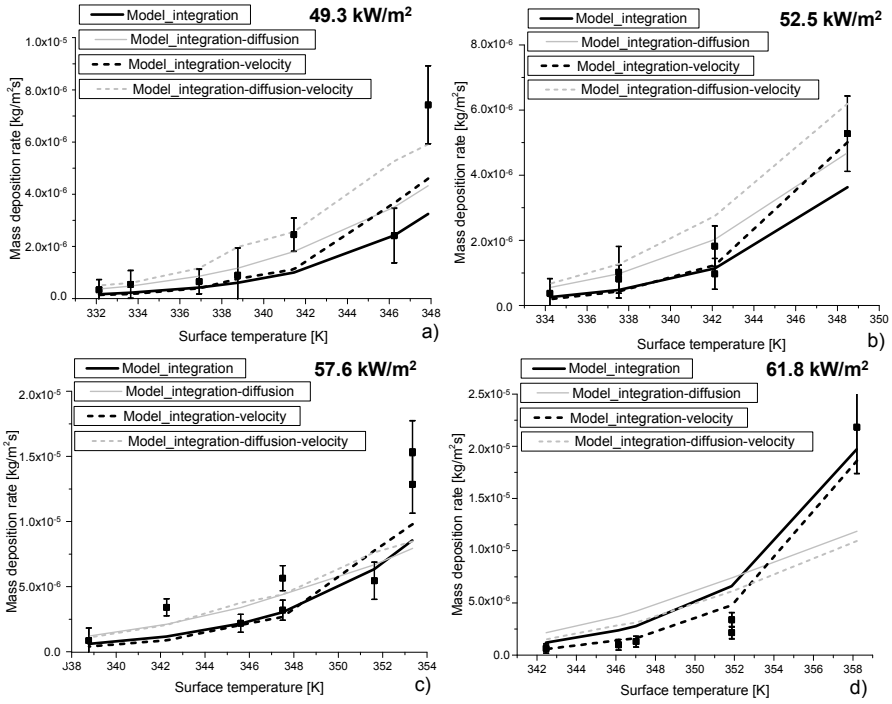

Fig. 20. Comparison between the models (lines) and the experimental data (symbols with uncertainty bars) at different heat fluxes (Paper II, published by permission of Elsevier).

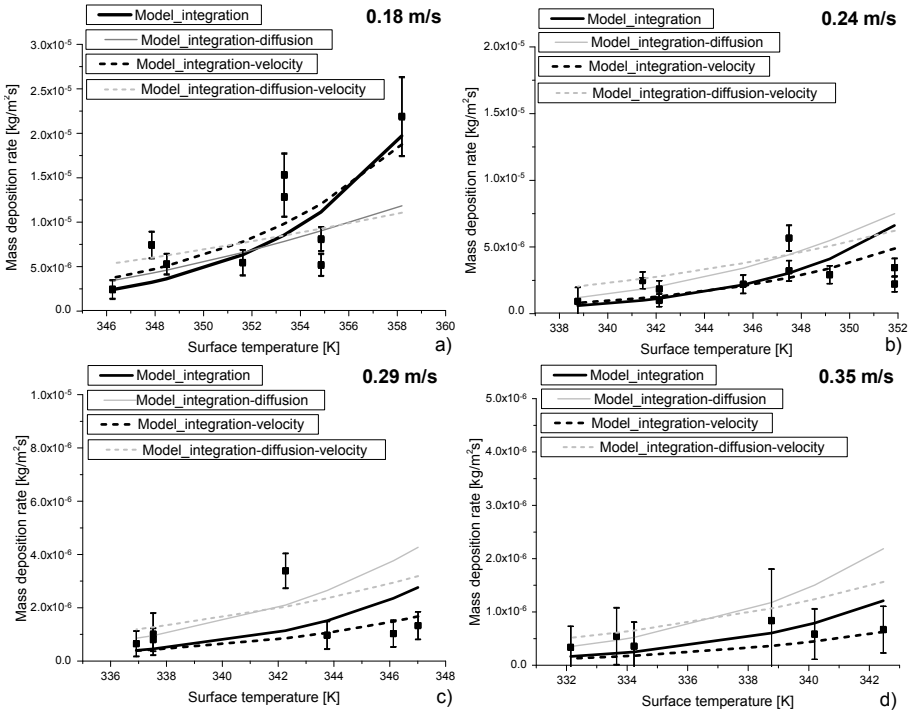

Fig. 21. Comparison between the models (lines) and the experimental data (symbols with uncertainty bars) at different flow velocities (Paper II, published by permission of Elsevier).

4.2.3 Determination of the governing sub-processes in crystallization fouling models (II)

In the experimental studies (Paper I, Section 4.1.4), the fouling process was found to be controlled by the surface integration sub-process. In addition, it was shown in Fig. 17 that the mass deposition rate decreases when the flow velocity is increased at a constant wall temperature, which indicates that shorter residence time of the fluid at higher flow velocities prevents the ions from sticking to the surface. (Paper I) The predictions of the mass deposition rate as a function of flow velocity are presented in Fig. 22.

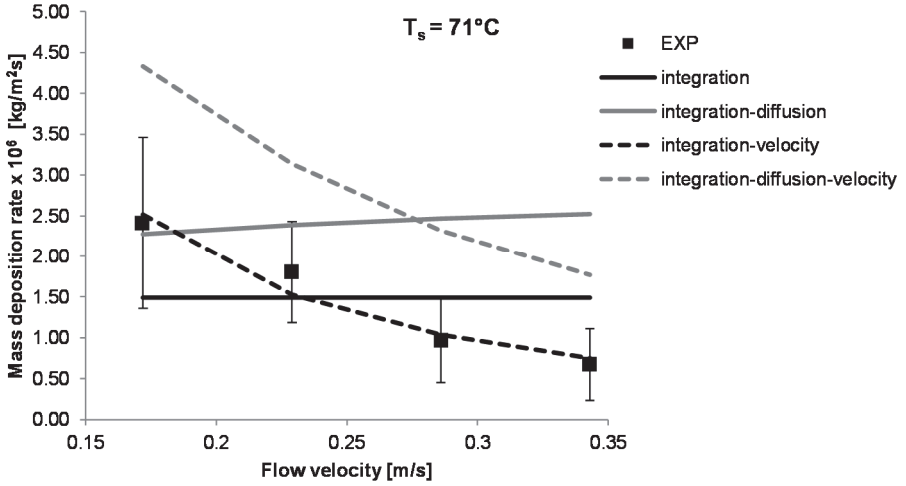

Fig. 22. Modeled and experimental mass deposition rates as a function of flow velocity at constant surface temperature (Paper II, published by permission of Elsevier).

Fig. 22 shows that the integration model gives a constant mass deposition rate for all of the flow velocities because the surface temperature is constant and the model does not contain any flow dependent terms. The mass deposition rate calculated by the integration-diffusion model increases slightly with flow velocity because the mass transfer coefficient increases with velocity. On the other hand, the integration-velocity and integration-diffusion-velocity models predict a decrease in the mass deposition rate with increasing velocity due to the addition of the velocity dependent time scaling factor to the models. The integration-diffusion-velocity model over-predicts the experimental mass deposition rate at the studied surface temperature (71 °C) and will most likely underestimate the mass deposition rate at higher surface temperatures as seen in Fig. 21. The most accurate prediction is obtained by the integration-velocity model, which agrees with the experimental data within the experimental uncertainty bounds. Therefore, inclusion of the velocity dependent time scaling factor is needed in order to model properly the crystallization fouling of $CaCO_3$ in the studied operating conditions and system.

The controlling fouling mechanism in the model can be defined by calculating the effectiveness factors, which gives a quantitative measure of the degree of mass transfer or surface integration control (Mullin 2001: 228–229).

The effectiveness factor (Eq. 68) is defined using the Damköhler number that represents the ratio of the rate coefficient for the surface integration to the mass transfer coefficient. The effectiveness factors can be defined as

$$\eta_c = \left(1 - \eta_c Da\right)^n, \tag{68}$$

where η_c is the effectiveness factor, Da is the Damköhler number for crystal growth and n is the order of the surface integration process (2 in this thesis). The Damköhler number is calculated as

$$Da = k_r (C_b - C_{sat})^{n-1} (1 - \omega) \beta^{-1}, \tag{69}$$

where ω is the mass fraction of the solute in the solution.

The surface integration controls the crystal growth when the effectiveness factor is close to one. If the effectiveness factor is close to zero, the mass transfer controls the fouling process. (Mullin 2001: 228–229) The effectiveness factors are presented in Table 6 for all of the studied flow velocities at heat fluxes of 52.5 kW/m^2 and 61.8 kW/m^2 using the parameters from the integration model and the mass transfer coefficient from Eq. 42, with the enhancement defined in Section 2.3.4.

Table 6. Effectiveness factors in different conditions.

Heat flux [kW/m^2]	Effectiveness factor			
	v = 0.18 m/s	v = 0.24 m/s	v = 0.29 m/s	v = 0.35 m/s
52.5	0.88	0.96	0.99	0.99
61.8	0.59	0.84	0.94	0.97

Table 6 shows that the effectiveness factor is close to one in most of the conditions. This indicates that the studied crystallization fouling process is controlled by surface integration. Only in the conditions that are the most favorable for the surface integration, i.e. at the highest heat flux and lowest flow velocity, the effectiveness factor (η_c = 0.59) implies that, the mass transfer may affect the results.

Because the integration and integration-velocity models assume infinite mass transfer to the wall and that the surface integration step controls the fouling, they correspond well to the experimental data at the surface integration controlled conditions detected in the experiments.

The integration-diffusion (and integration-diffusion-velocity) model contains two terms: mass transfer of ions to the wall and the integration of the ions to the

crystal lattice. The roles of these terms are elucidated in Fig. 23 by calculating the mass deposition by mass transfer alone (i.e. assuming that mass deposition due to surface integration is infinite), and by surface integration alone (i.e. assuming that the diffusion mass transfer is infinite) (the gray lines in Fig. 23) at the lowest flow velocity. The mass deposition by the surface integration model is presented for comparison (the black line).

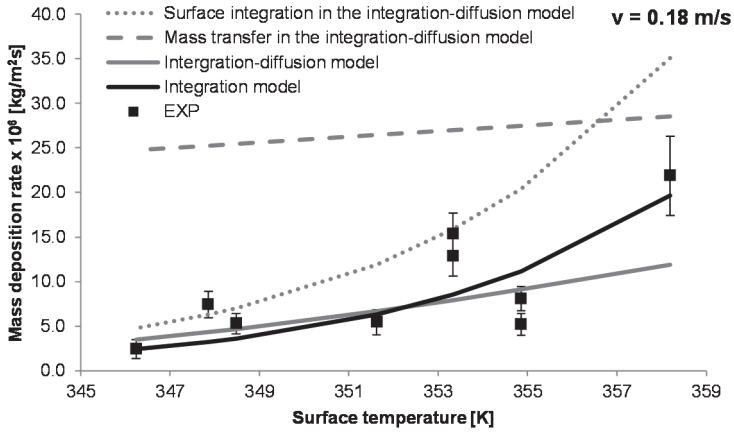

Fig. 23. Comparison of the mass deposition rate by the surface integration and the mass transfer terms in the integration-diffusion model, and the surface integration model for the lowest flow velocity (modified from Paper II, published by permission of Elsevier).

Fig. 23 shows that with the integration-diffusion model, the mass deposition based on the surface integration (the dotted gray line) is lower than the mass deposition based on the mass transfer (the dashed gray line) in most of the conditions. At the higher flow velocities, the limitation of the surface integration is even clearer (Paper II). However, at the highest surface temperature, and the lowest flow velocity (Fig. 23), the mass deposition by the surface integration exceeds the mass deposition by the mass transfer, indicating that in the integration-diffusion model, fouling is controlled by the mass transfer at the lowest flow velocity whereas the surface integration controls all other conditions. Because the mass transfer controlled conditions were not seen in the experiments (see Section 4.1.4), the integration-diffusion model (the solid gray line) under-predicts the experimental mass deposition rate (squared symbols in Fig. 23) at the lowest flow velocity. The reason for the under-prediction of the mass deposition

rate by the integration-diffusion model at the low flow velocity seems to be that the mass transfer model used in the integration-diffusion and integration-diffusion-velocity models slightly under-estimates the mass transfer at the lowest flow velocity. This gives too much control for the mass transfer when compared to the experimental results and therefore explains the deviation between the simpler model (integration model) and the more detailed model (integration-diffusion model).

The mass transfer coefficient used in the mass transfer modeling is influenced by a number of parameters each with their own uncertainty. For example, density and viscosity in the Reynolds and Schmidt numbers, and the diffusion coefficient are dependent on the temperature at which they are calculated (bulk, film or surface temperature). In this thesis, the film temperature is used, but choosing a higher temperature value would lead to a higher mass transfer coefficient.

In addition, an increase in the surface roughness could increase the mass (and heat) transfer. The relative roughness is found to deviate less than 10% from the hydraulically smooth surface (Bird *et al.* 1960: 186) according to the measured thickness (Paper II). However, when the fouling is the strong, i.e. the flow velocity is low and the surface temperature is high, the relative roughness may be larger. However, according to Mottahed and Molki (1996), the heat and mass transfer entrance region of the duct is significantly reduced by the surface roughness. This means that even if the mass and heat transfer increased due to the increased roughness, the entrance region would be reduced due to roughness, which would further decrease the mass and heat transfer. Therefore, it is reasonable to assume constant heat and mass transfer coefficients for the experiments.

Because the mass transfer model is sensitive to the mass transfer coefficient, which has a number of uncertain parameters, the integration-diffusion (and integration-diffusion-velocity) model does not give the best fit when the surface integration controls the fouling. Therefore, for accurate modeling, the mass transfer term should be neglected from the model equations if the surface integration controls the fouling, as is the case in this thesis. As a result, the integration-velocity model is suggested to be used for modeling the surface integration controlled crystallization fouling.

4.2.4 Study on the crystallization fouling mechanism using the developed model (Paper III)

The surface integration controlled fouling model (integration-velocity model) used in this thesis is composed of three main terms, which are the rate coefficient for the surface integration (k_r), the concentration difference between the bulk and saturation concentrations (C_b–C_{sat}), and the time scaling factor (t_{sf}). The effects of the flow velocity and the surface temperature, which are common operating parameters in heat exchangers, on these terms, are presented in Fig. 24.

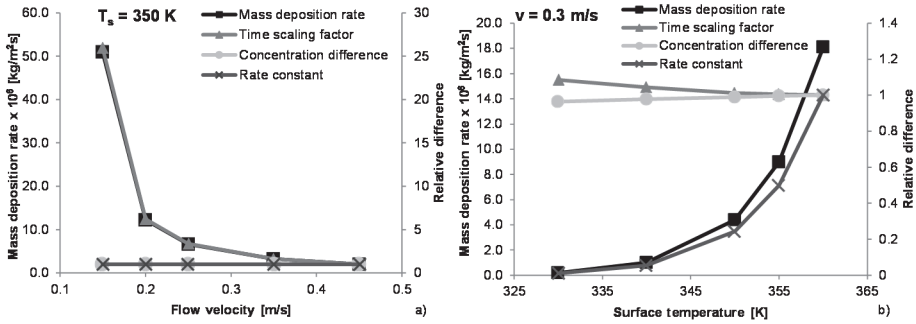

Fig. 24. The mass deposition rate (black lines), and the relative difference of the time scaling factor, the concentration difference and the rate constant (a) as a function of the flow velocity at a constant surface temperature (T_s = 350 K), and (b) as a function of the surface temperature at a constant flow velocity (v_{in} = 0.3 m/s). The relative differences are $k_r/k_{r,ref}$, $(C_b–C_{sat})/(C_b–C_{sat})_{ref}$ and $t_{sf}/t_{sf,ref}$, where the reference values are at the highest velocity (a) or temperature (b) (Paper III).

Fig. 24 (a) denotes that the mass deposition rate (the black line with squares), at the constant surface temperature, depends strongly on the flow velocity. The increase in the mass deposition rate as the flow velocity decreases is due to an increase in the time scaling factor (the gray line with triangles), which is caused by a decrease in the shear stress as the velocity decreases. On the other hand, the rate coefficient (the gray line with crosses) and the concentration difference (the gray line with circles) remain constant as the flow velocity decreases. The results show the importance of the inclusion of the time scaling factor in the model since it correctly models the decreasing mass deposition rate with the increasing flow velocity.

According to Fig. 24 (b), the mass deposition rate increases significantly with the surface temperature when the flow velocity is kept constant. Most of the change in the mass deposition rate due to a change in the temperature is due to the change in the rate constant (the gray line with crosses) with temperature. However, the time scaling factor (the gray line with triangles) and the concentration difference (the gray line with circles) play a small role. The concentration difference increases slightly with the surface temperature due to the temperature dependence of the saturation concentration. On the other hand, the time scaling factor decreases with the increasing surface temperature. The variation in the time scaling factor with the temperature is due to the variations in the properties of the fluid (i.e. in the density, viscosity and diffusion coefficient) with temperature.

The results in Fig. 24 showed that the most important parameters affecting the crystallization fouling are the rate constant obtained from the modeled surface temperature, and the time scaling factor obtained from the modeled shear stress. Fig. 25 presents the sensitivity of the model to these parameters.

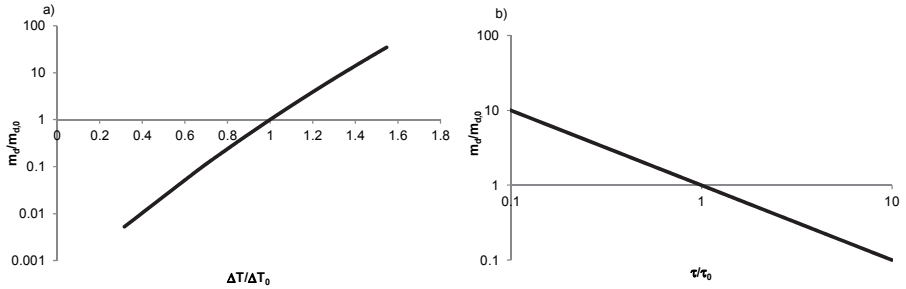

Fig. 25. Sensitivity of the model to the surface temperature (a), and the shear stress (b) (Paper III).

Fig. 25 shows that the presented model is very sensitive to the surface temperature: the mass deposition rate changes tenfold if the surface temperature is increased by 35%. Meanwhile, the shear stress must be changed by a factor of ten to change the mass deposition rate by a factor of ten. Therefore, the model is about 30 times more sensitive to the surface temperature than to the shear stress. The results show the importance of the accurate determination of especially the surface temperature, but also the shear stress. For simple cases these can be defined from the measurements or correlation, but for definition of the local

values of complicated geometries, such as corrugated plate heat exchanger surface, CFD is a very useful tool.

4.2.5 CFD modeling of crystallization fouling (Paper III)

In Section 4.2.3, the crystallization fouling model that includes surface integration and the time scaling factor, i.e. the integration-velocity model, was found to represent most reliably the experimental data. Therefore, this model is implemented in the ANSYS Fluent 14.0 CFD program to provide a novel combination of the crystallization fouling model and CFD. In this section, the model is validated against experiments and its applicability is discussed.

Validation of the heat transfer model

Temperature has a considerable effect on the crystallization fouling of heat exchangers. Therefore, an accurate heat transfer modeling is an essential part of the fouling models. The heat transfer CFD model used in this thesis has been validated with the temperature measurements of the flat plate experimental set-up by Pääkkönen *et al.* (2007). Fig. 26 presents the temperature difference between the inlet and outlet of the test section for different flow velocities. The comparison is made between the results from CFD, a theoretical heat balance and the experimental measurements. (Pääkkönen *et al.* 2007) The experimental measurements are presented with their 95% uncertainty bounds, which are quite large since the temperature difference between the inlet and outlet is small.

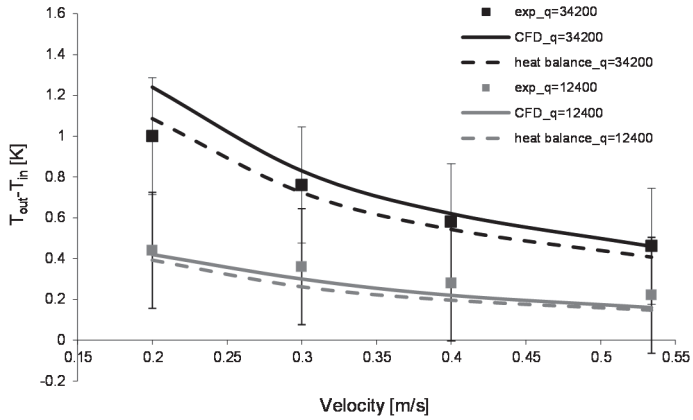

Fig. 26. Temperature difference between inlet and outlet of the set-up calculated from a theoretical energy balance, experimental measurements, and CFD (modified from Pääkkönen *et al.* 2007).

Fig. 26 indicates that the CFD predicts the temperature change of the fluid as it flows through the experimental set-up inside the experimental uncertainty. Small deviations to the measurements may be explained by the inaccuracy in the measurements, which are suspected to be due to incomplete mixing of the fluid before the thermocouple. In addition, Fig. 26 denotes that both the experiments and the CFD satisfy the energy balance. Pääkkönen *et al.* (2007) have also shown that the wall heat transfer coefficient modelled by CFD corresponds well with the heat transfer coefficient obtained from the experimental measurements (using Eq. 33) in the range of flow velocities used in this thesis.

Validation of the fouling model

The developed CFD fouling model is validated against experimental data in Figs. 27-29 in different operating conditions. Fig. 27 presents the modeled average mass deposition rate on one test surface for various heat fluxes and Reynolds numbers in comparison with the experimental mass deposition rates and their 95% uncertainty bounds. The validation of the modeled fouling resistance is presented in Fig. 28 for a varied Reynolds number at a constant heat flux. In modeling, the standard k-ε turbulence model with the Enhanced Wall Treatment is used in order to model accurately the near wall area, which is of the interest in the fouling modeling (Paper III).

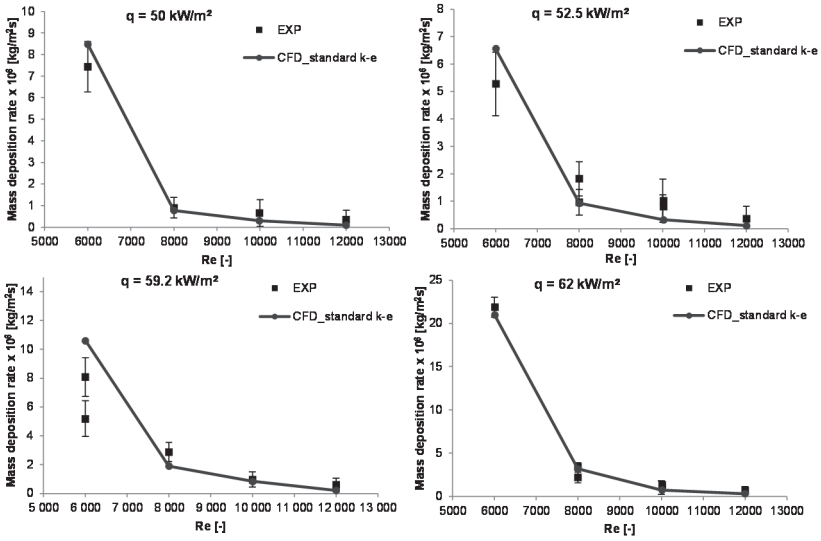

Fig. 27. The experimental (with 95% uncertainty bounds) and modeled mass deposition rates at different heat fluxes for a varied bulk fluid Reynold numbers (inlet flow velocities between 0.2 m/s and 0.4 m/s) with C_b = 0.418 g/l and T_b = 303 K (Paper III).

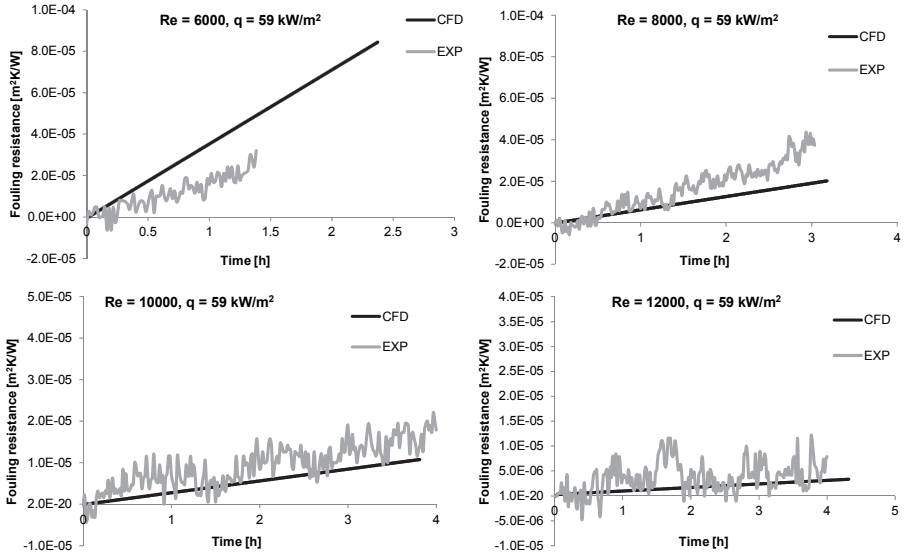

Fig. 28. Comparison between the experimental and modeled (with the standard k-ε turbulence model) fouling resistance curves for a varied flow velocity at the heat flux of 59 kW/m^2 (Paper III).

Fig. 27 indicates that the modeled mass deposition rate corresponds with the experimental data within the experimental uncertainty bounds in most of the conditions. Also, the modeled fouling resistances in Fig. 28 follow well the experimental fouling resistances during the linear growth of the fouling layer. According to the results in Figs. 27 and 28, the deviation between the numerical and experimental data is the largest at the lowest Reynolds number (i.e. at the lowest flow velocity). The standard k-ε turbulence model used in those simulations is intended for fully developed turbulent flows. However, the flow at the lowest Reynolds numbers may still be at the transition zone. Therefore, the RNG k-ε turbulence model, which is suitable for low *Re* flows (ANSYS Inc. 2011a), was also tested. The results in Paper III showed that the RNG standard k-ε turbulence model works better at the lowest Reynolds number compared to the standard k-ε turbulence model, but at higher Reynolds numbers, the RNG standard k-ε turbulence model under-predicts the mass deposition rate.

Validation of the used CFD fouling model for different bulk concentrations is presented in Fig. 29. The RNG k-ε turbulence model is used in the concentration

variation simulations because the validation experiments were conducted at the lowest Reynolds number.

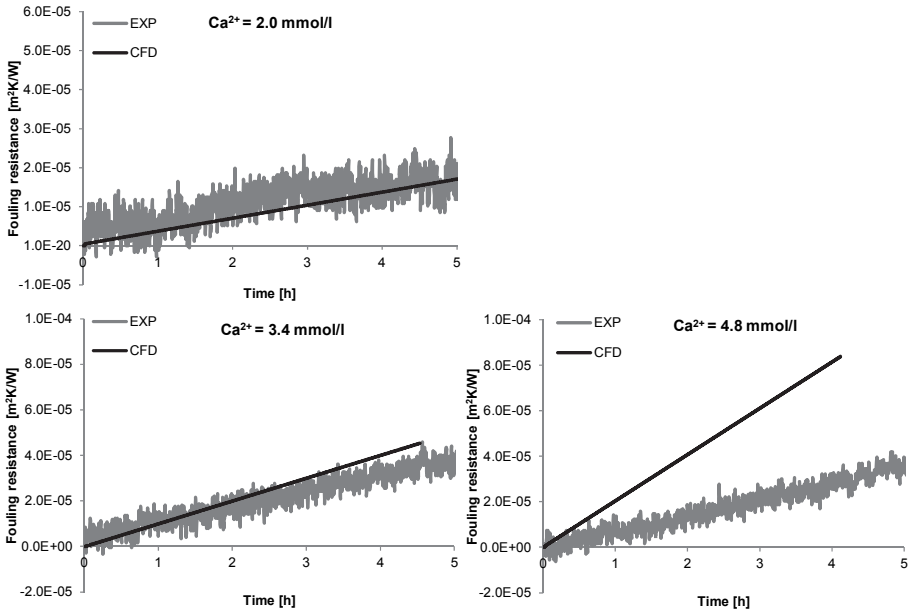

Fig. 29. Fouling resistance curves for varied bulk concentration with v_{in} = 0.2 m/s (*Re* = 6000), q = 55 kW/m^2, T_b = 303 K. The RNG k-ε turbulence model is used in the CFD model (Paper III).

According to Fig 29, the fouling resistances predicted by the CFD fouling model correspond well with the experimental data at the bulk concentrations of 2.57 mmol/l and 4.18 mmol/l (Ca^{2+} concentrations of 2.0 mmol/l and 3.4 mmol/l, respectively). At the highest bulk concentration, 5.78 mmol/l (denoting the Ca^{2+} concentration of 4.8 mmol/l), the model significantly over-predicts the fouling resistance. The reason for the over-prediction may be related to high supersaturation and homogeneous crystallization in the bulk fluid in the experiments. The homogeneous nucleation in the bulk fluid may take place within a reasonable time if a critical supersaturation degree is exceeded (Mullin 2001: 185). According to Elfil & Roques (2004), in the $CaCO_3$-CO_2-H_2O system, the homogeneous nucleation in the bulk fluid may take place when the Ca^{2+} concentration is over 4 mmol/l at pH 8, which corresponds to this study. At the highest concentration used in this thesis, the Ca^{2+} concentration is 4.8 mmol/l, and

homogeneous crystallization in the bulk fluid is probable during the experiments. Crystallization in the bulk fluid during an experiment would decrease the bulk concentration and lower the driving potential for crystallization and thus decrease the mass deposition to the surface. Because the bulk crystallization is not included in the fouling model, the model over-predicts the mass deposition rate at high supersaturations.

Limitations of the developed model

The fouling model introduced in this thesis is intended for the surface integration controlled fouling conditions. However, if the flow velocity is decreased enough, the mass transfer of ions to the vicinity of the surface begins to restrict the fouling process at some point. CFD can be used to study the interfacial concentration using the species mass transfer model and therefore the use of rather uncertain mass transfer correlations (Brahim *et al.* 2003, Mwaba *et al.* 2006c, Pääkkönen *et al.* 2015) can be avoided.

Fig. 30 presents the mass deposition rates (the left vertical axis) when the bulk concentration (the solid black line) and the interfacial concentration (the dashed black line) are applied in the fouling model, in comparison with the experimental values. The right vertical axis presents the ratio between the interfacial concentration and the bulk concentration when the interfacial concentration is used in the fouling model.

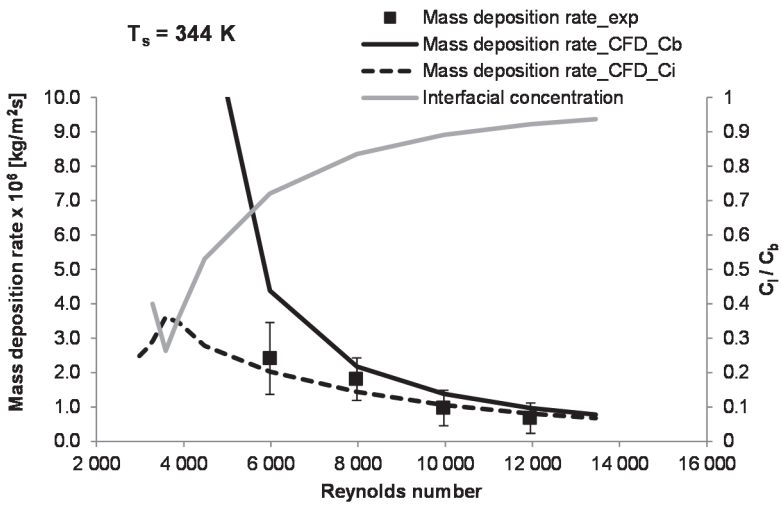

Fig. 30. The modeled mass deposition rates calculated with the interfacial concentration (dashed black line) and with the bulk fluid concentration (solid black line), and the relative difference in the interfacial concentration (gray line) at constant surface temperature (T_s = 344 K) with the varied bulk fluid Reynold number (inlet flow velocities between 0.1 m/s and 0.45 m/s) modeled with the standard k-ε turbulence model (Paper III).

Fig. 30 shows that the modeled mass deposition rates are within the experimental uncertainty at higher flow velocities. At Reynolds number of 6000 and lower, the model, in which the bulk concentration is used, seems to over-predict the mass deposition rate; whereas the model in which the interfacial concentration is used, predicts the mass deposition rate more accurately. This indicates that the mass transfer of ions begins to affect the fouling process at lower Reynolds numbers. At *Re* less than 3300, the low interfacial concentration restricts the mass deposition such that the mass deposition begins to decrease as the flow velocity (*Re*) decreases. Therefore, in order to model low Reynolds numbers, the interfacial concentration should be considered in the model. However, it should also be noted that the applicability of the turbulence models at low Reynolds numbers is questionable as noted previously.

In addition, accurate modeling of the interfacial concentration requires information about the roughness of the fouling layer, especially if the roughness effect is considerable since the roughness affects the mass and heat transfer near

the surface (Albert *et al.* 2011, Mottahed & Molki 1996). In this thesis, the fouling layers have been nearly hydraulically smooth, and therefore the effect of roughness has been negligible under most of the conditions (Paper II). However, at the low Reynolds numbers, both the surface temperature and the time scaling factor are high, which means that the mass deposition rate is also high and the thickness of the fouling layer, and further the effective roughness (x/D_h) increases. At some point, the effective roughness may become large enough to affect (i.e. increase) the mass and heat transfer. The increased mass transfer would increase the interfacial concentration, which also increases the mass deposition rate. On the other hand, the increased heat transfer would decrease the surface temperature, which would decrease the rate constant for the surface integration and the supersaturation. This would further reduce the mass deposition, even though the time scaling factor would slightly increase due to the lower surface temperature. Therefore, an appropriate roughness model should be implemented in CFD if the roughness is suspected to have a considerable effect on fouling.

4.2.6 Application of the model for process optimization

In this section, the developed fouling model is applied in a case study to predict the decrease in the heat transfer rate due to surface integration controlled crystallization fouling. In addition, the effect of different cleaning cycles on the operation of the process is studied.

Fig. 31 presents the heat transfer rate, calculated from Eqs. 5 and 7, as a function of the surface temperature. In the calculation of the heat transfer rates, the resistances of the process fluid, wall, and the fouling layer are taken into account, and correspond to the conditions of the experimental set-up used in this thesis. The black line in Fig. 31 denotes the heat transfer rate with the clean surface and the gray lines denote the average heat transfer rates during one cleaning cycle for the fouled surface when the cleaning cycle is 1, 2 or 5 days.

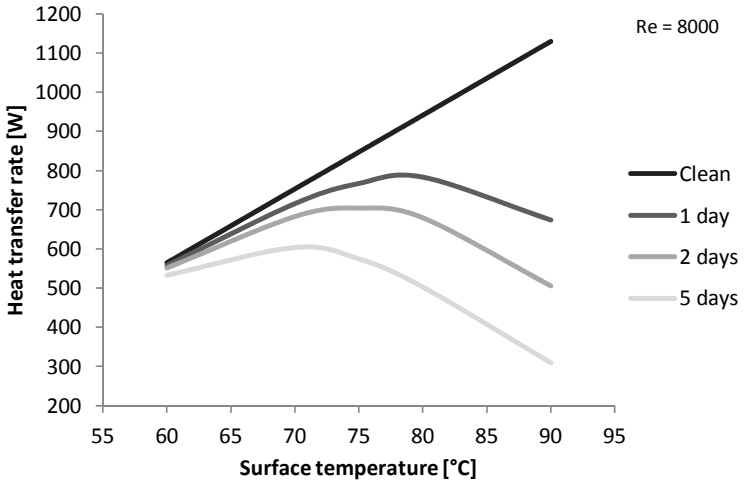

Fig. 31. The effect of fouling on the heat transfer rate for different surface temperatures and cleaning period.

Fig. 31 shows that fouling clearly reduces the obtained heat transfer rate. For a clean heat exchanger (i.e. with no fouling), the heat transfer rate increases linearly with the surface temperature. However, with fouling, the increase in the surface temperature increases the average heat transfer rate only until a certain maximum heat transfer rate, which depends on the cleaning cycle, is achieved. If the surface temperature is further increased beyond this point, the obtained heat transfer rate begins to decrease. Fig. 31 also shows that the higher the surface temperature, the more often the heat exchanger needs to be cleaned in order to retain the target average heat transfer. In addition, Fig. 31 demonstrates that the same average heat transfer rate is obtained at two different surface temperatures. This indicates that increasing the surface temperature does not always increase the heat transfer rate because crystallization fouling increases with surface temperature.

According to Fig. 31, with a one day cleaning cycle, the maximum heat transfer rate is about 790 W, which is obtained at the surface temperature of 78 °C. For the clean surface, the same surface temperature would give a 13% higher heat transfer rate. If the cleaning cycle is increased to 2 days, the maximum heat transfer rate is about 700 W at 75 °C, which is about 18% less than for the clean surface at the same temperature. If the cleaning cycle is 5 days, the maximum heat transfer rate is 600 W at 72 °C, which is 24% less than for the

clean surface. Therefore, prolonging the cleaning cycle reduces the maximum heat transfer rate, but also the surface temperature at which the maximum heat transfer rate occurs. This means that for example, if the target average heat transfer rate is 700 W, the surface temperature may be 70 °C if the cleaning cycle is one day, but with a two day cleaning cycle, the surface temperature needs to be increased to 75 °C in order to reach the target heat transfer rate. This means that the target heat transfer rate can be met with a lower surface temperature when the heat exchanger is cleaned more frequently.

This case study shows that the developed crystallization fouling model can be used to identify the maximum average heat transfer rate for a certain heat exchange cycle. This knowledge is useful for optimizing the time interval between cleaning cycles for a given process.

4.3 Abatement of fouling by surface modifications

Fouling may be reduced by various methods, as presented in Section 2.1.4, e.g., by physical surface modifications. Physical surface modifications do not require any additional chemicals that might contaminate the process fluid or be harmful for nature. In this section, experimental and numerical methods are used to study fouling abatement by surface modifications.

4.3.1 Fouling experiments (Paper IV)

The effect of the micron scale (from 20 to 50 μm) surface shape (see Section 3.1.2) on the fouling performance of the heat transfer surface is studied by laboratory scale experiments (Paper IV). The performance of the patterned surface is compared to the performance of the flat surface.

The fouling rates, which describe the change in the fouling resistance during the linear growth period of the fouling process, are presented in Fig. 32. The flat surface has the highest fouling rate; whereas the patterns A and B show a slightly higher fouling rate than pattern C, which has the lowest fouling rate. Therefore, the curved shape of the pattern C (see cross section of the pattern C in Fig. 13 in Section 3.4.1) seems to be the most promising from the studied patterns in terms of reducing the fouling rate by the surface modifications.

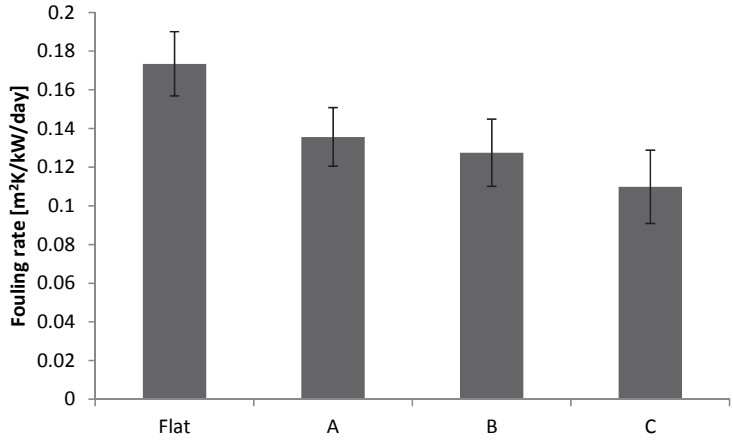

Fig. 32. Fouling rate of the patterned and the flat surfaces with the 95% uncertainty bounds. The different patterns are shown in Fig. 9 in Section 3.1.2.

The fouling experiments give information about the general fouling behavior of different surface modifications. However, conducting fouling experiments is laborious and time consuming, and requires a suitable experimental set-up. Therefore, comparison between the surface modifications by modeling methods would be beneficial. The behavior of pattern C in convective heat transfer conditions is therefore studied in the next section in more detail using CFD.

4.3.2 CFD modeling of hydrodynamics and heat transfer (Paper IV)

The results in Section 4.2.4 have shown that crystallization fouling is mainly governed by the surface temperature and the shear stress at the wall when the fouling process is controlled by the surface integration. The surface temperature and the wall shear stress may be obtained by 2D CFD modeling of hydrodynamics and heat transfer with the modified surface geometry (see Section 3.4.1). The results are compared to the results of the flat surface in corresponding conditions. The pattern C, which was found in the experimental studies to be most promising to reduce fouling, is used as an example. Fig. 33 presents the shear stress (a) and the surface temperature (b) at the heated wall for both the patterned and the flat geometries.

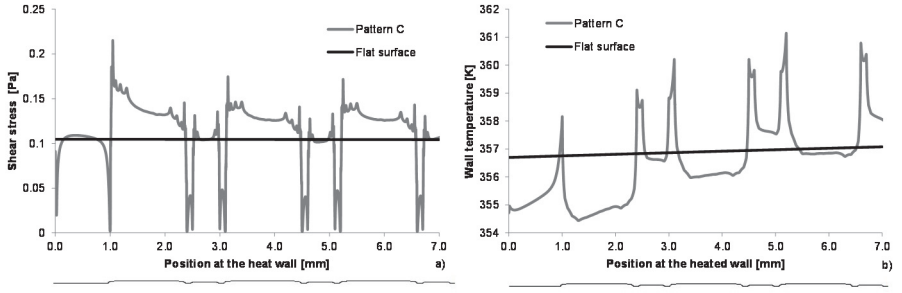

Fig. 33. Shear stress (a) and temperature (b) along the heated wall of the patterned (gray line) and flat (black line) surfaces. The surface profile of pattern C is presented below the figures (Paper IV, published by permission of TTP).

According to Fig. 33, the shear stress and temperature profiles of the patterned surface differ significantly from the profiles of the flat surface. Based on CFD, these changes are due to vortices that occur before and after the bigger convex. The shear stress (Fig. 33 (a)) is increased by about 40% on the convex part of the bigger pattern when compared to the flat surface. In addition, the shear stress is increased especially at the leading edges of the patterns. On the other hand, the shear stress is nearly zero in the concaves dips due to a low flow velocity in these areas. The changes in the flow velocity affect the temperature field of the system. Fig. 33 (b) shows that the wall temperature is higher at the concave parts of the surface, where the flow velocity and further the shear stress are low, and lower over the convex parts, where the flow velocity is higher. The lower surface temperature in the convex parts of the surface is a result of a higher convective heat transfer coefficient (*Nu*) due to the higher flow velocity for a constant heat flux. Similarly, in the concave parts of the surface, the convective heat transfer is lower because the flow velocity is lower which results in a higher surface temperature for a constant heat flux.

An increase in temperature increases the crystallization fouling of $CaCO_3$ markedly (Papers I and III). According to the CFD results, temperature is higher at the concaves, which may therefore be more prone to crystallization fouling compared to the flat surface. On the other hand, the convex parts have a lower temperature than the flat surface and therefore these areas may be less prone to fouling. In the convex parts, the shear stress is also higher compared to the flat surface. The increased shear stress may decrease the residence time of the fluid near the wall and thus reduce the attachment of the ions to the surface and further

reduce the crystallization fouling (Fahiminia *et al.* 2007). In addition, an increasing shear stress enhances the removal of the crystals from the surface as denoted by Bansal (2008) and Lee *et al.* (2006). However, the removal of the crystalline depositions from the surface is not important for the conditions in this thesis (see Section 4.1.1). Therefore, the reduced crystallization fouling rate of the pattern C seen in the experiments may be explained by the decreased wall temperature and increased shear stress in the large part of the patterned surface.

4.3.3 Fouling modeling

The observations carried out based on the CFD modeling of the hydrodynamics and heat transfer are verified by calculating the mass deposition rate based on the temperature and shear stress given by CFD. The obtained mass deposition rates presented in Fig. 34 show that on most of the heated wall the deposition rate is lower with the patterned surface than with the flat surface. Especially, the larger convex areas have lower deposition rates with the patterned surface because of the high shear stress and the low surface temperature compared to the flat surface (Fig. 33 (b)). The smaller convex areas have higher surface temperature (Fig. 33 (b)) than the flat surface but due to the effect of the shear stress the mass deposition rate on those areas is close to that of the flat surface. The concaves have higher temperature and a very low shear stress and therefore the mass depositions rate is about four times higher (excluding the very high peaks in the corners of the concaves) than with the flat surface. It should be noted that the shear stress changes about ± 70% along the patterned surface whereas the temperature changes only about ± 0.8%. Therefore, even though the model was found to be about 30 times more sensitive to the temperature than the shear stress (see Section 4.2.4), the shear stress affects more to these results than the temperature because the change in the shear stress is about 100 times bigger than the change in the temperature.

Comparing Figs. 33 and 34 shows that the surface temperature and the shear stress provide a good indication of the mass deposition behavior of the surface integration controlled crystallization fouling. In addition, the detailed information from the CFD simulations of the hydrodynamics and heat transfer can be used to calculate the local values of the mass deposition rate.

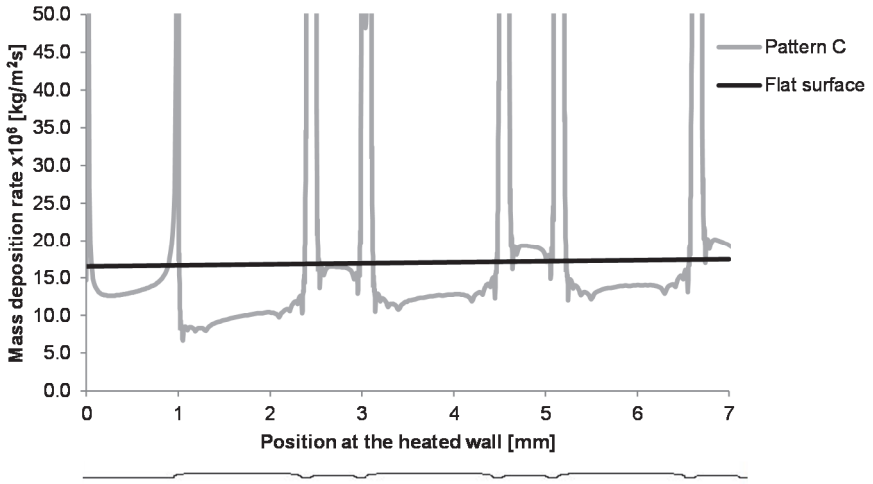

Fig. 34. Mass deposition rate on the flat and patterned surfaces calculated based on the CFD modeling of the hydrodynamics and the heat transfer.

Both, the experimental and the modeled results showed that the patterning may reduce fouling compared to the flat surface. In the experiments, the relative decrease in the fouling rate due to surface patterning was higher, about 36%, than based on the model (about 3%). Whereas CFD gives detailed information about the spatial variations of the parameters along the surface, the experiments give more or less average values for the surface. Therefore, extremely large or small values of the significant parameters affect markedly on the modeled mass deposition rate. In addition, the model is very sensitive to the temperature and therefore, especially the surface temperatures of the compared cases, need to correspond closely with each other. Since the surface temperature is evolving over the surface, modeling of the whole geometry (entire test section) would be beneficial for comparison between both the flat and patterned surface models and the modeled and measured mass deposition rates on a patterned surface in order to compare corresponding conditions. As a conclusion, the model is capable to predict reliably fouling on complex surfaces as long as the positions on the surface, in which the fouling is observed, corresponds to each other.

5 Summary and conclusions

Energy-efficient industrial processes are essential for reduced emissions that cause global climate change. Fouling, which is the deposition of undesired material on heat transfer surfaces, decreases significantly the energy efficiency of processes by reducing the heat transfer and increasing the pressure drop of the equipment, and causes challenges in the design, operation and maintenance of equipment. In addition to the harmful environmental effects, fouling reduces significantly the economic profitability of industrial process.

This thesis aims to reduce fouling and therefore improve the energy efficiency of processes by increasing the understanding of crystallization fouling and providing a validated model for studying crystallization fouling on heat transfer surfaces. The main objectives of the research were to determine the effects of the operating conditions on crystallization fouling in order to identify the most important parameters, and to define the governing sub-processes in crystallization fouling (Paper I). In addition, the goal was to develop and validate a crystallization fouling model, which can be used to study the effects of different parameters on crystallization fouling, and optimize the heat transfer process (Papers II and III). The used methods were then applied to study the abatement of fouling by surface modifications (Paper IV).

In the laboratory scale experiments, the crystallization fouling of $CaCO_3$ on a flat heat exchanger surface increased with an increase in the heat flux, which increased the surface temperature, and decreased with an increase in the flow velocity, which decreased the surface temperature and increased the shear stress. The experimental uncertainty was also quantified in order to evaluate the largest sources of uncertainty and the reliability of the results. The experiments showed that the surface integration sub-process controls the crystallization fouling of $CaCO_3$ in the studied system and operating conditions. In addition, it was concluded that the residence time of the fluid near the wall affects significantly the fouling rate since the fouling rate decreased with increasing flow velocity at a constant surface temperature.

To convert the experimental fouling thermal resistances to mass deposition rates, which are the outputs of fouling models, porosity, density and thermal conductivity of the fouling layer were needed. The properties of the fouling layer were defined by determining the density of the air-filled fouling layer after it was removed from the test section (ex-situ measurements of the area, mass and thickness of the fouling layer). Since the ex-situ measurements have high

uncertainties, the uncertainty analysis was used to determine the uncertainty in the properties of the fouling layer and to evaluate the applicability of the ex-situ measurement method to study fouling. Based on the analysis, the uncertainty in the porosity increases as the density of the fouling layer increases. However, the uncertainty in the porosity has only a minor effect on the uncertainty in the mass deposition rate. Therefore, the method is applicable for fouling layers with various porosities, but especially for the fouling layers with low densities and high porosities (preferably $\varepsilon > 0.8$), which is the case in this thesis.

The information gained from the experiments was used to develop models for crystallization fouling. Four different fouling models were built up and their parameters were defined using non-linear regression. Based on the comparison between the regressed models and the experimental results, the fouling model containing the terms for the surface integration and the residence time of the fluid provided the best prediction of the mass deposition rate by crystallization fouling at different heat fluxes and flow velocities. In addition, it was concluded that the inclusion of the residence time of the fluid into the model is essential for the modeling of the decreasing mass deposition rate with the increasing flow velocity, at constant surface temperatures. The sensitivity study of the fouling model containing the surface integration and the residence time showed that the model is very sensitive to the changes in the temperature, but also rather sensitive to the shear stress. Therefore, in order to use the developed model, the surface temperature and shear stress should be defined accurately.

The chosen fouling model was implemented in CFD in order to develop a CFD fouling model to study fouling in complex geometries. The CFD fouling model was validated at various operating conditions, and it was found to correspond very well with the experimental results. It was noticed in the CFD studies that at lower flow velocities, the choice of the turbulence model may affect the results, and at very low velocities, also mass transfer of ions should be modeled in order to take into account the reducing mass transfer at decreasing velocities. In addition, it was noticed that bulk crystallization may be significant at high supersaturations, which reduces the bulk concentration and therefore the rate of the surface crystallization.

The developed methods were applied to study crystallization fouling on patterned surfaces. The fouling experiments were used to determine the surface pattern with the lowest fouling rate compared to a flat surface. The most promising surface pattern was then studied by CFD. CFD modeling of the hydrodynamics and heat transfer in the patterned surface geometry was used to

obtain the surface temperature and shear stress, which were earlier found to be the most important parameters affecting the crystallization fouling. Based on the simulations, the crystallization fouling on the surface was estimated. Both the experiments and models showed that the patterned surface had a lower fouling rate than the smooth surface, therefore indicating the abatement of fouling when the patterned surface was used.

The developed fouling model may be used, for example, to study the decrease in the heat transfer rate due to fouling. This capability was applied to study cleaning cycles for heat exchanges with fouling. According to the case study, increasing the surface temperature increases the average heat transfer rate only until some maximum surface temperature. Beyond that point, the average heat transfer rate decreases due to fouling even when the surface temperature is increased. It was also noticed that the maximum heat transfer rate obtained for a certain surface temperature depends on the cleaning period. More frequent cleaning is needed to obtain a higher heat transfer rate. The case study showed that the model can provide useful information about the optimization of the cleaning cycle and the surface temperature of the heat exchanger.

To conclude, this thesis provides valuable scientific information about crystallization fouling under mainly surface integration controlled conditions. The thesis describes a methodology in which ex-situ measurements of the fouling layer and the uncertainty analysis were used to define reliably the properties of the fouling layer for modeling the mass deposition rate. The thesis also provides a validated crystallization fouling model that can be used to define the most important parameters affecting fouling, and to identify the preferable conditions and cleaning cycles for heat exchangers. In addition, a novel combination of the developed crystallization fouling model and CFD for studying surface integration controlled crystallization fouling of calcium carbonate in complex geometries is presented.

Despite the contributions of this thesis, there is still a need for further studies on crystallization fouling and development of fouling models. The crystallization fouling model used in this thesis is suitable for surface integration controlled conditions. If low flow velocities are studied, possible mass transfer limitations should be taken into account in the model. If the mass deposition rate is high and the forming fouling layer is thick, the effect of the fouling layer (porosity, density, thermal conductivity, and roughness) on the width of the flow channel, local heat flux along the surface, and convective heat and mass transfer should also be considered. To increase the applicability of the model, it would be important to

include bulk fluid phenomena (i.e. crystallization to the bulk fluid and fouling caused by the bulk fluid particles) to the model since few practical systems have filters to exclude these effects. By including these phenomena into the model, a more general fouling model suitable for industrial heat exchangers can be achieved.

References

Albert F, Augustin W & Scholl S (2011) Roughness and constriction effects on heat transfer in crystallization fouling. Chemical Engineering Science 66(3): 499–509.

Anderson JD (1995) Computational Fluid Dynamics. The Basics with Applications. Singapore, McGraw-Hill, Inc.

Andritsos N & Karabelas A (2003) Calcium carbonate scaling in a plate heat exchanger in the presence of particles. Int J Heat Mass Transfer 46(24): 4613–4627.

ANSYS Inc. (2011a) ANSYS FLUENT Theory Guide. 14.0.

ANSYS Inc. (2011b) ANSYS FLUENT User's Guide. 14.0.

ASME (1985) ANSI/ASME PTC 19.1 - 1985 Measurement Uncertainty.

Augustin W & Bohnet M (1995) Influence of the ratio of free hydrogen ions on crystallization fouling. Chemical Engineering and Processing: Process Intensification 34(2): 79–85.

Bansal B, Müller-Steinhagen H & Chen XD (1997) Effect of suspended particles on crystallization fouling in plate heat exchangers. Journal of Heat Transfer 119(3): 568–574.

Bansal B, Chen XD & Müller-Steinhagen H (2003) Use of non-crystallising particles to mitigate crystallisation fouling. Int Commun Heat Mass Transfer 30(5): 695–706.

Bansal B, Chen XD & Müller-Steinhagen H (2005) Deposition and removal mechanisms during calcium sulphate fouling in heat exchangers. International Journal of Transport Phenomena 7(1): 1–22.

Bansal B, Chen XD & Müller-Steinhagen H (2008) Analysis of 'classical'deposition rate law for crystallisation fouling. Chemical Engineering and Processing: Process Intensification 47(8): 1201–1210.

Bansal B, Müller-Steinhagen H & Chen XD (2000) Performance of plate heat exchangers during calcium sulphate fouling—investigation with an in-line filter. Chemical Engineering and Processing: Process Intensification 39(6): 507–519.

Bansal B, Müller-Steinhagen H & Chen XD (2001) Comparison of crystallization fouling in plate and double-pipe heat exchangers. Heat Transfer Eng 22(5): 13–25.

Bansal B & Müller-Steinhagen H (1993) Crystallization fouling in plate heat exchangers. Journal of Heat Transfer 115(3): 584–591.

Bird RB, Stewart WE & Lightfoot EN (1960) Transport phenomena. New York, John Wiley & Sons.

Bohnet M (1987) Fouling of heat transfer surfaces. Chem Eng Technol 10(1): 113–125.

Bott TR (1995) Fouling of heat exchangers. Amsterdam, Elsevier.

Bott TR (1997) Aspects of crystallization fouling. Exp Therm Fluid Sci 14(4): 356–360.

Brahim F, Augustin W & Bohnet M (2003) Numerical simulation of the fouling process. International Journal of Thermal Sciences 42(3): 323–334.

Coleman HW & Steele WG (1999) Experimentation and uncertainty analysis for engineers. New York, Wiley.

Collier J (1981) Heat Exchanger Fouling and Corrosion. In: Kakaç S, Bergles A & Mayinger F (eds) Heat Exchangers "Thermal-Hydraulic Fundamentals and Design". Hemisphere Publication Corporation: 999–1011.

Cooper A (1980) The plate heat exchanger. In: Bhatia MV & Cheremisinoff PN (eds) Process equipment series, Volume 2 – Heat transfer equipment. Lancaster, Technomic Pub Co: 187–211.

Elfil H & Roques H (2004) Prediction of the limit of the metastable zone in the "$CaCO_3$-CO_2-H_2O" system. AIChE J 50(8): 1908–1916.

Epstein N (1994) A model of the initial chemical reaction fouling rate for flow within a heated tube and its verification. Proceedings of 10th International Heat Transfer Conference. Hemsphere Publishing Corporation, Institution of Chemical Engineers Symposium Series 135: 225–229.

Fahiminia F, Watkinson AP & Epstein N (2007) Early events in the precipitation fouling of calcium sulphate dihydrate under sensible heating conditions. The Canadian Journal of Chemical Engineering 85(5): 679–691.

Fauchoux M, Bansal M, Talukdar P, Simonson CJ & Torvi D (2010) Testing and modelling of a novel ceiling panel for maintaining space relative humidity by moisture transfer. Int J Heat Mass Transfer 53(19): 3961–3968.

Hasson D (1981) Precipitation fouling. In: Somerscales E & Knudsen JG (eds) Fouling of heat transfer equipment. Washington, Hemisphere Publishing Corporation: 527–568.

Hasson D & Karmon M (1983) Novel process for lining water mains by controlled calcite deposition. 5th International Conference on the Internal and External Protection of Pipes: 153–167.

Hasson D, Avriel M, Resnick W, Rozenman T & Windreich S (1968) Mechanism of calcium carbonate scale deposition on heat-transfer surfaces. Industrial & Engineering Chemistry Fundamentals 7(1): 59–65.

Helalizadeh A, Müller-Steinhagen H & Jamialahmadi M (2005) Mathematical modelling of mixed salt precipitation during convective heat transfer and sub-cooled flow boiling. Chemical Engineering Science 60(18): 5078–5088.

Helalizadeh A, Müller-Steinhagen H & Jamialahmadi M (2000) Mixed salt crystallisation fouling. Chemical Engineering and Processing: Process Intensification 39(1): 29–43.

Incropera FP & DeWitt DP (1996) Fundamentals of heat and mass transfer. New York, Wiley & Sons.

Izadi M, Aidun D, Marzocca P & Lee H (2011) Experimental investigation of fouling behavior of 90/10 Cu/Ni tube by heat transfer resistance monitoring method. Journal of Heat Transfer 133(10): 101801.

Kazi SN (2012) Fouling and Fouling Mitigation on Heat Exchanger Surfaces. In: Mitrovic J (ed) Heat Exchangers–Basics Design Applications. Croatia, InTech: 507–532.

Kern D & Seaton R (1959) A theoretical analysis of thermal surface fouling. British Chemical Engineering 4(5): 258–262.

Kraus AD (2003) Heat exchangers. In: Bejan A & Kraus AD (eds) Heat transfer handbook. New Jersey, John Wiley & Sons: 797–911.

Krause S (1993) Fouling of heat-transfer surfaces by crystallization and sedimentation. International Chemical Engineering 33(3): 335–401.

Launder BE & Spalding DB (1972) Lectures in mathematical models of turbulence.

Lee GJ, Tijing LD, Pak BC, Baek BJ & Cho YI (2006) Use of catalytic materials for the mitigation of mineral fouling. Int Commun Heat Mass Transfer 33(1): 14–23.

Mayer M, Augustin W & Scholl S (2013) An approach to modeling induction period in crystallization fouling. Heat and Mass Transfer 49(10): 1419–1432.

Mayer M, Bucko J, Benzinger W, Dittmeyer R, Augustin W & Scholl S (2015) Modeling fouling factors for microscale heat exchangers. Exp Heat Transfer 28(3): 222–243.

Molki M & Sparrow E (1986) An empirical correlation for the average heat transfer coefficient in circular tubes. Journal of Heat Transfer 108(2): 482–484.

Mottahed B & Molki M (1996) Artificial roughness effects on turbulent transfer coefficients in the entrance region of a circular tube. Int J Heat Mass Transfer 39(12): 2515–2523.

Müller-Steinhagen H, Malayeri M & Watkinson A (2002) Heat Exchanger Fouling–Fundamental Approaches and Technical Solutions.

Müller-Steinhagen H, Malayeri M & Watkinson A (2009) Heat exchanger fouling: environmental impacts. Heat Transfer Eng 30(10–11): 773–776.

Müller-Steinhagen H (2011) Heat transfer fouling: 50 years after the Kern and Seaton model. Heat Transfer Eng 32(1): 1–13.

Mullin JW (2001) Crystallization. London, Butterworth-Heinemann.

Mullin J (1961) Crystallization. London, Butterworths.

Mwaba M, Golriz MR & Gu J (2006a) A semi-empirical correlation for crystallization fouling on heat exchange surfaces. Appl Therm Eng 26(4): 440–447.

Mwaba M, Rindt C, Van Steenhoven A & Vorstman M (2006b) Experimental investigation of CaSO4 crystallization on a flat plate. Heat Transfer Eng 27(3): 42–54.

Mwaba M, Rindt C, Van Steenhoven A & Vorstman M (2006c) Validated numerical analysis of $CaSO_4$ fouling. Heat Transfer Eng 27(7): 50–62.

Najibi S, Muller-Steinhagen H & Jamialahmadi M (1997a) Calcium carbonate scale formation during subcooled flow boiling. Journal of Heat Transfer 119(4): 767–775.

Najibi S, Müller-Steinhagen H & Jamialahmadi M (1997b) Calcium sulphate scale formation during subcooled flow boiling. Chemical Engineering Science 52(8): 1265–1284.

Olutimayin SO & Simonson CJ (2005) Measuring and modeling vapor boundary layer growth during transient diffusion heat and moisture transfer in cellulose insulation. Int J Heat Mass Transfer 48(16): 3319–3330.

Pääkkönen TM, Riihimäki M, Puhakka E, Muurinen E, Simonson C & Keiski RL (2009) Crystallization fouling of $CaCO_3$ - Effect of bulk precipitation on mass deposition on the heat transfer surface. Proceedings of International Conference on Heat Exchanger Fouling and Cleaning VIII: 209–216.

Pääkkönen TM, Riihimäki M, Ylönen R, Muurinen E, Simonson C & Keiski RL (2007) Evaluation of heat transfer boundary conditions for CFD modeling of a 3D plate heat exchanger geometry. Proceedings of International Conference on Heat Exchanger Fouling and Cleaning VII. The Berkley Electronic Press, ECI Symposium Series Volume RP 5: 336–343.

Pääkkönen TM, Ojaniemi U, Riihimäki M, Muurinen E, Simonson CJ & Keiski RL (2013) Surface patterning of stainless steel in prevention of fouling in heat transfer equipment. Mater Sci Forum 762: 493–500.

Pääkkönen TM, Riihimäki M, Simonson CJ, Muurinen E & Keiski RL (2012) Crystallization fouling of $CaCO_3$ – Analysis of experimental thermal resistance and its uncertainty. Int J Heat Mass Transfer 55(23–24): 6927–6937.

Pääkkönen TM, Riihimäki M, Simonson CJ, Muurinen E & Keiski RL (2015) Modeling $CaCO_3$ crystallization fouling on a heat exchanger surface – Definition of fouling layer properties and model parameters. Int J Heat Mass Transfer 83(0): 84–98.

Plummer LN & Busenberg E (1982) The solubilities of calcite, aragonite and vaterite in CO_2-H_2O solutions between 0 and 90°C, and an evaluation of the aqueous model for the system $CaCO_3$-CO_2-H_2O. Geochim Cosmochim Acta 46(6): 1011–1040.

Reay D (1999) Learning from experiences with compact heat exchangers. CADDET.

Riihimäki M, Ojaniemi U, Pättikangas T, Pääkkönen TM, Manninen M, Puhakka E, Muurinen E, Simonson C & Keiski RL (2009) Fouling in high solid content suspension – Effect of nucleating air and background electrolyte. Proceedings of International Conference on Heat Exchanger Fouling and Cleaning VIII: 192–199.

Rose IC, Watkinson AP & Epstein N (2000) Testing a mathematical model for initial chemical reaction fouling using a dilute protein solution. The Canadian Journal of Chemical Engineering 78(1): 5–11.

Sawada K (1997) The mechanisms of crystallization and transformation of calcium carbonates. Pure and Applied Chemistry 69(5): 921–928.

Schlichting H (1968) Boundary layer theory. McGraw-Hill.

Scholl S & Augustin W (2006) Numerical simulation of micro roughness effects on convective heat transfer. Computer Aided Chemical Engineering 21: 671–676.

Schreier P & Fryer P (1995) Heat exchanger fouling: a model study of the scaleup of laboratory data. Chemical Engineering Science 50(8): 1311–1321.

Segev R, Hasson D & Semiat R (2012) Rigorous modeling of the kinetics of calcium carbonate deposit formation. AIChE J 58(4): 1222–1229.

Shah R & Sekulic D (1985) Heat exchangers. In: Rohsenow WM, Hartnett JP & Ganic EN (eds) Handbook of heat transfer fundamentals. New York, McGraw-Hill Book Co.

Shaw CT (1992) Using computational fluid dynamics. Hemel Hempstead, Prentice Hall.

Sheikholeslami R (2000) Composite fouling of heat transfer equipment in aqueous media-a review. Heat Transfer Eng 21(3): 34–42.

Sheikholeslami R & Ng M (2001) Calcium sulfate precipitation in the presence of nondominant calcium carbonate: thermodynamics and kinetics. Ind Eng Chem Res 40(16): 3570–3578.

Somerscales E & Knudsen JG (1981) Fouling of heat transfer equipment. Washington, Hemisphere Publishing Corporation.
Stocker T, Qin D, Plattner G, Tignor M, Allen SK, Boschung J, Nauels A, Xia Y, Bex V & Midgley PM (2014) Climate change 2013: The physical science basis. Cambridge, UK, and New York, Cambridge University Press.
Stumm W & Morgan JJ (2012) Aquatic chemistry: chemical equilibria and rates in natural waters. New York, John Wiley & Sons.
Versteeg H & Malalasekera W (1995) An Introduction to Computational Fluid Dynamics - The Finite Volume Method. England, Longman Group Ltd.
Wang L & Sunden B (2003) Optimal design of plate heat exchangers with and without pressure drop specifications. Appl Therm Eng 23(3): 295–311.
Welty JR (1974) Engineering heat transfer. NewYork, John Wiley & Sons.
Zeebe RE (2011) On the molecular diffusion coefficients of dissolved, and and their dependence on isotopic mass. Geochim Cosmochim Acta 75(9): 2483–2498.

Original publications

I Pääkkönen TM, Riihimäki M, Simonson CJ, Muurinen E, and Keiski RL (2012) Crystallization fouling of $CaCO_3$ – Analysis of experimental thermal resistance and its uncertainty. International Journal of Heat and Mass Transfer 55: 6927–6937.

II Pääkkönen TM, Riihimäki M, Simonson CJ, Muurinen E, and Keiski RL (2015) Modeling $CaCO_3$ crystallization fouling on a heat exchanger surface – definition of fouling layer properties and model parameters. International Journal of Heat and Mass Transfer 83: 84–98.

III Pääkkönen TM, Ojaniemi U., Pättikangas T, Manninen M, Muurinen E, Keiski RL and Simonson CJ, (2015) CFD modeling of $CaCO_3$ crystallization fouling on heat transfer surfaces. Manuscript.

IV Pääkkönen TM, Ojaniemi U, Riihimäki M, Muurinen E, Simonson CJ, Keiski RL (2013) Surface patterning of stainless steel in prevention of fouling in heat transfer equipment. Materials Science Forum 762: 493–500.

Original publications are not included in the electronic version of the dissertation.

530. Leppänen, Kimmo (2015) Sample preparation method and synchronized thermography to characterize uniformity of conductive thin films

531. Pouke, Matti (2015) Augmented virtuality : transforming real human activity into virtual environments

532. Leinonen, Mikko (2015) Finite element method and equivalent circuit based design of piezoelectric actuators and energy harvester dynamics

533. Leppäjärvi, Tiina (2015) Pervaporation of alcohol/water mixtures using ultra-thin zeolite membranes : membrane performance and modeling

534. Lin, Jhih-Fong (2015) Multi-dimensional carbonaceous composites for electrode applications

535. Goncalves, Jorge (2015) Situated crowdsourcing : feasibility, performance and behaviours

536. Herrera Castro, Daniel (2015) From images to point clouds : practical considerations for three-dimensional computer vision

537. Komulainen, Jukka (2015) Software-based countermeasures to 2D facial spoofing attacks

538. Pedone, Matteo (2015) Algebraic methods for constructing blur-invariant operators and their applications

539. Karhu, Mirjam (2015) Treatment and characterisation of oily wastewaters

540. Panula-Perälä, Johanna (2015) Development and application of enzymatic substrate feeding strategies for small-scale microbial cultivations : applied for *Escherichia coli*, *Pichia pastoris*, and *Lactobacillus salivarius* cultivations

541. Pennanen, Harri (2015) Coordinated beamforming in cellular and cognitive radio networks

542. Ferreira, Eija (2015) Model selection in time series machine learning applications

543. Lamminpää, Kaisa (2015) Formic acid catalysed xylose dehydration into furfural

544. Visanko, Miikka (2015) Functionalized nanocelluloses and their use in barrier and membrane thin films

545. Gilman, Ekaterina (2015) Exploring the use of rule-based reasoning in ubiquitous computing applications

546. Kemppainen, Antti (2015) Limiting phenomena related to the use of iron ore pellets in a blast furnace

Book orders:
Granum: Virtual book store
http://granum.uta.fi/granum/

UNIVERSITY OF OULU P.O. Box 8000 FI-90014 UNIVERSITY OF OULU FINLAND

ACTA UNIVERSITATIS OULUENSIS

UNIVERSITY of OULU
OULUN YLIOPISTO

ISBN 978-952-62-0934-0 (Paperback)
ISBN 978-952-62-0935-7 (PDF)
ISSN 0355-3213 (Print)
ISSN 1796-2226 (Online)